NUMERICAL AND EXPERIMENTAL TECHNIQUES FOR ENHANCED POWER GENERATION IN A NANOSCALE-GAP THERMOPHOTOVOLTAIC DEVICE

by

Michael P. Bernardi

A dissertation submitted to the faculty of
The University of Utah
in partial fulfillment of the requirements for the degree of

Doctor of Philosophy

Department of Mechanical Engineering

The University of Utah

August 2016

The University of Utah Graduate School

STATEMENT OF DISSERTATION APPROVAL

The dissertation of **Michael P. Bernardi**

has been approved by the following supervisory committee members:

Mathieu Francoeur	, Chair	**3/30/2016** Date Approved
Ian R. Harvey	, Member	**3/30/2016** Date Approved
Keunhan Park	, Member	**3/30/2016** Date Approved
Amanda Smith	, Member	**3/30/2016** Date Approved
Michael A. Scarpulla	, Member	**3/30/2016** Date Approved

and by **Timothy Ameel**, Chair/Dean of

the Department/College/School of **Mechanical Engineering**

and by David B. Kieda, Dean of The Graduate School.

ABSTRACT

Power generation in a nanoscale-gap thermophotovoltaic (nano-TPV) device can be enhanced, compared to conventional thermophotovoltaic (TPV) systems, due to radiative heat transfer exceeding the blackbody limit. TPV power generation refers to direct thermal-to-electrical energy conversion of near infrared and infrared radiation emitted by a terrestrial source. By separating the radiator and the cell by a gap smaller than the peak emitted wavelength, radiative heat transfer can exceed the blackbody predictions by a few orders of magnitude due to energy transport by waves evanescently confined to the surface of the radiator. This enhanced energy transfer can lead to a significant increase in TPV power generation.

This dissertation is divided into two main parts. First, a numerical model is presented which demonstrates increased power generation in nano-TPV devices when compared to conventional TPV systems. The model incorporates near-field radiation, heat and charge transport while accounting for radiative, electrical and thermal losses in the cell. The devices analyzed consist of GaSb cells illuminated by a broadband tungsten and a quasi-monochromatic Drude emitter at 2000 K. Results show an increase in power generation by a factor of 4.7 with a tungsten emitter and a 100-nm-thick gap. Furthermore, it is shown that nano-TPV power generators may perform better with broadband emitters where radiative heat transfer is dominated by frustrated modes rather

than surface modes.

The second part of this dissertation is devoted to the experimental demonstration of radiative heat transfer exceeding the blackbody limit, which is the fundamental phenomenon underlying enhanced power generation in nano-TPV systems. A MEMS-based experimental device has been fabricated for radiative heat flux measurements between 5×5 mm^2 planar intrinsic silicon surfaces separated by a variable gap as small as 150 nm. The separation gap is maintained via rigid spacers and a compliant membrane allows for variation of the gap size via mechanical forces. Results agree well with predictions based on fluctuational electrodynamics. At a gap size of 150 nm, the blackbody limit is exceeded by a factor of 8.4. This is the largest value ever recorded between macroscale planar surfaces at non-cryogenic temperatures.

This dissertation is dedicated to my beautiful and infinitely patient wife, Ginger. Without her support and encouragement, I never would have completed this journey.

Research is what I'm doing when I don't know what I'm doing.

- Wernher von Braun in an interview with the
New York Times, December 16, 1957

TABLE OF CONTENTS

ABSTRACT iii

ACKNOWLEDGEMENTS ix

Chapters

1. INTRODUCTION 1

    1.1 Description of Near-Field Thermal Radiation 1
    1.2 Application of Near-Field Thermal Radiation to Thermophotovoltaic Power Generation 4
    1.3 Objective and Organization of the Dissertation 7
    1.4 References Cited 10

2. LITERATURE SURVEY OF NANOSCALE-GAP THERMOPHOTOVOLTAIC MODELING 14

    2.1 Radiative Losses Only 15
    2.2 Radiative and Electrical Losses 19
    2.3 Radiative, Electrical and Thermal Losses 20
    2.4 References Cited 24

3. IMPACTS OF PROPAGATING, FRUSTRATED AND SURFACE MODES ON RADIATIVE, ELECTRICAL AND THERMAL LOSSES IN NANOSCALE-GAP THERMOPHOTOVOLTAIC POWER GENERATORS 26

    3.1 Results 28
    3.2 Conclusions 35
    3.3 Methods 35
    3.4 References 37
    3.5 Supplemental Information 39

4. LITERATURE SURVEY OF NANOSCALE-GAP THERMOPHOTOVOLTAIC AND NEAR-FIELD RADIATIVE HEAT TRANSFER MEASUREMENTS 45

    4.1 Nano-TPV Measurements 46

4.2 Radiative Heat Transfer Measurements between a Sharp Tip and a Planar Surface 48
4.3 Radiative Heat Transfer Measurements between a Microsphere and a Planar Surface 51
4.4 Radiative Heat Transfer Measurements between Microstructures 55
4.5 Radiative Heat Transfer Measurements between Planar Surfaces 58
4.6 References Cited 63

5. RADIATIVE HEAT TRANSFER EXCEEDING THE BLACKBODY LIMIT BETWEEN MACROSCOPIC PLANAR SURFACES SEPARATED BY A NANOSIZE VACUUM GAP 66

5.1 Radiative Heat Transfer Exceeding the Blackbody Limit between Macroscopic Planar Surfaces Separated by a Nanosize Vacuum Gap 66
5.2 Methods 78
5.3 Supplementary Information 82
5.4 References Cited 93

6. CONCLUSION 96

6.1 Numerical Modeling of a Nano-TPV Power Generator 96
6.2 Experimental Measurements of Near-Field Radiative Heat Transfer 99
6.3 References Cited 103

Appendices

A: USING ELECTROSTATIC FORCES AND CAPACITANCE FOR CONTROLLING AND MEASURING THE GAP SIZE BETWEEN MACROSCALE PLANAR SURFACES SEPARATED BY A NANOSCALE GAP 106

B: EXPERIMENTAL APPARATUS FOR PERFORMING NEAR-FIELD RADIATIVE HEAT TRANSFER MEASUREMENTS 113

ACKNOWLEDGEMENTS

These last few years have been quite a rollercoaster. Although any Ph.D. program will have its ups and downs, I truly enjoyed my time in the Radiative Energy Transfer Lab. Regardless of the countless hours that were devoted to this program, none of it would have been possible without the many people that helped, supported and guided me along the way.

I would first like to thank my advisor, Professor Mathieu Francoeur. He is an incredibly hard worker and excellent teacher. I feel very fortunate to have had him as my advisor. I would also like to thank my past and present lab mates, John DeSutter, Sheila Edalatpour, Spencer Petersen and Mitch Short. I enjoyed every discussion I had with them. I would like to express my appreciation to Professors Ian Harvey, Kay Park, Michael Scarpulla and Amanda Smith who agreed to be a part of my Ph.D. committee. Additionally, this work would not have been possible without the help from Brian Baker and the rest of the staff at the Utah Nanofab.

Of course I also want to thank my family and friends who supported and encouraged me in this endeavor. Lastly, I would like to thank the late George the Pug for making sure I never got too much work done from home.

CHAPTER 1

INTRODUCTION

1.1 Description of Near-Field Thermal Radiation

Radiative heat transfer consists of energy that is transferred by electromagnetic waves. Propagating waves are electromagnetic waves that are emitted from a body that is at a temperature above 0 K. This form of heat transfer is limited by Planck's blackbody distribution. However, the Planck relationship only applies when the objects exchanging radiation are separated by distances larger than the dominant emitted wavelength, λ_{max}. At distances smaller than this wavelength, electromagnetic waves evanescently confined within approximately one wavelength, λ_{max}, from a surface can also contribute to heat transfer. Evanescent waves can be generated by total internal reflection of propagating waves at the emitter-gap interface (frustrated modes). Total internal reflection occurs when the incident angle of a propagating wave inside the emitter is greater than the critical angle defined by Snell's law as $\theta_{cr} = \arcsin(n_2/n_1)$ where n_1 and n_2 are the refractive indices of the emitter and gap, respectively [1]. Evanescent waves can also be generated by mechanical oscillations of free electrons and transverse optical phonons such as surface plasmon-polaritons [2] and surface phonon-polaritons, respectively (surface modes) [3,4].

Figure 1.1 depicts the three types of electromagnetic modes present at an emitter-vacuum interface. For typical thermal radiation temperatures, evanescent modes become dominant when bodies are separated by a few tens to a few hundreds of nanometers. The contribution of these modes can cause net heat flux to exceed blackbody predictions.

Near-field radiative heat transfer cannot be handled via the classical tools based on Planck's blackbody distribution [5,6]. Near-field effects of thermal radiation are accounted for by using fluctuational electrodynamics, where thermal emission is modeled as fluctuating currents in Maxwell's equations [7-9]. Details regarding near-field thermal radiation modeling can be found in textbooks [5,6,10] and various papers [2-4,7,11-18]. Figure 1.2 shows the net radiative flux between a bulk intrinsic silicon (Si) emitter and receiver separated by a vacuum gap of thickness d. Results show a significant enhancement of the flux as the separation gap d decreases. For a 10-nm-thick gap, the net radiative heat flux is over 11 times larger than the blackbody predictions of 3.08×10^{3} Wm^{-2} and over 20 times larger than the predictions based only on propagating modes of 1.69×10^{3} Wm^{-2}.

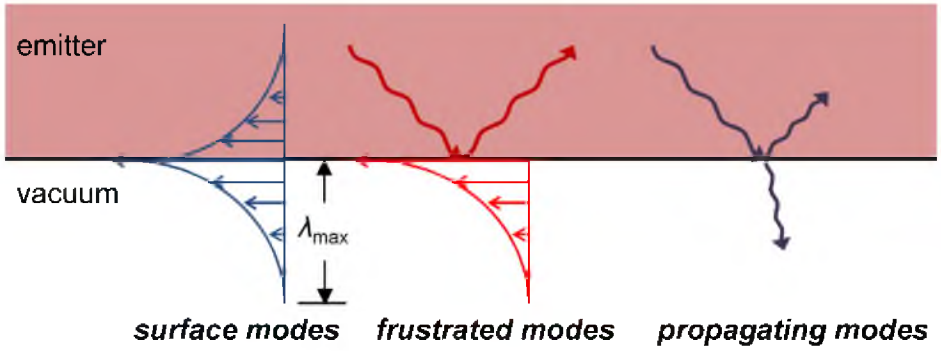

Figure 1.1 Electromagnetic modes generated at an emitter-vacuum interface.

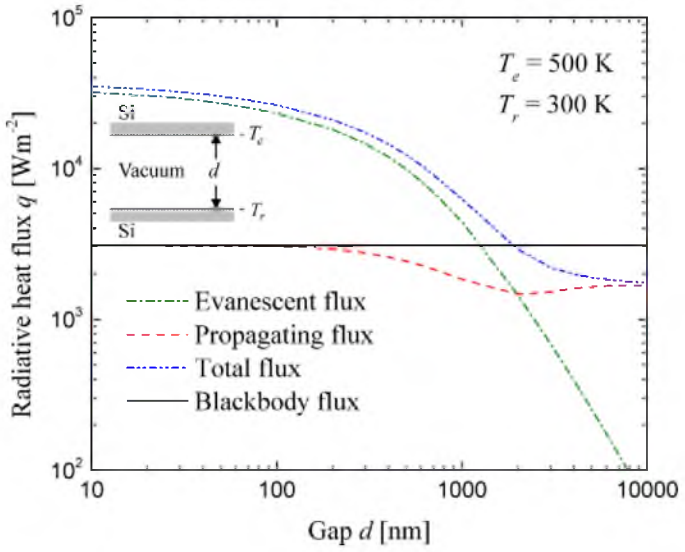

Figure 1.2 Net radiative heat flux q between two Si bulks as a function of vacuum gap d.

Figure 1.3 shows the spectral radiative heat flux exchanged by two bulks of intrinsic Si and two bulks of silicon carbide (SiC) separated by a 150-nm-thick vacuum gap. Intrinsic Si does not support surface modes such that the radiative flux is dominated by frustrated modes. However, since SiC supports surface phonon-polaritons, the flux is dominated by surface modes for that case. The spectral heat flux exchanged by two blackbodies is also shown. In all cases, the temperature of the emitter and receiver is at 500 and 300 K, respectively. As depicted in the Figure 1.3, surface mode mediated radiative heat transfer exhibits a quasi-monochromatic spectral profile while the profile for frustrated modes is broadband. Furthermore, radiative heat transfer exchanged by the bulks of SiC is 3.10×10^4 Wm^{-2}. This is one order of magnitude greater than the case of blackbodies and over 30% greater than the 2.35×10^4 Wm^{-2} that is exchanged by intrinsic Si.

Some of the potential applications of near-field radiative heat transfer include thermal rectification [19], radiative cooling [20], nanostructure characterization [21] and

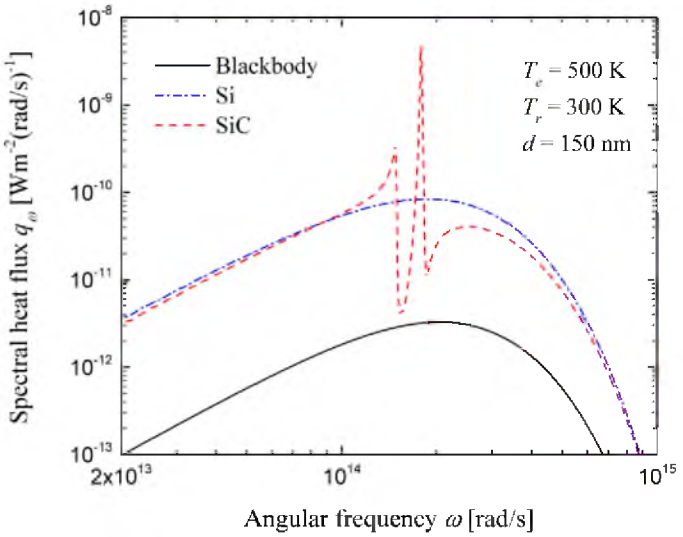

Figure 1.3 Spectral heat flux q_ω as a function of angular frequency ω for bulk intrinsic Si, SiC and blackbodies.

thermophotovoltaic (TPV) power generation [22,23]. The remainder of this dissertation is focused primarily on power generation in TPV cells using near-field thermal radiation.

1.2 Application of Near-Field Thermal Radiation to Thermophotovoltaic Power Generation

Total energy consumption in the United States was over 98 quadrillion Btu in 2014. Less than 10% of that came from renewable resources [24]. By 2040, consumption is expected to reach nearly 106 quadrillion Btu. To aide in satisfying this increasing demand, Baxter et al. [25] discussed how nanotechnology could be used to develop highly efficient renewable energy sources. Solar TPV power generators could benefit from a nanoscale design. In such a solar TPV device, an emitter absorbs solar irradiation and re-emits spectrally selective thermal radiation toward a TPV cell generating electricity. However, TPV devices are not necessarily restricted to solar applications. Any thermal source can be used to heat an emitter. Power generating TPV devices could utilize waste heat (58% of the energy consumed annually in the United States is lost in

the form of heat [26]) in systems such as combustion chambers, photovoltaic (PV) cells and personal computers. TPV power generators are versatile, quiet and pollution-free [27-30]. The power density of a TPV system with a thermal source in the range of 1300 K to 2000 K is approximately 10^4 Wm^{-2} [27,29].

TPV power generation is limited by Planck's blackbody distribution when the gap between the emitter and the TPV cell is larger than the dominant emitted wavelength. In order to improve TPV performance, Whale and Cravalho [22,23] suggested separating the emitter and the cell by a subwavelength vacuum gap. Such a device will be referred to as a nanoscale-gap thermophotovoltaic (nano-TPV) power generator. At sub-wavelength distances, radiative heat transfer is in the near-field regime, such that energy exchange can exceed blackbody predictions by a few orders of magnitude, as discussed in Section 1.1.

The working principle of a nano-TPV power generator can be described as follows. By decreasing the gap separating the emitter and the cell to a subwavelength distance (i.e., below the dominant wavelength emitted as predicted by Wien's law [5]: $\lambda_{max}T$ = 2898 μm·K), radiation transfer exceeds the blackbody predictions due to tunneling of evanescent modes. Higher radiation absorption by the cell thus leads to enhanced photocurrent generation, and potentially higher power output. More specifically, the emitter is maintained at a temperature T_e via an external heat input. Radiation is converted into electricity via a cell that is separated from the emitter by a vacuum gap of thickness d. For the temperatures involved in nano-TPV devices (300 K – 2000 K), d must be of the order of a few tens to a few hundreds of nanometers in order to generate significant power from evanescent modes. A major technological challenge in

nano-TPV power generation is to maintain a nanosize gap between two macrosize surfaces.

Cells with absorption bandgaps of about 1.1 eV are usually employed in solar PV applications. Since TPV emitters operate at lower temperatures (300 K – 2000 K), thermal emission occurs mostly in the near infrared and infrared such that cells with bandgaps lower than 1.1 eV are required (~0.17 eV to 0.85 eV). Typical TPV cells are made of III-V binary compounds, such as GaSb and InAs, as well as ternary and quaternary III-V alloys [27,29,31]. Finally, a thermal management system is needed to keep the cell around 300 K. Figure 1.4 shows a schematic of a nano-TPV power generator.

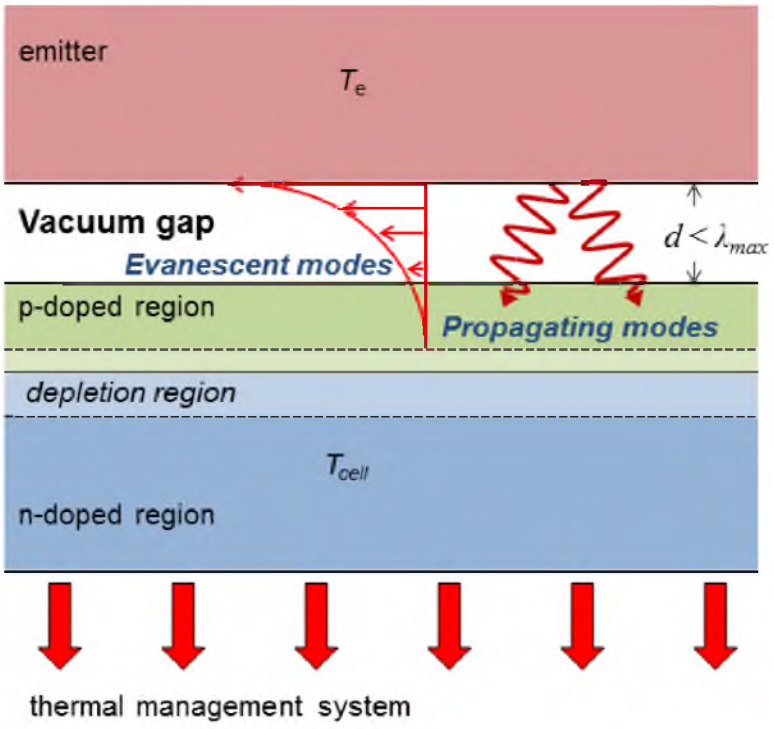

Figure 1.4 Schematic of a nano-TPV power generator.

1.3 Objective and Organization of the Dissertation

A few groups have analyzed nano-TPV devices theoretically [32-42]. These studies predicted a potential power output enhancement by a factor of up to 30. However, most of these models did not account for all the loss mechanisms present in a cell (radiative, electrical and thermal) [32-40]. Francoeur et al. [42] showed that the broadband enhancement of the radiative flux in the near field does not necessarily lead to improved performance due to large thermal losses. It is thus clear that accounting for all three loss mechanisms is a critical component of the design of optimal nano-TPV power generators. Therefore, one of the objectives of this dissertation is to investigate the conversion of evanescent modes into electrical power. In particular, the impact each mode (propagating, frustrated and surface) has on each loss mechanism in a TPV cell is studied for the first time.

Nano-TPV devices constitute an attractive alternative to conventional TPV systems limited by the Planck blackbody distribution. However, experimental nano-TPV devices are challenging to fabricate, since a nanosize gap needs to be maintained between two macroscale surfaces. One of the only experimental studies on nano-TPV power generation was conducted by DiMatteo et al. [43]; however, the results were qualitative.

Although there have been no quantitative experimental studies on nano-TPV power, radiative heat transfer exceeding the blackbody limit at nanosize separation gaps has been demonstrated in various geometric configurations including a sharp tip-surface [44-47], sphere-surface [48-53] and between microstructures [20,54,55]. The validity of fluctuational electrodynamics has been confirmed experimentally down to a separation gap of 2 nm [45]. However, the micro/nanoscale surfaces involved in the aforementioned

experiments limit the amount of radiative energy that can be exchanged, such that these configurations cannot be applied to systems such as nano-TPV power generators. Functional nano-TPV devices require macroscale surfaces separated by a nanosize adjustable vacuum gap. However, experimental research on near-field radiative heat transfer between macroscale surfaces has mainly focused on microsize gaps [56-61]. Observation of significant radiation transfer necessitates larger surfaces and a smaller separation gap. The second objective of this dissertation is to design and fabricate a device capable of maintaining an adjustable nanosize gap between macroscale surfaces. With this device, near-field radiative heat transfer is then measured.

In Chapter 2, the state of the art in nano-TPV modeling is presented. Recent work is discussed in terms of the types of losses present in the models: radiative, electrical and thermal. It is shown that thermal losses have been largely ignored in the literature. In order to guide the design of functional nano-TPV devices, the effect each mode of radiative energy transfer has on each loss mechanism must be well understood.

In order to address the knowledge gap presented in Chapter 2, a numerical model of nano-TPV performance considering the coupled effects of radiative, electrical and thermal losses, in addition to the impact that propagating, frustrated and surface modes have on these losses, is presented in Chapter 3. A numerical analysis of a nano-TPV system incorporating near-field thermal radiation, charge and heat transport is conducted. In particular, nano-TPV systems consisting of a GaSb cell paired with tungsten and fictitious Drude emitters are analyzed. This analysis provides guidelines for the design of nano-TPV devices when all loss mechanisms are taken into account. This work has been published in Scientific Reports [62].

A literature review of TPV and near-field radiative heat transfer measurements is presented in Chapter 4. The research that has been accomplished in the field up until this point is presented. The literature for near-field radiative heat transfer is presented with respect to the geometric configuration: sharp tip and a surface, sphere and a surface, microstructures and planar surfaces.

In Chapter 5, near-field radiative heat transfer measurements between macroscale planar surfaces separated by a nanosize gap are presented. Experimental measurements are made at gaps ranging from 150 to 3500 nm and temperatures differences as high as 120 K. This is accomplished through a microfabricated device and custom built experimental setup. The experimental data is compared against, and found to be in excellent agreement with, a computational model coupling COMSOL and fluctuational electrodynamics. The design, fabrication and calibration of the experimental device and setup is also presented in Chapter 5. The work discussed in this chapter has been submitted for publication to Nature Communications.

A method of controlling the separation gap between the emitter and receiver of the near-field radiative heat transfer device using electrostatic forces and gap size measurement based on capacitance is discussed in Appendix A. Additionally, the balance of electrostatic forces with the restoring spring force of a compliant membrane is analyzed. A discussion of the experimental setup used in this research is presented in Appendix B.

The overall results of this work are discussed in Chapter 6. Also, recommendations for future research in this area are presented.

1.4 References Cited

[1] E. Hecht, *Optics*, 5th ed. (Pearson Education, New York City, 2015).

[2] C.J. Fu and Z.M. Zhang, Int. J. Heat Mass **49**, 1703 (2006).

[3] J.-P. Mulet, K. Joulain, R. Carminati and J.-J. Greffet, Nanosc. Microsc. Therm. **6**, 209 (2002).

[4] K. Joulain, J.-P. Mulet, F. Marquier, R. Carminati and J.-J. Greffet, Surf. Sci. Rep. **57**, 59 (2005).

[5] J.R. Howell, R. Siegel and M.P. Mengüç, *Thermal Radiation Heat Transfer*, 6th ed. (CRC Press, Boca Raton, 2015).

[6] M.F. Modest, *Radiative Heat Transfer*, 3rd ed. (Academic Press, San Diego, 2013).

[7] D. Polder and M. Van Hove, Phys. Rev. B **4**, 3303, 1971.

[8] S.M. Rytov, Y.A. Kravtsov, V.I. Tatarskii, *Principles of Statistical Radiophysics 3: Elements of Random Fields* (Springer, New York, 1989).

[9] L. Novotny and B. Hecht, *Principles of Nano-Optics* (Cambridge University Press, New York, 2006).

[10] Z.M. Zhang, *Micro/Nanoscale Heat Transfer* (McGraw-Hill, New York, 2007).

[11] J.J. Loomis and H.J. Maris, Phys. Rev. B **50**, 18517 (1994).

[12] J.B. Pendry, J. Phys.-Condens. Mat. **11**, 6621 (1999).

[13] A. Narayanaswamy and G. Chen, Annu. Rev. Heat Transfer **14**, 169 (2005).

[14] A. Narayanaswamy and G. Chen, Phys. Rev. B **77**, 075125 (2008).

[15] M. Francoeur, M.P. Mengüç and R. Vaillon, J. Quant. Spectrosc. Radiat. Transfer **110**, 2002 (2009).

[16] S. Basu, Z.M. Zhang and C.J. Fu, Int. J. Ener. Res. **33**, 1202 (2009).

[17] M. Francoeur, M.P. Mengüç and R. Vaillon, J. Phys. D: Appl. Phys. **43**, 075501 (2010).

[18] S. Edalatpour and M. Francoeur, J. Quant. Spectrosc. Radiat. Transfer **133**, 364 (2014).

[19] C.R. Otey, W.T. Lau and S. Fan, Phys. Rev. Lett. **104**, 154301 (2010).

[20] B. Guha, C. Otey, C.B. Poitras, S. Fan and M. Lipson, Nano Lett. **12**, 4546 (2012).

[21] M.R. Short, J.-M. Geffrin, R. Vaillon, H. Tortel, B. Lacroix and M. Francoeur, J. Quant. Spectrosc. Radiat. Transfer **146**, 452 (2014).

[22] M.D. Whale, PhD Thesis, MIT, 1997.

[23] M.D. Whale and E.G. Cravalho, IEEE T. Energy Conver. **17**, 130 (2002).

[24] U.S. Energy Information Administration: http://www.eia.gov/, March 1, 2016.

[25] J. Baxter, Z. Bian, G. Chen, D. Danielson, M.S. Dresselhaus, A.G. Federov, T.S. Fisher, C.W. Jones, E. Maginn, U. Kortshagen, A. Manthiram, A. Nozik, D.R. Rolison, T. Sands, L. Shi, D. Sholl and Y. Wu, Energ. Environ. Sci. **2**, 559 (2009).

[26] T.L. Bergman, A.S. Lavine, F.P. Incropera and D.P. DeWitt, *Fundamentals of Heat and Mass Transfer*, 7th ed. (Wiley, Hoboken, 2011).

[27] T. Bauer, *Thermophotovoltaics: Basic Principles and Critical Aspects of System Design* (Springer, New York, 2011).

[28] T.J. Coutts, Sol. Energ. Mat. Sol. Cells **66**, 443 (2001).

[29] M.G. Mauk, in *Mid-Infrared Semiconductor Optoelectronics* (Springer, New York, 2006).

[30] D.L. Chubb, *Fundamentals of Thermophotovoltaic Energy Conversion* (Elsevier, The Netherlands, 2007).

[31] J.A. Gonzalez-Cuevas, T.F. Refaat, M.N. Abedin and H.E. Elsayed-Ali, J. Appl. Phys. **102**, 014504 (2007).

[32] A. Narayanaswamy and G. Chen, Appl. Phys. Lett. **82**, 3544 (2003).

[33] M. Laroche, R. Carminati and J.-J. Greffet, J. Appl. Phys. **100**, 063704 (2006).

[34] O. Ilic, M. Jablan, J.D. Joannopoulos, I. Celanovic and M. Soljačić, Opt. Express **20**, A366 (2012).

[35] C. Simovski, M. Stanislav, I. Nefedov and S. Tretyakov, Opt. Express **21**, 14988 (2013).

[36] R. Messina and P. Ben-Abdallah, Sci. Rep. **3**, 1383 (2013).

[37] V.B. Svetovoy and G. Palasantzas, Phys. Rev. Appl. **2**, 034006 (2014).

[38] K. Park, S. Basu, W.P. King and Z.M. Zhang, J. Quant. Spectrosc. Radiat. Transfer **109**, 305 (2008).

[39] T.J. Bright, L.P. Wang and Z.M. Zhang, J. Heat Transfer **136**, 062701 (2014).

[40] L. Lim, S. Jin, S.S. Lee and B.J. Lee, Opt. Express **23**, A240 (2015).

[41] E. Elzouka and S. Ndao, Sol. Energ., doi: 10.1016/j.solener.2015.02.007, in press (2015).

[42] M. Francoeur, R. Vaillon and M.P. Mengüç, IEEE T. Energy Conver. **26**, 686 (2011).

[43] R.S. DiMatteo, P. Greiff, S.L. Finberg, K.A. Young-Waithe, H.K.H. Choy, M.M. Masaki and C.G. Fonstad, Appl. Phys. Lett. **79**, 1894 (2001).

[44] A. Kittel, W. Müller-Hirsch, J. Parisi, S.-A. Biehs, D. Reddig and M. Holthaus, Phys. Rev. Lett. **95**, 224301 (2005).

[45] K. Kim, B. Song, V. Fernández-Hurtado, W. Lee, W. Jeong, L. Cui, D. Thomson, J. Feist, M.T.H. Reid, F.J. García-Vidal, J.C. Cuevas, E. Meyhofer and P. Reddy, Nature **528**, 387 (2015).

[46] J.-B. Xu, K. Läuger, R. Möller, K. Dransfield and I.H. Wilson, J. Appl. Phys. **76**, 7209 (1994).

[47] L. Worbes, D. Hellmann and A. Kittel, Phys. Rev. Lett. **110**, 134302 (2013).

[48] A. Narayanaswamy, S. Shen and G. Chen, Phys. Rev. B **78**, 115303 (2008).

[49] S. Shen, A. Narayanaswamy and G. Chen, Nano Lett. **9**, 2909 (2009).

[50] E. Rousseau, A. Siria, G. Jourdan, S. Volz, F. Comin, J. Chevrier and J.-J. Greffet, Nature Photon. **3**, 514 (2009).

[51] S. Shen, A. Mavrokefalos, P. Sambegoro and G. Chen, Appl. Phys. Lett. **100**, 233114 (2012).

[52] B. Song, Y. Ganjeh, S. Sadat, D. Thomson, A. Fiorino, V. Fernández-Hurtado, J. Feist, F.J. García-Vidal, J.C. Cuevas, P. Reddy and E. Meyhofer, Nat. Nanotechnol. **10**, 253 (2015).

[53] J. Shi, B. Liu, P. Li, L.Y. Ng and S. Shen, Nano Lett. **15**, 1217 (2015).

[54] C. Feng, Z. Tang, J. Yu and C. Sun, Sensors **13**, 1998 (2013).

[55] R. St-Gelais, B. Guha, L. Zhu, S. Fan and M. Lipson, Nano Lett. **14**, 6971 (2014).

[56] G.A. Domoto, R.F. Boehm and C.L. Tien, J. Heat Transfer **92**, 412 (1970).

[57] T. Kralik, P. Hanzelka, M. Zobac, V. Musilova, T. Fort and M. Horak, Phys. Rev. Lett. **109**, 224302 (2012).

[58] C.M. Hargreaves, Phys. Lett. **30A**, 491 (1969).

[59] L. Hu, A. Narayanaswamy, X.Y. Chen and G. Chen, Appl. Phys. Lett. **92**, 133106 (2008).

[60] R.S. Ottens, V. Quetschke, S. Wise, A.A. Alemi, R. Lundock, G. Mueller, D.H. Reitze, D.B. Tanner and B.F. Whiting, Phys. Rev. Lett. **107**, 014301 (2011).

[61] T. Ijiro and N. Yamada, Appl. Phys. Lett. **106**, 023103 (2015).

[62] M.P. Bernardi, O. Dupré, E. Blandre, P.-O. Chapuis, R. Vaillon and M. Francoeur, Sci. Rep. **5**, 11626 (2015).

CHAPTER 2

LITERATURE SURVEY OF NANOSCALE-GAP THERMOPHOTOVOLTAIC MODELING

Radiative heat transfer between bodies separated by subwavelength gaps exceeds Planck's blackbody distribution due to energy transport by evanescent modes [1-12]. As discussed in Chapter 1, these modes include evanescent waves generated by total internal reflection of propagating waves at the emitter-gap interface (frustrated modes) and resonant surface waves (surface modes) such as surface plasmon-polaritons [13] and surface phonon-polaritons [14]. The impact of evanescent waves on thermophotovoltaic (TPV) systems is reviewed in this chapter.

There are three main loss mechanisms in TPV devices that degrade their performance: radiative, electrical and thermal. Radiation with energy smaller than the cell bandgap does not contribute to the generation of electron-hole pairs (EHPs) and is considered a radiative loss. EHPs that recombine prior to reaching the depletion region, and therefore do not contribute to photocurrent generation, are considered electrical losses. This includes EHP recombination in the bulk and at the surfaces of the cell. Thermal losses are associated with the increasing temperature of the TPV cell. As cell temperature increases, the dark current in the cell also increases. Dark current opposes the photogenerated current and causes power output to decrease. The mechanisms that lead to radiative and electrical losses also tend to lead to thermal losses. Radiation that is

absorbed by the cell with energy smaller than the cell bandgap does not generate an EHP and only contributes to cell heating. In addition, radiation with energy greater than the cell bandgap dissipates its excess energy as heat through thermalization, which causes the cell temperature to increase. Nanoscale-gap TPV (nano-TPV) modeling efforts are reviewed in this chapter with respect to the types of losses that are considered.

2.1 Radiative Losses Only

Narayanaswamy and Chen [15] considered an emitter made of cubic boron nitride (cBN) at 1000 K, supporting surface phonon-polaritons in the infrared, in order to achieve quasi-monochromatic energy transfer. A fictitious cell maintained at 300 K with an absorption bandgap of 0.13 eV, matching the surface phonon-polariton resonance of the radiator, was used. As this model does not account for electrical or thermal losses, this work reports the results in terms of the fraction of energy absorbed by the cell that could potentially contribute to photocurrent generation, referred to as overexcitation efficiency, $F_{o'}$. Results of the model are shown in Figure 2.1. It was found that for a 20-nm- thick vacuum gap, the cell absorbs 1.17×10^{6} Wm^{-2} above the bandgap while only 5.67×10^{4} Wm^{-2} is absorbed when a blackbody emitter in the far field is considered. Due to the negative effects of recombination and heat generation within the cell, the actual power output would be less than 1.17×10^{6} Wm^{-2}.

Laroche et al. [16] analyzed a nano-TPV device consisting of a gallium antimonide (GaSb) cell maintained at 300 K and a quasi-monochromatic emitter approximated by a Drude model with resonance matching the cell bandgap of 0.72 eV at 2000 K. Power generated, P_{el}, as a function of gap size, d, is shown in Figure 2.2. At a gap size of 10 μm, electrical power generated is 1.4×10^{3} Wm^{-2}. Generated power

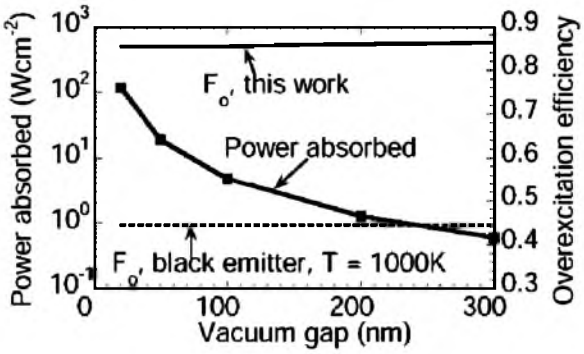

Figure 2.1 Power absorbed and overexcitation efficiency, $F_{O'}$, as a function of vacuum gap from Narayanaswamy and Chen [15].

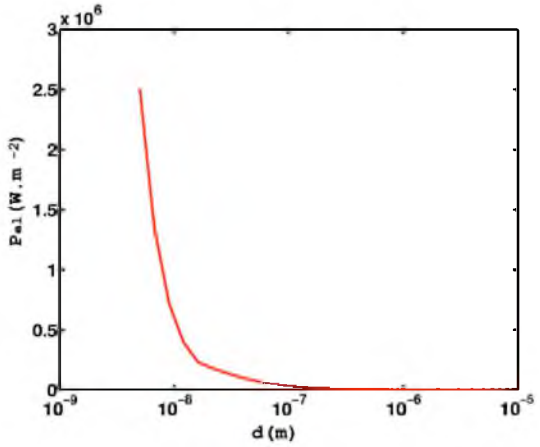

Figure 2.2 Power density, P_{el}, as a function of gap size, d, for a GaSb cell illuminated by a quasi-monochromatic emitter from Laroche et al. [16].

increases by over 3 orders of magnitude to 2.5×10^6 Wm^{-2} at a gap size of 5 nm. A photocurrent enhancement of an order of magnitude over that of a blackbody radiator in the far field was also reported. Although mention is made of cell heating due to thermalization and absorption by the lattice and free carriers, thermal losses are not taken into account since the cell is maintained at 300 K. It is also assumed that all EHPs generated within the cell contribute to photocurrent generation, and therefore the model neglects to take into account electrical losses from any EHPs that recombine before reaching the depletion region.

Messina and Ben-Abdallah [17] modeled a TPV cell on which a single layer of graphene is deposited. By changing the chemical potential, μ, of the graphene, its electrical and optical properties can be tuned in order to more effectively absorb thermal radiation from the emitter. The cell consists of an indium antimonide (InSb) p-n junction maintained at 300 K. A vacuum gap as small as 10 nm separated the cell from a hexagonal boron nitride (hBN) emitter. Figure 2.3 shows cell performance as a function of gap size and heat source temperature. The authors reported an increase in conversion efficiency, η, from 10% without graphene to 20% with graphene. Also, the power output of the device with graphene, $P_{PV,g}$, increased by a factor of 8 over the power output of the device without graphene, P_{PV}. However, as the cell is maintained at a constant temperature and recombination is not considered, electrical and thermal losses were consequently neglected.

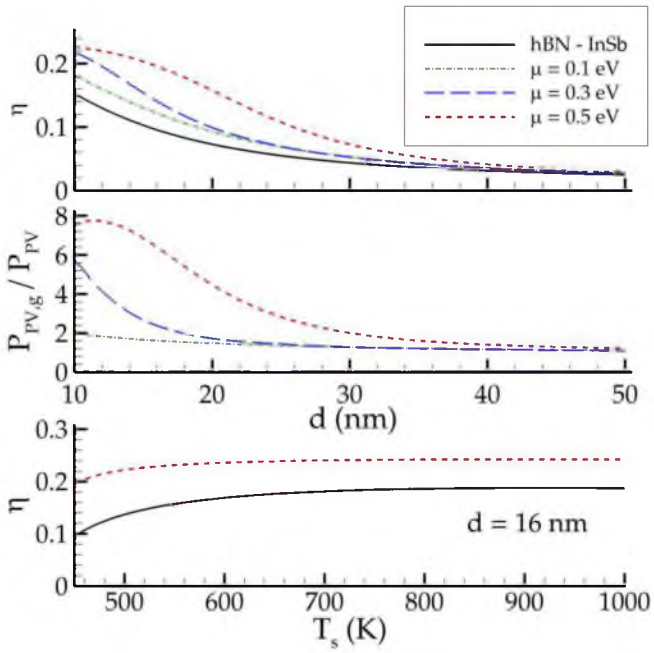

Figure 2.3 Conversion efficiency, η, and power enhancement, $P_{PV,g}/P_{PV}$, as a function of gap size, d, as well as conversion efficiency, η, as a function of emitter temperature, T_s, with respect to graphene chemical potential, μ, from Messina and Ben-Abdallah [17].

Svetovoy and Palasantzas [18] used a graphene-on-Si (GOS) Schottky cell to maximize thermal radiation absorption in the near field. Absorption is increased due to the excitation of plasmons in the graphene layer. Power generated when using a hBN emitter was found to be one order of magnitude greater than when an InSb cell was used. Results are shown in Figure 2.4. These predictions overestimate actual nano-TPV performance since electrical and thermal losses were not taken into account.

Ilic et al. [19], Simovski et al. [20], and Guo et al. [21] did not model the power generated by a TPV device, but instead attempted to optimize the radiative energy transfer between the emitter and the TPV cell. Ilic et al. [19] minimized radiative losses in the cell by considering various emitters supporting surface modes in the near infrared (fictitious Drude model, indium tin oxide, silver, graphene). Furthermore, Ilic et al. [19] modified the parameters of an emitter represented by a Drude model in order to maximize radiative energy transfer above the cell bandgap. Similarly, Simovski et al. [20] modeled a vacuum gap filled with nanowires that behaved as hyperbolic metamaterials in order to

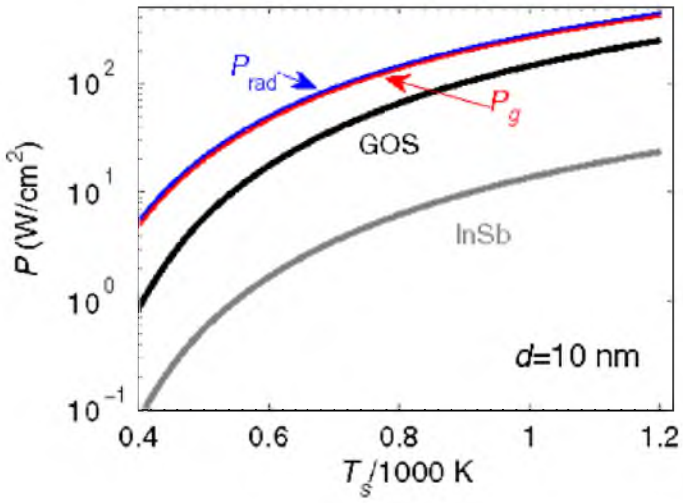

Figure 2.4 Total radiative flux emitted, P_{rad}, and radiative flux absorbed by graphene, P_g, as a function of emitter temperature from Svetovoy and Palantzas [18]. Also, the output power of the GOS and InSb cells as a function of radiator temperature, T_s.

optimize radiative energy transfer. Guo et al. [21] discussed tuning the emission of plasmonic metamaterials to obtain quasi-monochromatic radiative energy transfer for nano-TPV applications. These models may oversimplify the optimization of the emitter since only radiative losses are considered. Optimization of a nano-TPV device is not possible without considering all three loss mechanisms.

2.2 Radiative and Electrical Losses

Radiative and electrical losses in nano-TPV power generators were considered for the first time by Park et al. [22]. A device consisting of a tungsten emitter at 2000 K and an indium gallium antimonide ($In_{0.18}Ga_{0.82}Sb$) TPV cell maintained at 300 K was investigated. This model factors in electrical losses by accounting for recombination in the bulk and at the surfaces of the cell. An electrical power output of 10^6 Wm^{-2} at a gap distance of 10 nm was reported. This is an enhancement over the power output for the far-field case of over a factor 30. As shown in Figure 2.5, results also revealed that electrical losses induce a drop in conversion efficiency, and thus in power output, of 5 to 10%.

Bright et al. [23] modeled a nano-TPV system consisting of an $In_{0.18}Ga_{0.82}Sb$ cell maintained at 300 K illuminated by a tungsten emitter at temperatures ranging from 1250 K to 2000 K. The model incorporated a gold backside reflector to recycle radiation that does not contribute to photocurrent generation by reflecting waves with energy lower than the absorption bandgap of the cell back to the emitter. This approach effectively increases nano-TPV conversion efficiency by decreasing the radiation absorbed by the cell without actually increasing the power output. A relative increase in conversion efficiency of 35% for a device with a radiator maintained at 1250 K was reported. The

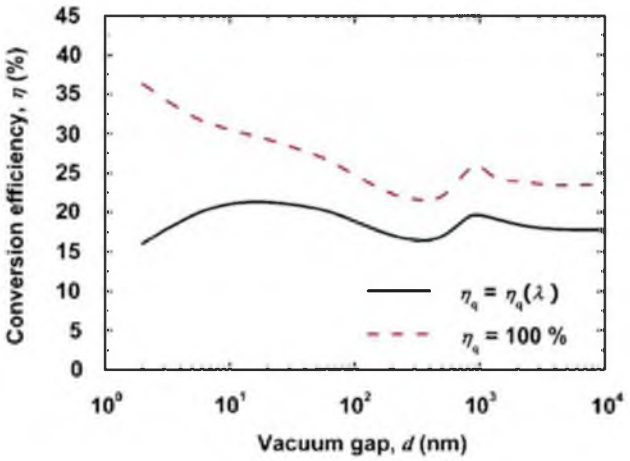

Figure 2.5 Conversion efficiency, η, as a function of vacuum gap, d, with respect to whether electrical losses are included in the model from Park et al. [22].

authors also highlighted that high surface recombination velocities negatively affect conversion efficiency at nanosize gaps due to the low penetration depth of evanescent modes within the cell.

Lim et al. [24] analyzed a nano-TPV system consisting of a doped silicon (Si) emitter at 500 K and an InSb cell maintained at 300 K. A cell with a monolayer of graphene with chemical potentials of 0.5 and 1.0 eV was also modeled. Figure 2.6 depicts the results from this study. When graphene with a chemical potential of 1.0 eV was used, results showed that power output and conversion efficiency increased by factors of 30 and 6.1, respectively, when compared to the case without graphene.

2.3 Radiative, Electrical and Thermal Losses

Francoeur et al. [25] were the first to consider the coupled effects of radiative, electrical and thermal losses on the performance of a nano-TPV system made of a tungsten emitter maintained at 2000 K and an $In_{0.18}Ga_{0.82}Sb$ cell. Figure 2.7 shows power generated, P_m, and radiative energy absorbed by the cell, q_{cell}^{abs}, as a function of cell

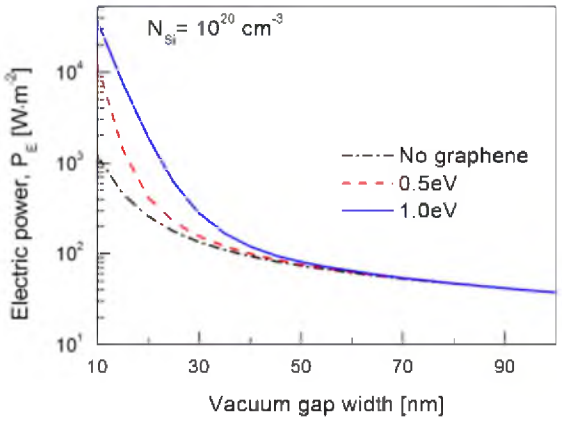

Figure 2.6 Power generated, P_E, as a function of vacuum gap, d, with respect to graphene chemical potential from Lim et al. [24].

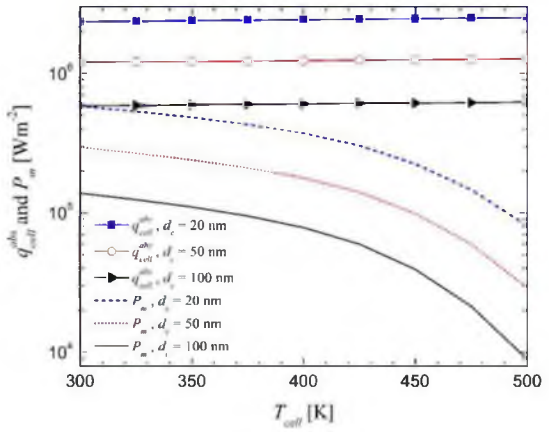

Figure 2.7 Absorbed radiative flux, q_{cell}^{abs}, and power generated, P_m, as a function of cell temperature, T_{cell}, with respect to vacuum gap size, d_c, from Francoeur et al. [25].

temperature, T_{cell}. Absorbed radiative energy remains fairly independent of cell temperature while power output decreases as the cell temperature rises. Results revealed that the broadband enhancement of the radiative flux in the near field does not automatically lead to improved performance due to large thermal losses in the cell inducing a significant drop of the power output. It was found that a thermal management system with a high heat transfer coefficient of 10^5 $Wm^{-2}K^{-1}$ was required to maintain the cell near room temperature for nanosize gaps in order to obtain performance similar to

that of Park et al. [22].

Elzouka and Ndao [26] considered nano-TPV devices for solar applications. They reported power output 30 times greater than far-field devices for a nano-TPV system comprised a tungsten emitter and an $In_{0.18}Ga_{0.82}Sb$ cell separated by a 20-nm-thick gap. Although thermal effects were not coupled with radiative and electrical losses, their model is able to calculate the heat generated in the cell. Power generated, P_m, and heat rejected, Q_{rej}, by the cell are shown in Figure 2.8 for emitter temperatures, T_e, of 1500, 2000 and 2500 K. In order to maintain the cell at 300 K, less than 10^4 Wm^{-2} needs to be rejected for a gap separation distance of 5 μm and an emitter temperature of 1500 K. The heat rejected increases by over four orders of magnitude to nearly 10^8 Wm^{-2} when the gap separation distance is 1 nm and the emitter temperature is 2500 K. This shows that heat generation in the cell poses a significant problem that needs to be addressed when designing nano-TPV power generators.

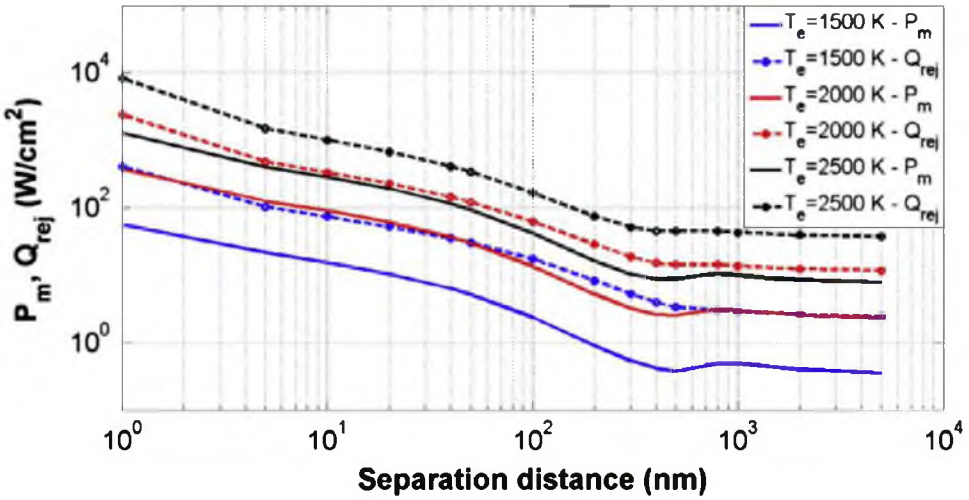

Figure 2.8 Output power, P_m, and heat rejected, Q_{rej}, as a function of gap separation distance from Elzouka and Ndao [26].

It is clear that it is necessary to account for the coupled effects of radiative, electrical and thermal losses in order to obtain realistic nano-TPV predictions. Accounting for the three loss mechanisms is a critical component of the design of optimal nano-TPV power generators. Indeed, Dupré and Vaillon [27] proposed a novel approach for optimizing the performance of standard crystalline Si solar cells by minimizing radiative and electrical losses as well as thermal losses. It was shown that the cell architecture leading to a maximum power output is significantly affected when thermal losses are considered in the optimization procedure.

The literature cited shows that power generation can be enhanced when the gap between the emitter and the cell is a few tens of nanometers [22,25]. However, most of the works cited do not account for the thermal impacts on nano-TPV performance. Since the temperature of the cell increases substantially as the gap size between it and the emitter decreases, it is also important to consider cooling technologies in order to increase system performance as well as lifespan. Cooling technologies discussed by Jakhar et al. [28] for concentrated PV systems may also be applicable to nano-TPV power generators.

Chapter 3 of this dissertation addresses the requirement of considering the coupled effects of radiative, electrical and thermal losses on the performance of a nano-TPV device. The effect that each radiative heat transfer mode (propagating, frustrated and surface) has on each loss mechanism is studied in detail. This type of analysis has never before been examined in the literature.

2.4 References Cited

[1] Z.M. Zhang, *Micro/Nanoscale Heat Transfer* (McGraw-Hill, New York, 2007).

[2] J.R. Howell, R. Siegel and M.P. Mengüç, *Thermal Radiation Heat Transfer*, 6th ed. (CRC Press, Boca Raton, 2015).

[3] K. Joulain, J.-P. Mulet, F. Marquier, R. Carminati and J.-J. Greffet, Surf. Sci. Rep. **57**, 59 (2005).

[4] A. Kittel, W. Müller-Hirsch, J. Parisi, S.-A. Biehs, D. Reddig and M. Holthaus, Phys. Rev. Lett. **95**, 224301 (2005).

[5] L. Hu, A. Narayanaswamy, X.Y. Chen and G. Chen, Appl. Phys. Lett. **92**, 133106 (2008).

[6] S. Shen, A. Narayanaswamy and G. Chen, Nano Lett. **9**, 2909 (2009).

[7] E. Rousseau, A. Siria, G. Jourdan, S. Volz, F. Comin, J. Chevrier and J.-J. Greffet, Nature Photon. **3**, 514 (2009).

[8] R.S. Ottens, V. Quetschke, S. Wise, A.A. Alemi, R. Lundock, G. Mueller, D.H. Reitze, D.B. Tanner and B.F. Whiting, Phys. Rev. Lett. **107**, 014301 (2011).

[9] S. Shen, A. Mavrokefalos, P. Sambegoro and G. Chen, Appl. Phys. Lett. **100**, 233114 (2012).

[10] K. Kim, B. Song, V. Fernández-Hurtado, W. Lee, W. Jeong, L. Cui, D. Thomson, J. Feist, M.T.H. Reid, F.J. García-Vidal, J.C. Cuevas, E. Meyhofer and P. Reddy, Nature **528**, 387 (2015).

[11] B. Song, Y. Ganjeh, S. Sadat, D. Thomson, A. Fiorino, V. Fernández-Hurtado, J. Feist, F.J. García-Vidal, J.C. Cuevas, P. Reddy and E. Meyhofer, Nat. Nanotechnol. **10**, 253 (2015).

[12] M. Lim, S.S. Lee and B.J. Lee, Phys. Rev. B **91**, 195136 (2015).

[13] C.J. Fu and Z.M. Zhang, Int. J. Heat Mass **49**, 1703 (2006).

[14] J.-P. Mulet, K. Joulain, R. Carminati and J.-J. Greffet, Nanosc. Microsc. Therm. **6**, 209 (2002).

[15] A. Narayanaswamy and G. Chen, Appl. Phys. Lett. **82**, 3544 (2003).

[16] M. Laroche, R. Carminati and J.-J. Greffet, J. Appl. Phys. **100**, 063704 (2006).

[17] R. Messina and P. Ben-Abdallah, Sci. Rep. **3**, 1383 (2013).

[18] V.B. Svetovoy and G. Palasantzas, Phys. Rev. Appl. **2**, 034006 (2014).

[19] O. Ilic, M. Jablan, J.D. Joannopoulos, I. Celanovic and M. Soljačić, Opt. Express **20**, A366 (2012).

[20] C. Simovski, M. Stanislav, I. Nefedov and S. Tretyakov, Opt. Express **21**, 14988 (2013).

[21] Y. Guo, S. Molesky, H. Hu, C.L. Cortes and Z. Jacob, Appl. Phys. Lett. **105**, 073903 (2014).

[22] K. Park, S. Basu, W.P. King and Z.M. Zhang, J. Quant. Spectrosc. Radiat. Transfer **109**, 305 (2008).

[23] T.J. Bright, L.P. Wang and Z.M. Zhang, J. Heat Transfer **136**, 062701 (2014).

[24] L. Lim, S. Jin, S.S. Lee and B.J. Lee, Opt. Express **23**, A240 (2015).

[25] M. Francoeur, R. Vaillon and M.P. Mengüç, IEEE T. Energy Conver. **26**, 686 (2011).

[26] E. Elzouka and S. Ndao, Sol. Energ., doi: 10.1016/j.solener.2015.02.007, in press (2015).

[27] O. Dupré and R. Vaillon, IRESR **6,** 011201 (2014).

[28] S. Jakhar, M.S. Soni and N. Gakkhar, Renew. Sust. Energ. Rev. **60**, 41 (2016).

CHAPTER 3

IMPACTS OF PROPAGATING, FRUSTRATED AND SURFACE MODES ON RADIATIVE, ELECTRICAL AND THERMAL LOSSES IN NANOSCALE-GAP THERMOPHOTOVOLTAIC POWER GENERATORS

Reprinted with permission from Bernardi M.P., Dupré O., Blandre E., Chapuis P.-O., Vaillon R. and Francoeur M., Impacts of propagating, frustrated and surface modes on radiative, electrical and thermal losses in nanoscale-gap thermophotovoltaic power generators, *Scientific Reports* **5**, 11626, 2015.

www.nature.com/scientificreports

SCIENTIFIC REPORTS

OPEN

Impacts of propagating, frustrated and surface modes on radiative, electrical and thermal losses in nanoscale-gap thermophotovoltaic power generators

Received: 04 March 2015
Accepted: 01 June 2015
Published: 26 June 2015

Michael P. Bernardi[1], Olivier Dupré[2], Etienne Blandre[2], Pierre-Olivier Chapuis[2], Rodolphe Vaillon[2] & Mathieu Francoeur[1]

The impacts of radiative, electrical and thermal losses on the performances of nanoscale-gap thermophotovoltaic (nano-TPV) power generators consisting of a gallium antimonide cell paired with a broadband tungsten and a radiatively-optimized Drude radiator are analyzed. Results reveal that surface mode mediated nano-TPV power generation with the Drude radiator outperforms the tungsten radiator, dominated by frustrated modes, only for a vacuum gap thickness of 10 nm and if both electrical and thermal losses are neglected. The key limiting factors for the Drude- and tungsten-based devices are respectively the recombination of electron-hole pairs at the cell surface and thermalization of radiation with energy larger than the cell absorption bandgap. A design guideline is also proposed where a high energy cutoff above which radiation has a net negative effect on nano-TPV power output due to thermal losses is determined. It is shown that the power output of a tungsten-based device increases by 6.5% while the cell temperature decreases by 30 K when applying a high energy cutoff at 1.45 eV. This work demonstrates that design and optimization of nano-TPV devices must account for radiative, electrical and thermal losses.

Radiation heat transfer in the near field, where bodies are separated by sub-wavelength gaps, exceeds Planck's blackbody distribution due to energy transport by tunneling of evanescent modes[1–10]. These modes include evanescent waves generated by total internal reflection of propagating waves at the material-gap interface (frustrated modes) and surface waves such as surface plasmon-polaritons[11] and surface phonon-polaritons (surface modes)[12]. Whale and Cravalho[13,14] suggested that direct thermal-to-electrical energy conversion via thermophotovoltaic (TPV) power generators could benefit from the near-field effects of thermal radiation by spacing the radiator and the cell by a sub-wavelength vacuum gap. Since then, a few groups analyzed nanoscale-gap TPV (nano-TPV) power generators theoretically[15–25] and experimentally[26–31].

Numerical studies predicted a potential power output enhancement by a factor of 20 to 30 in nano-TPV systems, but most of these modeling efforts only accounted for radiative losses in the cell[15–20]. Radiative and electrical losses in nano-TPV power generators were considered for the first time by Park *et al.*[21] A device consisting of a tungsten radiator at 2000 K and an indium gallium antimonide ($In_{0.18}Ga_{0.82}Sb$) cell maintained at 300 K was modeled. Results revealed that electrical losses induce a drop

[1]Radiative Energy Transfer Lab, Department of Mechanical Engineering, University of Utah, Salt Lake City, UT 84112, USA. [2]Université de Lyon, CNRS, INSA-Lyon, UCBL, CETHIL, UMR5008, F-69621 Villeurbanne, France. Correspondence and requests for materials should be addressed to M.P.B. (email: michael.bernardi@utah.edu) or R.V. (email: rodolphe.vaillon@insa-lyon.fr) or M.F. (email: mfrancoeur@mech.utah.edu)

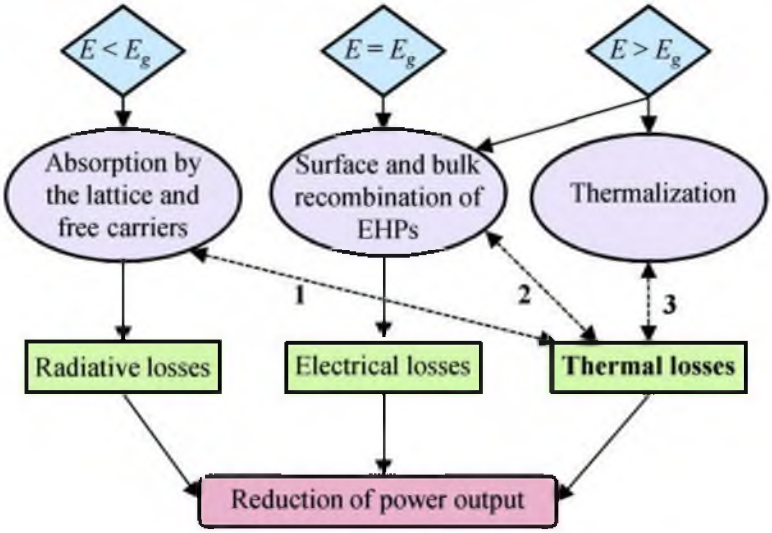

Figure 1. Coupled effects of radiative, electrical and thermal losses on the power output of nano-TPV power generators.

in conversion efficiency by 5 to 10%. To date, only Francoeur *et al.*[25] considered the coupled effects of radiative, electrical and thermal losses on the performances of a nano-TPV system made of a tungsten radiator maintained at 2000 K and an $In_{0.18}Ga_{0.82}Sb$ cell. Results showed that the broadband enhancement of the radiative flux in the near field does not automatically lead to improved performance due to large thermal losses and the associated temperature increase in the cell inducing a significant drop of the power output. It was found that a thermal management system with a high heat transfer coefficient of $10^5\,Wm^{-2}K^{-1}$ was required to maintain the cell at room temperature for nanometer-size gaps in order to obtain performances similar to those of Park *et al.* It is thus clear that accounting for the three loss mechanisms is a critical component of the design of optimal nano-TPV power generators. Indeed, Dupré and Vaillon[32] proposed a novel approach for optimizing the performance of standard crystalline silicon solar cells by minimizing radiative and electrical losses as well as thermal losses that are usually omitted. It was shown that the cell architecture leading to a maximum power output is affected when thermal losses are considered in the optimization procedure. This is expected to have an even more significant impact in the optimization of nano-TPV power generators.

Nano-TPV power generators constitute an attractive alternative to conventional TPV systems limited by the Planck blackbody distribution. Experimental nano-TPV devices are however challenging to fabricate, since a nanosize vacuum gap needs to be maintained between two surfaces having dimensions of a few hundreds of micrometers to a few millimeters. As such, this technology will be viable only if a significant power output enhancement over conventional TPV devices can be obtained. The objective of this paper is therefore to investigate in depth the impacts of radiative, electrical and thermal losses on nano-TPV power output enhancement. In particular, the contributions of propagating, frustrated and surface modes to radiative, electrical and thermal losses are analyzed for nano-TPV systems with tungsten and radiatively-optimized Drude radiators. A secondary objective is to provide general guidelines for the design and conception of nano-TPV devices when all loss mechanisms are taken into account.

Results

Interplay between radiative, electrical and thermal losses. Figure 1 shows how the coupled effects of radiative, electrical and thermal losses negatively affect nano-TPV power output. Note that losses are defined relative to the power absorbed by the cell. Reflection by the cell is not a radiative loss for nano-TPV systems, as reflected radiation can be absorbed by the radiator. Yet, reflection should be minimized in order to maximize radiation absorption by the cell. Additionally, transmission is negligible for a micrometer-thick cell. Radiation absorbed by the cell with energy E below its bandgap E_g does not generate electron-hole pairs (EHPs) and is classified as a radiative loss. Since this energy is dissipated as heat via absorption by the lattice and the free carriers, it also contributes to thermal

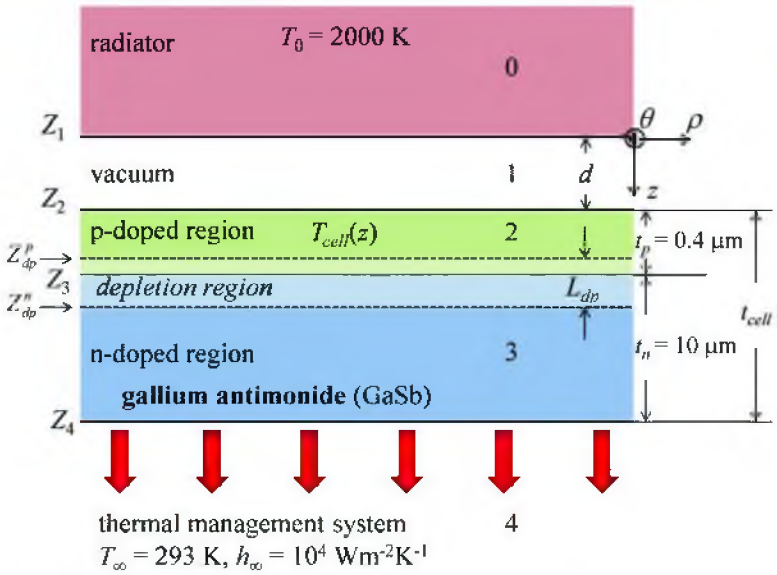

Figure 2. Nano-TPV power generator consisting of a radiator, maintained at a constant and uniform temperature of 2000 K, separated by a vacuum gap of thickness *d* from a GaSb cell.

losses resulting in an increase of the cell temperature T_{cell}. As T_{cell} increases, the dark current increases thereby decreasing the power output[25]. The radiative properties and the absorption bandgap of the cell are temperature-dependent, such that there is a feedback component, shown by the dashed arrow 1 in Fig. 1, affecting the absorption characteristics and therefore the radiative losses. Radiation absorbed by the cell with energy E equal to or larger than E_g generates EHPs. Electrical losses arise when the photogenerated EHPs recombine before being separated at the depletion region of the cell, thus reducing the power output. Electrical losses include recombination within the volume and at the surfaces of the cell. These mechanisms also contribute to thermal losses since the EHPs that undergo non-radiative recombination dissipate their energy as heat. As the electrical properties of the cell are temperature-dependent, an increase in T_{cell} also affects recombination of EHPs; this coupling is represented by the dashed arrow 2 in Fig. 1. Radiation with energy E larger than the bandgap E_g dissipates its excess energy as heat through thermalization, thus contributing to thermal losses. There is a feedback component to this loss mechanism, shown by the dashed arrow 3 in Fig. 1, as increasing T_{cell} lowers the absorption bandgap of the cell and modifies its radiative properties. Clearly, accounting for thermal losses substantially increases the complexity of the problem as the loss mechanisms are strongly coupled to each other.

Description of the problem. The nano-TPV power generator under study is shown in Fig. 2 and consists of a semi-infinite radiator (layer 0) at a temperature of 2000 K and a 10.4-µm-thick cell (layers 2 and 3) separated by a vacuum gap of thickness d (layer 1). The problem is assumed to be one-dimensional, for which only the variations along the z-axis normal to the surface of the radiator and the cell are accounted. The cell is modeled as a single p-n junction made of gallium antimonide (GaSb) that has a bandgap of 0.723 eV at 293 K. The thickness and doping level of the p-region (layer 2) are 0.4 µm and 10^{19} cm^{-3}, respectively, while the thickness of the n-region (layer 3) is 10 µm with a doping level of 10^{17} cm^{-3}. For these conditions, the thickness of the depletion region, assumed to be exclusively in the n-doped region, is 113 nm at 293 K[25]. A convective boundary condition with $T_\infty = 293$ K and a heat transfer coefficient fixed at $h_\infty = 10^4$ Wm^{-2}K^{-1} is used as a thermal management system (layer 4).

Vacuum gap thicknesses d ranging from 10 to 1000 nm are considered in order to maximize radiative heat transfer by evanescent modes. In practice, maintaining a vacuum gap on the order of a few tens of nanometers between two millimeter-size surfaces is difficult to achieve. However, in the future, the bottlenecks associated with maintaining a nanosize gap may be overcome. As such, the analysis presented here is not limited to current technological constraints. Additionally, measurement of radiation heat transfer between a microsize sphere and a surface separated by a 30-nm-thick vacuum gap was reported by Rousseau *et al.*[5]. The experimental results were compared against numerical predictions based on the

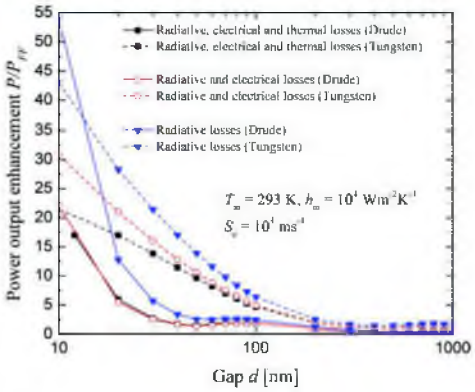

Figure 3. Power output enhancement as a function of the vacuum gap thickness d and the type of losses considered for tungsten and Drude radiators.

Derjaguin approximation, where the flux between the sphere and the surface is computed as a summation of local heat fluxes between two parallel surfaces. The results presented hereafter could thus be used for designing a sphere-surface nano-TPV experimental bench where it is possible to maintain a nanosize gap.

Various numerical studies that accounted solely for radiative losses suggested that radiators with quasi-monochromatic emission in the near field matching the bandgap of the cell result in better performing nano-TPV power generators. In order to verify this hypothesis, a radiatively-optimized radiator supporting surface polariton modes made of a fictitious material with a dielectric function described by a Drude model given by $\varepsilon(\omega) = 1 - \omega_p^2/(\omega^2 + i\Gamma\omega)$ is considered, where the plasma frequency ω_p and the loss coefficient Γ are fixed at 1.83×10^{15} rad/s (1.20 eV) and 2.10×10^{13} rad/s (0.0138 eV), respectively. These values were chosen following the technique proposed by Ilic *et al.*[17] where Γ is calculated to maximize radiation transfer with energy larger than the cell absorption bandgap for a vacuum gap of 10 nm. Optimizing Γ for every gap thickness is unnecessary as it leads to a variation in the power output of less than 1%. The plasma frequency ω_p was chosen so that surface polariton resonance occurs at a radiation energy slightly above the cell bandgap. Surface polariton resonance for the radiator-vacuum interface is $\omega_p/\sqrt{2}$, which corresponds to a frequency of 1.29×10^{15} rad/s (0.850 eV)[1]. For the specific values of ω_p and Γ selected here, the real part of the refractive index of the Drude radiator is between zero and one within the spectral band of interest (0.09 eV $\leq E \leq$ 2.5 eV), such that no frustrated modes are generated at the radiator-vacuum interface. For comparison, a tungsten radiator where the emission in the near field is dominated by frustrated modes is also considered. The dielectric function of tungsten has been obtained by curve-fitting the data provided in Ref. 33. Note that despite supporting surface plasmon-polaritons in the near infrared, tungsten does not exhibit quasi-monochromatic near-field thermal emission due to high losses. For the tungsten-vacuum interface, resonance occurs when the real part of the permittivity $\varepsilon' = -1$ which corresponds to a frequency of 1.97×10^{15} rad/s (1.30 eV). At this frequency, the imaginary part of the permittivity ε'' is large and takes a value of 20.3.

In the simulations, the cell is discretized into N control volumes and its temperature is initialized at 293 K. The radiative energy absorbed in each control volume is calculated from fluctuational electrodynamics[34], and is used to determine the net radiation absorbed by the cell due to the lattice and the free carriers, the heat losses by thermalization and the local generation rate of EHPs. The generated photocurrent and heat sources due to non-radiative and radiative recombination are afterwards calculated by solving the minority carrier diffusion equations. Note that radiative recombination has a negligible effect on the overall energy balance of the cell[35]. An updated temperature of the cell is obtained by solving the energy equation. The radiative, electrical and thermophysical properties of the GaSb cell, provided in Ref. 25, are calculated at the updated cell temperature, and computations are repeated until T_{cell} converges. The dark current is obtained by solving the minority carrier diffusion equations without the local generation rate of EHPs, and various performance indicators, such as the power output and conversion efficiency, are finally calculated. The details of the computational model are provided in the Methods section.

Impacts of radiative, electrical and thermal losses on nano-TPV power output enhancement. Figure 3 shows the power output enhancement of the tungsten- and radiatively-optimized

Drude-based nano-TPV power generators as a function of the vacuum gap thickness d and the type of losses considered in the model. The corresponding conversion efficiency, η_c, is provided in Fig. S1 of the Supplemental Information section. For both radiators, the power output enhancement is defined as the power output of the actual device (P) over the power output obtained with a tungsten source in the far field when all loss mechanisms are considered ($P_{FF} = 3.18 \times 10^4\,\mathrm{Wm^{-2}}$, $T_{cell} = 298\,\mathrm{K}$). Note that when thermal losses are neglected, the temperature of the cell is fixed at 293 K.

The power output enhancement increases as the thickness of the vacuum gap decreases due to an increasing contribution of evanescent modes to the radiative flux. The only exception arises for the Drude radiator, where the power output enhancement increases non-monotonically for sub-100 nm vacuum gap thicknesses; the local minimum observed at $d = 50\,\mathrm{nm}$ will be explained when analyzing the separate contributions of propagating, frustrated and surface modes. For a fixed gap thickness and for the tungsten radiator, the power output enhancement P/P_{FF} is maximum when only radiative losses are considered, where it is assumed that all radiation absorbed by the cell with energy E larger than the bandgap E_g generates EHPs contributing to the photocurrent (i.e., the quantum efficiency is 100% for radiation with $E \geq E_g$). When radiative and electrical losses are taken into account, the quantum efficiency for radiation with $E \geq E_g$ is no longer 100% due to bulk and surface recombination of EHPs thus resulting in a lower power output enhancement. For the case that radiative, electrical and thermal losses are considered, heat generation in the cell due to absorption by the lattice and the free carriers, thermalization and recombination of EHPs increases the temperature of the cell, thus decreasing the power output enhancement because of an increase of the dark current. The same conclusions are applicable for the Drude radiator, except in the gap range from 20 to 80 nm where the power output enhancement for radiative, electrical and thermal losses slightly exceeds the predictions for radiative and electrical losses. This counterintuitive behavior is explained by the fact that the cell bandgap decreases as T_{cell} increases, thus increasing radiation absorption and EHP generation. For the case of radiative, electrical and thermal losses, T_{cell} varies from 350 to 303 K in the gap range from 20 to 80 nm, corresponding to bandgap variations from 0.701 to 0.719 eV; for the case of radiative and electrical losses, T_{cell} is 293 K such that the bandgap is fixed at 0.723 eV. However, above a certain temperature, thermal effects become dominant and cause the power output to deteriorate rapidly due to a large dark current. Note that the equilibrium temperatures of both types of nano-TPV devices as a function of the vacuum gap thickness are provided in Fig. S.2 of the Supplemental Information section. In all simulations, the temperature difference in the cell is negligible ($\Delta T_{cell} \leq 1.3\,\mathrm{K}$), such that a single average temperature is reported for a given vacuum gap thickness.

The maximum power output enhancement, arising for a 10-nm-thick gap, is 43.0 and 53.9 for the tungsten- and the Drude-based devices, respectively, when only radiative losses are considered; the corresponding conversion efficiencies are 47.9% and 59.5%. When both electrical and thermal losses are added, the cell temperature, the conversion efficiency and the power output enhancement for the tungsten radiator are respectively 448 K, 21.2% and 21.5 (−50.0% drop in power output enhancement relative to radiative losses), while the cell exceeds its melting temperature of 985 K for the Drude-based system. It is also interesting to note that the radiatively-optimized Drude radiator leads to a power output enhancement larger than that achieved with tungsten only for the case $d = 10\,\mathrm{nm}$ when only radiative losses are accounted for.

Figure 4 shows the power output enhancement as a function of the vacuum gap thickness, the type of losses considered and the modes contributing to power generation. These modes are defined relative to the radiator-vacuum interface. Propagating modes propagate in both the radiator and the vacuum gap, and correspond to waves with parallel wavevectors k_ρ smaller than k_0, where k_0 is the magnitude of the wavevector in vacuum. Frustrated modes are propagating within the radiator and evanescent in the vacuum gap, such that they are described by parallel wavevectors $k_0 < k_\rho < n' k_0$, where n' is the real part of the refractive index of the radiator. Finally, surface polariton modes are evanescent on both sides of the radiator-vacuum interface and are described by parallel wavevectors $k_\rho > n' k_0$.

For the tungsten radiator shown in Fig. 4(a), the power output enhancement in the near field is dominated by frustrated modes. For example, at $d = 10\,\mathrm{nm}$, the relative contributions of propagating, frustrated and surface modes to P/P_{FF} are respectively 7.4, 75.9 and 16.7% when all loss mechanisms are considered. Note that that the power output enhancement due to propagating waves exceeds unity even when radiative, electrical and thermal losses are included in the model. In the far field, the cell absorbs a propagating flux of $1.05 \times 10^5\,\mathrm{Wm^{-2}}$ and this number increases to $2.24 \times 10^5\,\mathrm{Wm^{-2}}$ when the gap thickness is 10 nm. The increased absorption of propagating waves in the near field is due to two phenomena. First, as $d \to 0$, the transmission factor between the radiator and the cell (i.e., transmission factor between interfaces Z_1 and Z_2 in Fig. 2) for propagating waves approaches unity[35]. Secondly, constructive and destructive wave interference within the gap causes the propagating radiative flux to oscillate, thus leading to local maximum and minimum[36]. As shown in Fig. S.3 of the Supplemental Information section, the propagating flux absorbed by the cell converges to the far-field value at a gap thickness of approximately 2 μm where interference of propagating waves become negligible (the peak emitted wavelength for a radiator temperature of 2000 K is 1.45 μm according to Wien's law).

For the Drude radiator shown in Fig. 4(b), the power output enhancement is dominated by surface modes (no frustrated modes are generated). Again, the oscillations shown for the propagating modes are due to an increasing transmission factor as d decreases and wave interference; the maximum at $d = 700\,\mathrm{nm}$

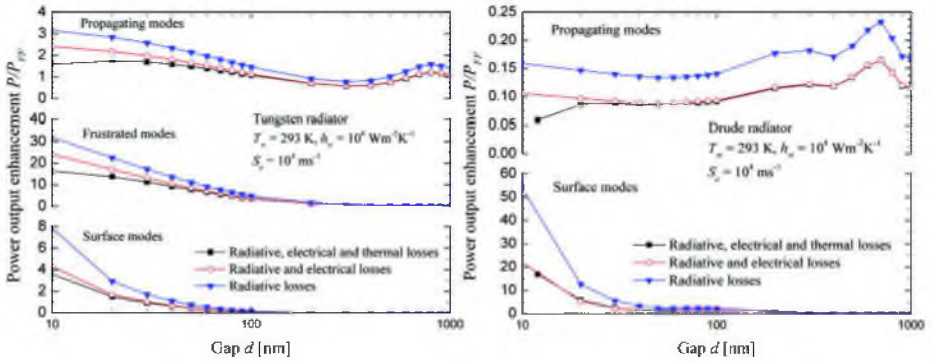

Figure 4. Power output enhancement as a function of the vacuum gap thickness d and the type of losses considered showing the contributions of propagating, frustrated and surface modes: (**a**) tungsten radiator. (**b**) Drude radiator.

is attributed to constructive wave interference (see Fig. S.3). The relative contribution of surface modes to power generation is more than 99% for gap thicknesses equal to or smaller than 20 nm regardless of the types of losses considered. Figure 4(b) also shows that the local minimum observed for a 50-nm-thick gap is due to surface modes. This minimum arises due to a modification of the dispersion relation of surface modes supported at the radiator-vacuum interface caused by the presence of the cell. At gap thicknesses equal to or smaller than 30 nm, surface polariton resonance at an angular frequency of $\omega_p/\sqrt{2}$ (0.85 eV) dominates energy transfer. At gap thicknesses equal to or larger than 80 nm, radiative energy transfer is dominated by a second peak at a lower radiation energy (~0.75 eV). As outlined by Laroche *et al.*[16], this peak corresponds to the non-asymptotic portion of the dispersion relation of surface modes that is broadened by the cell. As the broadening of the dispersion relation varies as a function of the vacuum gap thickness, the spectral location and strength of the second peak varies with gap thickness. The local minimum at $d = 50$ nm is due to the transition between the two peaks, as shown in Fig. S.4 of the Supplemental Information section.

The Drude radiator used here has been optimized by minimizing radiative losses. It is clear however that even if only radiative losses are considered, nano-TPV power generation dominated by surface modes is useful in the extreme near field for a vacuum gap thickness on the order of 10 nm. Indeed, the radiative flux absorbed by the cell with the tungsten radiator decreases at a slower rate than with the Drude radiator (see Fig. S.5 of the Supplemental Information section). For vacuum gap thicknesses from 10 to 50 nm, the total radiative heat flux absorbed with the Drude radiator decays at a rate proportional to $d^{-1.82}$ when only radiative losses are considered. Note that the fact that radiative energy is being transferred between dissimilar materials results in a slight deviation from the d^{-2} power law observed for surface polariton mediated energy transfer between identical materials[37].

Figure 4 suggests that the contribution of surface modes to the power output is more affected by electrical losses than the contribution by frustrated modes. Surface polaritons are modes with large momentum (i.e., large parallel wavevector $k_{//}$) and thus small penetration depth on the order of the vacuum gap separating the radiator and the cell[37,38]. On the other hand, the penetration depth of frustrated modes is on the order of the wavelength in the medium and is independent of the vacuum gap thickness. Consequently, for nanosize gaps, recombination of EHPs at, or near, the surface of the cell is likely to be a limiting factor to surface polariton mediated nano-TPV power generation. The diffusion length of the minority carrier electrons in the p-region of the cell can be estimated as $L_e = \sqrt{D_e \tau_e}$. For GaSb at 293 K, the electron diffusion coefficient D_e and lifetime τ_e are 29.1 cm^{2}s^{-1} and 5.70 ns[39], respectively, thus resulting in a diffusion length L_e of 4.07 μm. Therefore, bulk recombination of EHPs is not the limiting factor to surface polariton mediated nano-TPV power generation since L_e is much larger than the thickness of the p-doped region. A surface recombination velocity S_e of 10^4 ms^{-1} at the top surface of the cell was used for generating the results shown in Figs 3 and 4, which is a typical value for GaSb[39]. In order to further investigate the effect of surface recombination on nano-TPV performance, simulations have been performed using a surface recombination velocity of $S_e = 0$ ms^{-1} (see Fig. S.6 of the Supplemental Information section). Although completely eliminating surface recombination is unrealistic, it is possible to minimize S_e by decreasing the surface roughness and/or passivating the surface, at least in silicon-based photovoltaics[40–42]. For a 10-nm-thick gap, the tungsten-based system exhibits a power output enhancement of 41.6, a 3.3% relative decrease when compared to the case where only radiative losses are

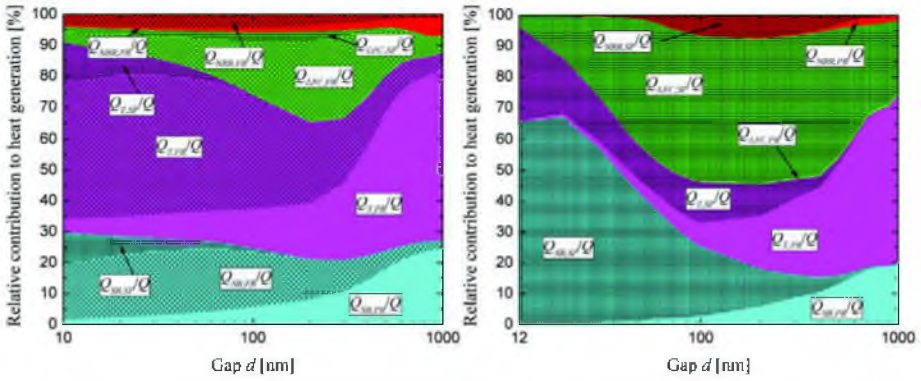

Figure 5. Relative contributions of thermalization (*T*), bulk non-radiative recombination (*NRR*), surface recombination (*SR*) and absorption by the lattice and the free carriers (*LFC*) due to propagating (*PR*), frustrated (*FR*) and surface (*SP*) modes to heat generation within the cell as a function of the vacuum gap thickness *d*: (a) Tungsten radiator (note that negligible contributions to the total heat generation are not shown). **(b)** Drude radiator.

considered and a relative increase of 88.2% over the case that includes electrical losses with surface recombination. For the same gap thickness, the Drude-based system has a power output enhancement of 53.6. This is a 0.5% relative decrease from the case with radiative losses and a 143% relative increase over the case that includes electrical losses with surface recombination. These results show that surface recombination is a limiting factor to nano-TPV power generation due to the small penetration depth associated with evanescent modes. Surface recombination has a larger effect on the performance of the Drude-based system than the tungsten-based device due to the fact that surface polariton modes are characterized by larger parallel wavevectors than frustrated modes and thus smaller penetration depths in the cell. Surface polariton mediated nano-TPV power generation is thus potentially interesting at very small gap thicknesses and when surface recombination velocity is minimized, although those conditions may be difficult to achieve in practice.

Despite a large heat transfer coefficient of $10^4\,Wm^{-2}K^{-1}$ for the thermal management system, thermal losses have a significant negative impact on nano-TPV power generation. For the Drude radiator, Figs. 3 and 4(b) show that thermal losses have a negligible effect on P/P_{FF}, when compared to the case of radiative and electrical losses, down to a gap thickness of 20 nm. The cell reaches a temperature of 350 K for $d = 20$ nm, as opposed to 388 K when the tungsten radiator is used (see Fig. S.2). However, the cell temperature rapidly increases with the Drude radiator for gap thicknesses below 20 nm and eventually exceeds its melting point slightly below a 12-nm-thick gap. To better understand the mechanisms responsible for thermal losses, the relative contributions of thermalization, bulk non-radiative recombination of EHPs, surface recombination of EHPs, and absorption by the lattice and the free carriers due to propagating, frustrated and surface modes to heat generation Q are plotted in Fig. 5 as a function of the gap thickness d. The units for heat generation due to surface recombination (Q_{SR}) are Wm^{-2}, while the remaining contributions within the cell have units of Wm^{-3}. For comparison purposes, thermalization (Q_T), bulk non-radiative recombination (Q_{NRR}) and absorption by the lattice and the free carriers (Q_{LFC}) are integrated over the thickness of the cell in order to obtain units of Wm^{-2}. Note that the magnitude of the total heat generation ranges from $5.43 \times 10^4\,Wm^{-2}$ at $d = 1000$ nm to $1.54 \times 10^6\,Wm^{-2}$ at $d = 10$ nm for the tungsten-based system; for the Drude-based system, the total heat generation varies from $1.41 \times 10^4\,Wm^{-2}$ at $d = 1000$ nm to $1.99 \times 10^6\,Wm^{-2}$ at $d = 12$ nm.

For the tungsten radiator (Fig. 5(a)), thermal losses are dominated by thermalization of frustrated modes for sub-300 nm gap thicknesses and by thermalization of propagating modes for larger gaps. This is explained by the fact that thermal emission by a tungsten radiator is broadband such that the near field enhancement occurs at all frequencies. A large portion of the radiation absorbed by the cell thus contributes simultaneously to EHP generation and thermalization. After some limiting photon energy $E\ (>E_g)$, it is reasonable to expect that radiation absorption has a net negative effect on the cell arising when the reduction of the power output due to heat generation overcomes the power produced by EHP photogeneration. This will be analyzed further in the next sub-section.

For the Drude radiator (Fig. 5(b)), thermal losses at small gap distances are dominated by surface recombination of EHPs generated by surface modes. It is therefore imperative to minimize the surface

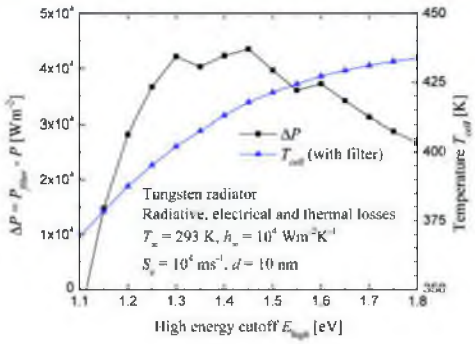

Figure 6. Difference of power output with and without filtering ΔP and cell temperature T_{cell} as a function of the high energy cutoff E_{high} (the low energy cutoff is fixed at 0.66 eV).

recombination velocity when radiation transfer is dominated by surface modes in order to minimize both electrical and thermal losses. However, one must keep in mind that even if surface recombination is minimized, surface polariton mediated nano-TPV power generation outperforms traditional radiators only in the extreme near field. Thermalization is not as critical for the Drude radiator when compared to tungsten, since radiative heat transfer in the near field is quasi-monochromatic. The relative contribution of thermalization increases as d increases, when the flux contains a non-negligible portion of broadband propagating waves.

From the results obtained here, it is obvious that a Drude radiator optimized by accounting solely for radiative losses is not a viable solution for enhancing power generation in nano-TPV devices. The design of nano-TPV systems maximizing power generation must account for all three loss mechanisms, radiative, electrical and thermal.

Estimation of cutoff spectral band for improved nano-TPV performance. The results discussed in the previous section suggest that nano-TPV systems exploiting frustrated modes outperform devices capitalizing on surface modes, except in the extreme near field when both electrical and thermal losses are minimized. However, broadband radiators supporting frustrated modes lead to high thermal losses due to thermalization. This section attempts to improve the performance of a tungsten-based device ($d = 10$ nm) dominated by frustrated modes by filtering a portion of the near-field emission spectrum while accounting for all loss mechanisms

Radiation with energy E lower than the absorption bandgap of the cell E_g should be suppressed as it only contributes to radiative and thermal losses (see Fig. 1). For simplicity, a fixed low energy cutoff of 0.66 eV is selected since the cell temperature is expected to be higher than 293 K due to thermal losses. This choice is motivated by the fact that when all losses are considered, the device with the tungsten radiator and $d = 10$ nm reaches an equilibrium temperature of 448 K; at this temperature, the resulting absorption bandgap of the cell is 0.66 eV. In addition, the reduction of the power output associated with heat dissipation in the cell due to absorption of radiation with energy E larger than E_g, dominated by thermalization, may exceed the power produced from the generation of EHPs. As such, a high energy cutoff E_{high} above which radiation absorption has a net negative effect on the power output can be determined. This is done by analyzing the difference between the power output obtained with and without filtering ($\Delta P = P_{filter} - P$, where $P = 6.82 \times 10^5$ W/m^2) as a function of E_{high} (see Fig. 6). Although employing a conventional filter to achieve the desired spectrum in the near field is unlikely, man-made structures such as metamaterials and photonic crystals can be used for controlling thermal emission.

There is an optimum high energy cutoff E_{high} (1.45 eV) at which the difference in power output ΔP is maximized. This arises since the cell temperature decreases with decreasing the high energy cutoff due to smaller heat losses by thermalization. As such, the maximum voltage increases while the maximum current decreases since a smaller number of EHPs are generated by decreasing the high energy cutoff (see Fig. S.7 of the Supplemental Information section). By limiting thermal emission by the tungsten source to a spectral band from 0.66 to 1.45 eV, a power output enhancement of 22.9 is achieved. This is a 6.5% increase compared to the power output enhancement when considering the full spectrum of tungsten, where a P/P_{1g} value of 21.5 was obtained. The conversion efficiency also increases from 21.1% when considering the full spectrum to 25.6% when capitalizing on the filtered spectrum (see Fig. S.8 of the Supplemental Information section). It is also remarkable that the cell reaches a temperature of 418 K, while a temperature of 448 K was obtained with the entire spectrum. By analyzing thermal losses that are

usually neglected in the literature, it is possible to decrease the cell temperature by 30 K (and thus reduce the cooling load) and to increase the power output enhancement by 6.5%.

It is clear that thermal losses are an integral part of the design of optimal nano-TPV power generators. Here, it was possible to determine a spectral limit above which radiation absorption is more detrimental than beneficial to the power output by accounting for heat generation within the cell. A rigorous optimization scheme would require further analysis for determining the near-field thermal spectrum maximizing power generation.

Conclusions

This work demonstrated that a quasi-monochromatic radiator supporting surface modes outperforms a tungsten radiator only in the extreme near field when both electrical and thermal losses are minimized. In an actual nano-TPV power generator and for a realistic vacuum gap thickness of 100 nm, which would automatically account for all loss mechanisms, a power output enhancement of 4.69 is achieved through the use of a tungsten radiator, while a power output enhancement of 1.89 is obtained with a radiatively-optimized Drude radiator. Recombination of EHPs at the surface of the cell is the main limiting factor to surface mode mediated nano-TPV power generation. For a radiator dominated by frustrated modes, thermalization significantly affects nano-TPV power output due to the broadband enhancement of the flux in the near field. Finally, it was shown that the impact of thermalization in a device dominated by frustrated modes can be mitigated by determining a high energy cutoff above which radiation absorption has a net negative effect on nano-TPV power output. For tungsten, a high energy cutoff of 1.45 eV leads to an increase of the power output by 6.5% and a decrease of the cell temperature by 30 K. Such an analysis is only possible when thermal losses are considered, thus showing that radiative, electrical and thermal losses must be considered in the design of optimal nano-TPV power generators.

Methods

The net radiative heat flux absorbed by a control volume of thickness Δz_j in the cell is calculated using fluctuational electrodynamics and dyadic Green's functions for layered media[25,34]. The absorbed radiation with energy equal to or larger than the bandgap of the cell is used for calculating the local monochromatic generation rate of EHPs $g_{j,\omega}$ [$m^{-3}s^{-1}(rad/s)^{-1}$], acting as a source term in the minority carrier diffusion equations:[25,45]

$$D_e \frac{d^2 \Delta n_{e,\omega}(z)}{dz^2} - \frac{\Delta n_{e,\omega}(z)}{\tau_e} + g_{\omega}(z) = 0 \tag{1}$$

$$D_h \frac{d^2 \Delta n_{h,\omega}(z)}{dz^2} - \frac{\Delta n_{h,\omega}(z)}{\tau_h} + g_{\omega}(z) = 0 \tag{2}$$

where the dependent variables $\Delta n_{e,\omega}$ and $\Delta n_{h,\omega}$ are the local excess of minority carriers (e: electrons in the p-region, h: holes in the n-region) above the equilibrium concentration [m^{-3}], D_e and D_h are the minority carrier diffusion coefficients [m^2s^{-1}], while τ_e and τ_h are the minority carrier lifetimes [s] that include radiative and non-radiative (Auger and Shockley-Read-Hall) recombination processes. The local monochromatic generation rates of EHPs within a given control volume j in the p- and n-regions are respectively given by:

$$g_{j,\omega} = \frac{1}{\hbar\omega} \kappa_{j,\omega}^{ib} \left(\frac{q_{\omega,\Delta z_j^p}^{abs}}{\Delta z_j^p \kappa_{j,\omega}} \right) \tag{3}$$

$$g_{j,\omega} = \frac{1}{\hbar\omega} \kappa_{j,\omega}^{ib} \left(\frac{q_{\omega,\Delta z_j^n}^{abs}}{\Delta z_j^n \kappa_{j,\omega}} \right) \tag{4}$$

where ω is the angular frequency [rad/s], $\hbar$ is the reduced Planck constant [1.0546×10^{-34} Js], $q_{\omega,\Delta z_j^{p,n}}^{abs}$ is the local monochromatic radiative heat flux absorbed by control volume j [$Wm^{-2}(rad/s)^{-1}$], $\kappa_{j,\omega}^{ib}$ is the local monochromatic interband absorption coefficient [m^{-1}] and $\kappa_{j,\omega}$ is the local monochromatic absorption coefficient that accounts for absorption by the lattice and the free carriers as well as the interband absorption process [m^{-1}].

The boundary conditions of the minority carrier diffusion equations at the cell-vacuum interface ($z = Z_0$) and at the cell-thermal management interface ($z = Z_4$) account for surface recombination of EHPs and are respectively given by:

$$D_e \frac{d\Delta n_{e,\omega}(Z_2)}{dz} = S_e \Delta n_{e,\omega}(Z_2) \tag{5}$$

$$D_h \frac{d\Delta n_{h,\omega}(Z_4)}{dz} = S_h \Delta n_{h,\omega}(Z_4) \tag{6}$$

where S_e and S_h are the minority carrier surface recombination velocities [ms^{-1}]. At the boundaries of the depletion region, it is assumed that the minority carriers are swept by the electric field at the p-n junction such that $\Delta n_{e,\omega}(Z_{dp}^p) = 0$ and $\Delta n_{h,\omega}(Z_{dp}^n) = 0$.

The photocurrent produced by the cell is the sum of contributions due to EHPs generated outside the depletion region diffusing to the boundaries of that zone and EHPs generated directly in the depletion region. In the depletion region, it is assumed that all EHPs contribute to the photocurrent:

$$J_{dp,\omega} = e \int_{Z_{dp}^n}^{Z_{dp}^p} g_{\lambda,\omega} dz \tag{7}$$

where e is the electron charge [1.6022×10^{-19}](eV)$^{-1}$] and the monochromatic photocurrent has units of Am^{-2}(rad/s)$^{-1}$. The photocurrent generated at the boundaries of the depletion region is calculated using the solution of the minority carrier diffusion equations:

$$J_{e,\omega} = eD_e \frac{d\Delta n_{e,\omega}(Z_{dp}^p)}{dz} \tag{8}$$

$$J_{h,\omega} = -eD_h \frac{d\Delta n_{h,\omega}(Z_{dp}^n)}{dz} \tag{9}$$

The total photocurrent J_{ph} is calculated by integrating the sum of Eqs. (7), (8) and (9) over the frequency from ω_g to infinity, where ω_g is the absorption bandgap of the cell in rad/s ($\omega_g = E_g e/\hbar$).

Heat transport within the cell is modeled via the one-dimensional steady-state energy equation with heat generation:

$$k \frac{d^2 T_{cell}(z)}{dz^2} + Q(z) = 0 \tag{10}$$

where k is the thermal conductivity of the cell [Wm^{-1}K^{-1}]. The local volumetric heat generation [Wm^{-3}] is defined as:

$$Q(z) = -Q_{LEC}(z) + Q_T(z) + Q_{NRR}(z) - Q_{RR}(z) \tag{11}$$

Bulk non-radiative recombination, Q_{NRR}, is a heat generation process due to EHPs recombining before reaching the depletion region. EHP recombination may also result in radiation emission, Q_{RR}, which has a cooling effect on the cell. These two contributions are computed from the solution of the minority carrier diffusion equations[25]. The local radiative source term, Q_{LEC}, represents the balance between thermal emission and absorption by the lattice and the free carriers. Finally, heat dissipation within the cell by thermalization is accounted for via the term Q_T. These last two contributions are calculated from the solution of the near-field thermal radiation problem[25].

At the cell boundaries, internal heat conduction and surface recombination of EHPs are balanced with an external heat flux. At the cell-vacuum interface ($z = Z_2$), the external heat flux is nil such that the boundary condition is given by:

$$k \frac{dT_{cell}(Z_2)}{dz} = S_e e E_g \int_{\omega_g}^{\infty} \Delta n_{e,\omega}(Z_2) d\omega \tag{12}$$

The boundary condition at $z = Z_4$ adjacent to the thermal management system includes the external heat flux due to convection:

$$-k \frac{dT_{cell}(Z_4)}{dz} = h_\infty \left[T_{cell}(Z_4) - T_\infty \right] \tag{13}$$

where surface recombination is neglected due to the large thickness of the cell[16].

Solution of the energy equation provides an updated temperature of the cell. The radiative, electrical and thermophysical properties of the cell, given in Ref. 25, are then calculated at the updated cell temperature. Note that the temperature-dependent dielectric function of the cell is calculated from the model

proposed by Adachi[47] for $E \geq E_g$; for $E < E_g$, the dielectric function is modeled as a Lorentz-Drude model with parameters determined by Patrini *et al.*[48] The temperature dependence of the cell absorption bandgap is computed using Varshni's equation, $E_g(T_{cell}) = E_g(0) - \delta T_{cell}^2/(T_{cell} + \beta)$ where $E_g(0)$ is the bandgap at 0 K and takes a value of 0.806 eV; the parameters δ and β are 4.2×10^{-4} eV/K and 140 K, respectively, for GaSb[49]. The computations are repeated until the cell temperature converges. It has been verified that a relative convergence criterion of 10^{-4} on the cell temperature is sufficient and was used in all simulations.

Once convergence is reached, the minority carrier diffusion equations are solved in dark conditions ($g_{op}(z) = 0$) for a series of forward biases V_f [V] in order to compute the dark current J_0 [Am^{-2}][25]. The photocurrent-voltage (J-V) characteristic of the nano-TPV device is then determined by calculating $J(V_f) = J_{ph} - J_0(V_f)$ as a function of the forward bias starting with $V_f = 0$. The maximum power output P [Wm^{-2}] of the nano-TPV device is determined directly from the J-V characteristic, and the conversion efficiency η_c is calculated as the ratio of the maximum power output over the total radiation absorbed by the cell.

References

1. Joulain, K., Mulet, J.-P., Marquier, F., Carminati, R. & Greffet, J. J. Surface electromagnetic waves thermally excited: Radiative heat transfer, coherence properties and Casimir forces revisited in the near field. *Surf. Sci. Rep.* **57,** 59–112 (2005).
2. Kittel, A. *et al.* Near-Field Heat Transfer in a Scanning Thermal Microscope. *Phys. Rev. Lett.* **95,** 224301 (2005).
3. Hu, L., Narayanaswamy, A., Chen, X. Y. & Chen, G. Near-field thermal radiation between two closely spaced glass plates exceeding Planck's blackbody radiation law. *Appl. Phys. Lett.* **92,** 133106 (2008).
4. Shen, S., Narayanaswamy, A. & Chen, G. Surface phonon polaritons mediated energy transfer between nanoscale gaps. *Nano Lett.* **9,** 2909–2913 (2009).
5. Rousseau, E. *et al.* Radiative heat transfer at the nanoscale. *Nat. Photonics* **3,** 514–517 (2009).
6. Ottens, R. S. *et al.* Near-Field Radiative Heat Transfer between Macroscopic Planar Surfaces. *Phys. Rev. Lett.* **107,** 014301 (2011).
7. Shen, S., Mavrokefalos, A., Sambegoro, P. & Chen, G. Nanoscale thermal radiation between two gold surfaces. *Appl. Phys. Lett.* **100,** 233114 (2012).
8. Worbes, L., Hellmann, D. & Kittel, A. Enhanced near-field heat flow of a monolayer dielectric island. *Phys. Rev. Lett.* **110,** 134302 (2013).
9. Francoeur, M. Near-field radiative energy transfer: Nanostructures feel the heat. *Nat. Nanotechnol.* **10,** 206–208 (2015).
10. Song, B. *et al.* Enhancement of near-field radiative heat transfer using polar dielectric thin films. *Nat. Nanotechnol.* **10,** 253–258 (2015).
11. Fu, C. J. & Zhang, Z. M. Nanoscale radiation heat transfer for silicon at different doping levels. *Int. J. Heat Mass Tran.* **49,** 1703–1718 (2006).
12. Mulet, J.-P., Joulain, K., Carminati, R. & Greffet, J.-J. Enhanced radiative heat transfer at nanometric distances. *Nanosc. Micros. Therm.* **6,** 209–222 (2002).
13. Whale, M. D. A Fluctuational electrodynamics analysis of microscale radiative heat transfer and the design of microscale thermophotovoltaic devices, PhD Thesis, MIT, Cambridge, 1997.
14. Whale, M. D. & Cravalho, E. G. Modeling and performance of microscale thermophotovoltaic energy conversion devices. *IEEE T. Energy Conver.* **17,** 130–142 (2002).
15. Narayanaswamy, A. & Chen, G. Surface modes for near field thermophotovoltaics. *Appl. Phys. Lett.* **82,** 3544–3546 (2003).
16. Laroche, M., Carminati, R. & Greffet, J.-J. Near-field thermophotovoltaic energy conversion. *J. Appl. Phys.* **100,** 063704 (2006).
17. Ilic, O., Jablan, M., Joannopoulos, J. D., Celanovic, I. & Soljačić, M. Overcoming the black body limit in plasmonic and graphene near-field thermophotovoltaic systems. *Opt. Express* **20,** A366–A384 (2012).
18. Simovski, C., Stanislav, M., Nefedov, I. & Tretyakov, S. Optimization of radiative heat transfer in hyperbolic metamaterials for thermophotovoltaic applications. *Opt. Express* **21,** 14988–15013 (2013).
19. Messina, R. & Ben-Abdallah, P. Graphene-based photovoltaic cells for near-field thermal energy conversion. *Scientific Reports* **3,** 1383 (2013).
20. Svetovoy, V. B. & Palasantzas, G. Graphene-on-silicon near-field thermophotovoltaic cell. *Phys. Rev. Applied* **2,** 034006 (2014).
21. Park, K., Basu, S., King, W. P. & Zhang, Z. M. Performance analysis of near-field thermophotovoltaic devices considering absorption distribution. *J. Quant. Spectrosc. Ra.* **109,** 305–316 (2008).
22. Bright, T. J., Wang, L. P. & Zhang, Z. M. Performance of near-field thermophotovoltaic cells enhanced with a backside reflector. *J. Heat Transfer* **136,** 062701 (2014).
23. Mikyung, L., Jin, S., Lee, S. S. & Lee, B. J. Graphene-assisted Si-InSb thermophotovoltaic system for low temperature applications. *Opt. Express* **23,** A240–A253 (2015).
24. Elzouka, E. & Ndao, S. Towards a near-field concentrated solar thermophotovoltaic microsystem: Part I – Modeling. *Sol. Energy*, doi: 10.1016/j.solener.2015.02.007, in press (2015).
25. Francoeur, M., Vaillon, R. & Mengüç, M. P. Thermal Impacts on the performance of nanoscale-gap thermophotovoltaic power generators. *IEEE T. Energy Conver.* **26,** 686–698 (2011).
26. DiMatteo, R. S. *et al.* Enhanced photogeneration of carriers in a semiconductor via coupling across a nonisothermal nanoscale vacuum gap. *Appl. Phys. Lett.* **79,** 1894–1896 (2001).
27. DiMatteo, R. S. *et al.*, Micron-gap thermophotovoltaics (MTPV). Presented at Thermophotovoltaic Generation of Electricity: 5th Conference, Rome, Italy 16-19 September 2002 (Vol. 653). American Institute of Physics (2003, January 25).
28. DiMatteo, R. S. *et al.*, Micron-gap thermophotovoltaics (MTPV). Presented at Thermophotovoltaic Generation of Electricity: 6th Conference, Freiburg, Germany 14-16 June 2004 (Vol. 738). American Institute of Physics (2004, November 30).
29. Hanamura, K. & Mori, K., Nano-gap TPV generation of electricity through evanescent wave in near-field above emitter surface. Presented at Thermophotovoltaic Generation of Electricity: 7th Conference, Madrid, Spain 25-27 September 2006 (Vol. 890). American Institute of Physics (2007, February 22).
30. Hanamura, K., Fukai, H., Srinivasan, E., Asano, M. & Masuhara, T., Photovoltaic generation of electricity using near-field radiation. Presented at ASME/JSME 2011 8th Thermal Engineering Joint Conference, Honolulu, HI, USA 13-17 March 2011. *doi: 10.1115/AJTEC2011-44513* (2011).
31. Yoshida, I., Ashida, Y. & Hanamura, K., Thermophotovoltaic generation of electricity by GaSb schottky cell using evanescent effect. Presented at International Workshop on Nano-Micro Thermal Radiation, Matsushima, Miyagi, Japan 23-25 May 2012. Tohoku University Global COE Program (2012, May 23).

32. Dupré, O. & Vaillon, R. Optimizations of photovoltaic cells including the minimization of internal heat sources. *J. Renew. and Sust. Ener.* **6**, 011201 (2014).
33. Palik, E. D. *Handbook of Optical Constants of Solids* (vol. 1, San Diego, 1998).
34. Francoeur, M., Mengüç, M. P. & Vaillon, R. Solution of near-field thermal radiation in one-dimensional layered media using dyadic Green's functions and the scattering matrix method. *J. Quant. Spectrosc. Ra.* **110**, 2002–2018 (2009).
35. Biehs, S.-A., Rousseau, E. & Greffet, J.-J. Mesoscopic description of radiative heat transfer at the nanoscale. *Phys. Rev. Lett.* **105**, 234301 (2010).
36. Tsurimaki, Y. *et al.* Reducing thermal radiation between parallel plates in the far-to-near field transition regime. Presented at 15th International Heat Transfer Conference, Kyoto, Japan 10-15 August 2014. *doi: 10.1615/IHTC15.rad.009188* (2014).
37. Francoeur, M., Mengüç, M. P. & Vaillon, R. Coexistence of multiple regimes for near-field thermal radiation between two layers supporting surface phonon polaritons in the infrared. *Phys. Rev. B* **84**, 075436 (2011).
38. Basu, S. & Zhang, Z. M. Ultrasmall penetration depth in nanoscale thermal radiation. *Appl. Phys. Lett.* **95**, 133104 (2009).
39. Martin, D. & Algora C. Temperature-dependent GaSb material parameters for reliable thermophotovoltaic cell modeling. *Semicond. Sci. Technol.* **10**, 1040 (2004).
40. Xiong, K., Lu, S., Jiang, D., Dong, J. & Yang, H. Effective recombination velocity of textured surfaces. *Appl. Phys. Lett.* **96**, 193107 (2010).
41. Agostinelli, G. *et al.* Very low surface recombination velocities on p-type silicon wafers passivated with a dielectric with fixed negative charge. *Sol. Energ. Mat. Sol. C.* **90**, 3438–3443 (2006).
42. Werner, F. *et al.* Very low surface recombination velocities on p- and n-type c-Si by ultrafast spatial atomic layer deposition of aluminum oxide. *Appl. Phys. Lett.* **97**, 162103 (2010).
43. Saint-Cast, P. *et al.* Very low surface recombination velocity on p-type c-Si by high-rate plasma-deposited aluminum oxide. *Appl. Phys. Lett.* **95**, 151502 (2009).
44. Hoex, B., Heil, S. B. S., Langereis, E., van de Sanden, M. C. M. & Kessels, W. M. M. Ultralow surface recombination of c-Si substrates passivated by plasma assisted atomic layer deposited Al_2O_3. *Appl. Phys. Lett.* **89**, 042112 (2006).
45. Vaillon, R., Robin, L., Muresan, C. & Ménézo, C. Modeling of coupled spectral radiation, thermal and carrier transport in a silicon photovoltaic cell. *Int. J. Heat Mass Tran.* **49**, 4454–4468 (2006).
46. Gonzalez-Cuevas, J. A., Refaat, T. F., Abedin, M. N. & Elsayed-Ali, H. E. Modeling of the temperature-dependent spectral response of $In_{1-x}Ga_xSb$ infrared photodetectors. *Opt. Eng.* **45**, 044001 (2006).
47. Adachi, S. *Properties of Group-IV, III-V and II-VI Semiconductors* (John Wiley and Sons, 2005).
48. Patrini, M. *et al.* Optical functions of bulk and epitaxial GaSb from 0.0025 to 6eV. *Solid State Commun.* **101**, 93–98 (2007).
49. Gonzalez-Cuevas, J. A., Refaat, T. F., Abedin, M. N. & Elsayed-Ali, H. E. Calculation of temperature alloy composition effects on the optical properties of $Al_xGa_{1-x}As_ySb_{1-y}$ and $Ga_xIn_{1-x}As_ySb_{1-y}$ in the spectral range 0.5–6 eV. *J. Appl. Phys.* **102**, 014504 (2007).

Acknowledgements

This work was supported by the National Science Foundation under Grant No. CBET-1253577.

Author Contributions

The work was conceived by M.P.B., M.F. and R.V. The simulations were performed by M.P.B. under the supervision of M.F. with inputs from R.V., O.D., E.B. and P.-O.C. The manuscript was written by M.P.B. and M.F. with comments from all authors.

Additional Information

Supplementary information accompanies this paper at http://www.nature.com/srep

Competing financial interests: The authors declare no competing financial interests.

How to cite this article: Bernardi, M. P. *et al.* Impacts of propagating, frustrated and surface modes on radiative, electrical and thermal losses in nanoscale-gap thermophotovoltaic power generators. *Sci. Rep.* **5**, 11626; doi: 10.1038/srep11626 (2015).

Supplemental Information: Impacts of propagating, frustrated and surface modes on radiative, electrical and thermal losses in nanoscale-gap thermophotovoltaic power generators

Michael P. Bernardi,[1,a)] Olivier Dupré,[2] Etienne Blandre,[2] Pierre-Olivier Chapuis[2], Rodolphe Vaillon,[2,b)] and Mathieu Francoeur[1,c)]

[1]Radiative Energy Transfer Lab, Department of Mechanical Engineering, University of Utah, Salt Lake City, UT 84112, USA

[2]Université de Lyon, CNRS, INSA-Lyon, UCBL, CETHIL, UMR5008, F-69621 Villeurbanne, France

[a)] Electronic mail: michael.bernardi@utah.edu
[b)] Electronic mail: rodolphe.vaillon@insa-lyon.fr
[c)] Electronic mail: mfrancoeur@mech.utah.edu

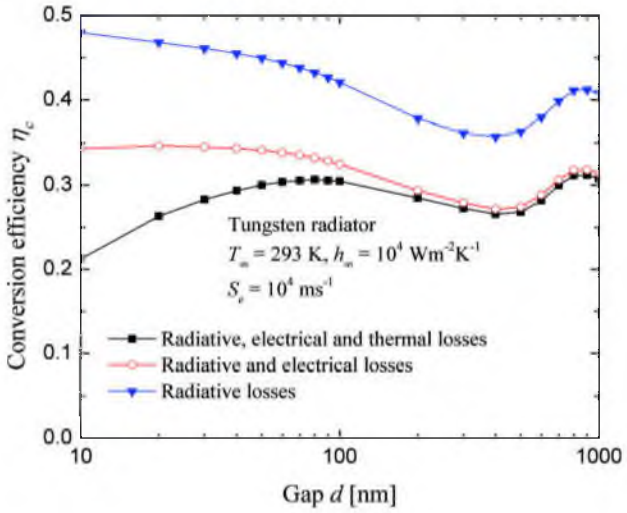

(a)

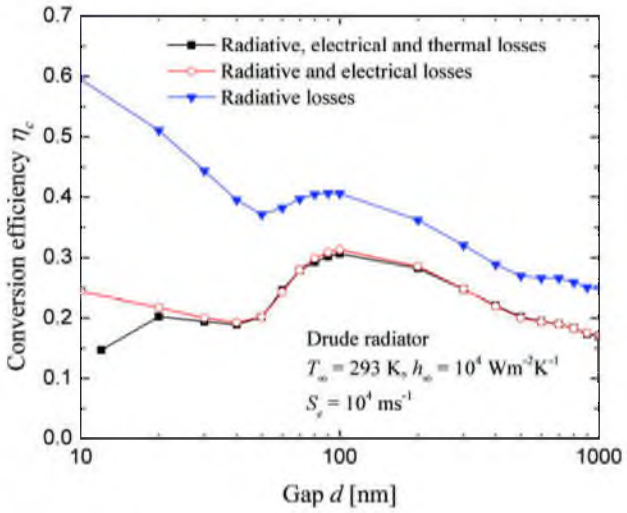

(b)

Figure S.1. Conversion efficiency as a function of the vacuum gap thickness and the type of losses considered: (a) tungsten radiator. (b) Drude radiator.

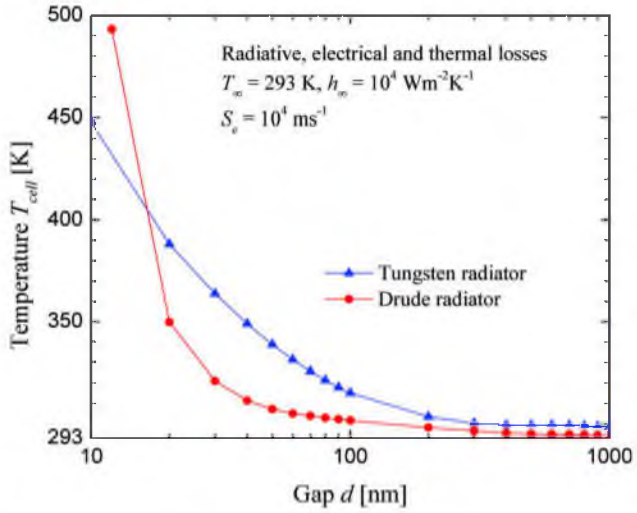

Figure S.2. Equilibrium cell temperature as a function of the vacuum gap thickness for tungsten and Drude radiators.

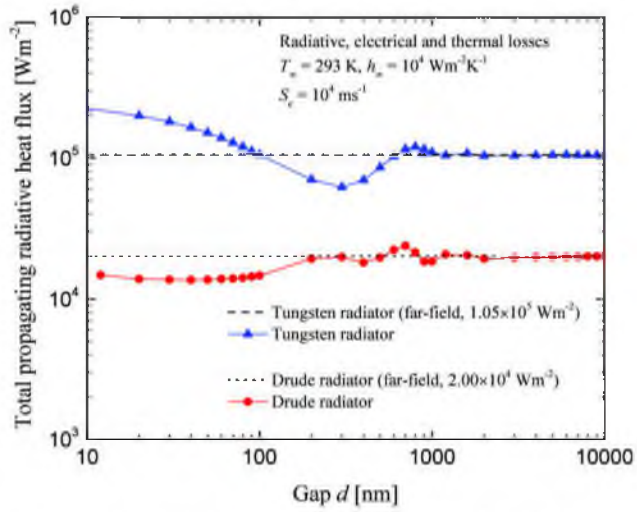

Figure S.3. Total propagating radiative heat flux absorbed by the cell as a function of the vacuum gap thickness for tungsten and Drude radiators.

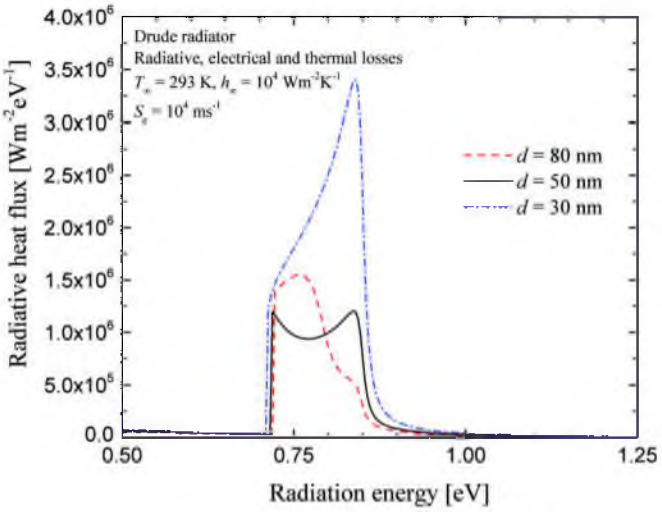

Figure S.4. Spectral distribution of radiative heat flux at the surface of the cell ($z = Z_2$) for vacuum gap thicknesses of 30, 50 and 80 nm (Drude radiator).

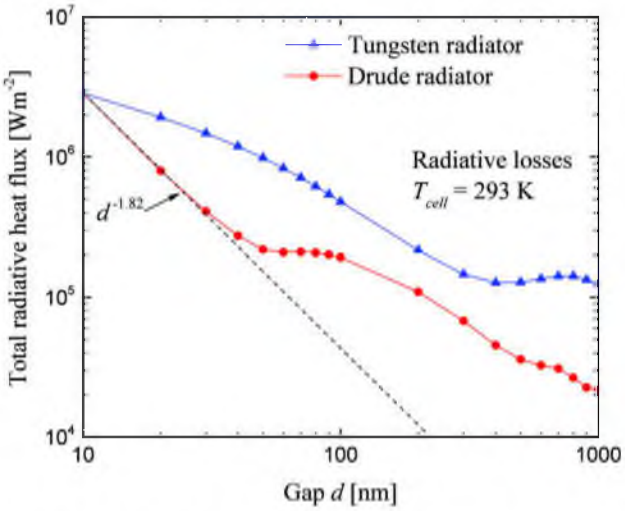

Figure S.5. Total radiative flux absorbed by the cell as a function of the vacuum gap thickness for tungsten and Drude radiators.

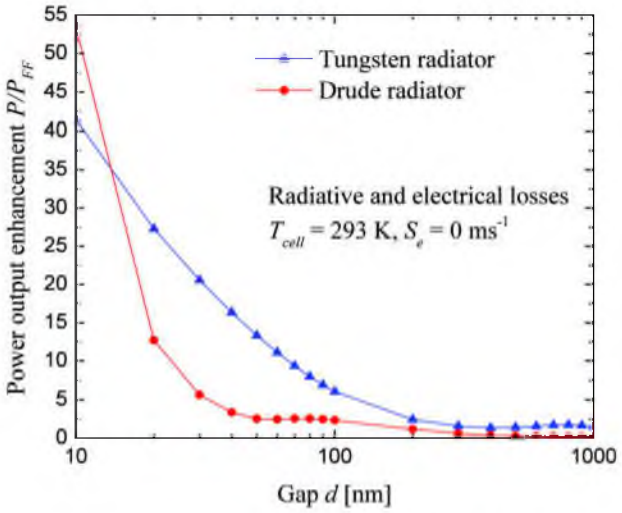

Figure S.6. Power output enhancement as a function of the vacuum gap thickness when neglecting surface recombination velocity and thermal losses for tungsten and Drude radiators.

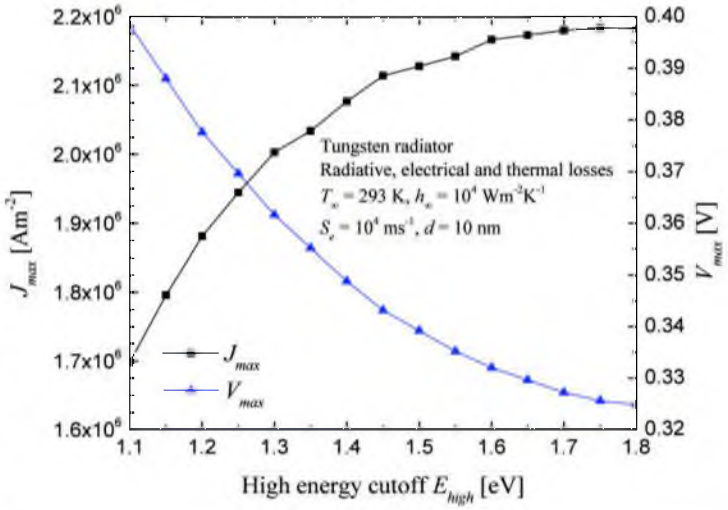

Figure S.7. Photocurrent J_{max} and potential V_{max} at maximum power output as a function of the high energy cutoff E_{high}.

Figure S.7 shows photocurrent J_{max} and voltage V_{max} at the maximum power output as a function of the high energy cutoff E_{high}. As expected, J_{max} increases as E_{high} increases due to a larger number of EHPs generated. Conversely, V_{max} decreases as E_{high} increases because of an increasing thermalization heat source and consequently a rise in temperature leading to a larger dark current.

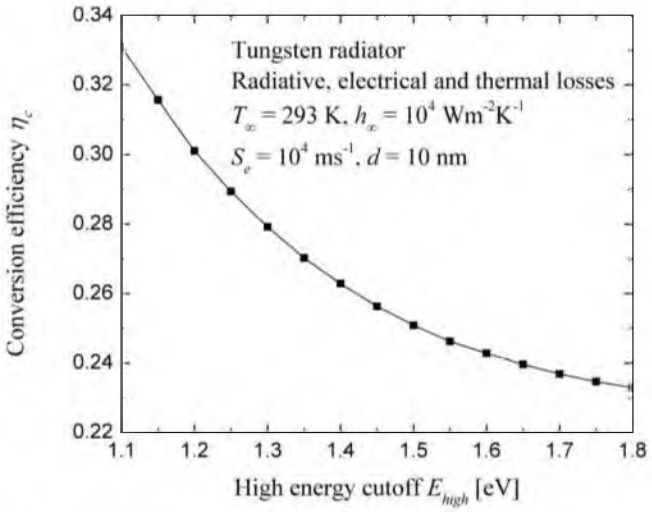

Figure S.8. Conversion efficiency as a function of the high energy cutoff E_{high} for a tungsten radiator.

CHAPTER 4

LITERATURE SURVEY OF NANOSCALE-GAP THERMOPHOTOVOLTAIC AND NEAR-FIELD RADIATIVE HEAT TRANSFER MEASUREMENTS

Prior to the development of functional nanoscale-gap thermophotovoltaic (nano-TPV) power generators, radiative heat transfer that is dominated by evanescent modes must first be well understood experimentally. Measurements of radiative heat flux at nanosize separation gaps between an emitter and receiver have been achieved between a microsize sphere and a planar surface [1-9], between a sharp tip and a planar surface [10-12] and between micro/nanostructures [13-17]. These results showed good agreement with predictions based on fluctuational electrodynamics. On the other hand, experimental validation of near-field radiative heat transfer between macroscopic planar surfaces separated by a nanosize gap has not been shown definitively [18-28]. Generating usable levels of power in nano-TPV devices requires thermal radiation to be exchanged between macroscale planar surfaces. Nonetheless, there has been limited work on nano-TPV devices [29-34], but the results thus far have been mostly qualitative.

In this chapter, the only experimental measurements on nano-TPV devices are presented. Definitive results relating gap size to power generation enhancement are shown to be lacking. Prior to making meaningful measurements of power generation in a nano-TPV device, radiative heat transfer between surfaces must be experimentally

quantified. Near-field radiative heat transfer measurements with respect to geometry is presented and analyzed in terms of applicability to nano-TPV power generation.

4.1 Nano-TPV Measurements

Only two groups [29-34] have conducted experiments on nano-TPV systems. DiMatteo et al. [29,30] experimented on a system comprised of a silicon (Si) emitter and an indium arsenide (InAs) cell cooled by a thermoelectric module. The gap was maintained via 1-μm-tall silicon dioxide (SiO_2) posts. The experimental setup allowed for a slight variation of the gap using a piezoactuator flexing the heater chip by fractions of microns. However, the distance the heater chip flexed was not documented. By decreasing the gap for emitter temperatures of 348 K, 378 K and 408 K, it was observed that the short-circuit current increased by a factor of five. A dynamic test was also performed, where the piezoactuator oscillated at various frequencies from 200 to 1000 Hz, thus also causing the vacuum gap to oscillate. As depicted in Figure 4.1, results showed that variations of the short-circuit current followed nearly in-phase with the gap oscillation frequency, thus leading the authors to conclude that the increase of the current was due to tunneling of evanescent modes. As pointed out by the authors, while this work qualitatively demonstrated near-field enhancement, no quantitative data was reported. DiMatteo et al. [31] later refined the experimental device using indium gallium arsenide (InGaAs) cells. The updated setup employed tubular spacers minimizing heat conduction between the radiator and the cell, and allowed measurements of the full *J-V* curve (i.e., current versus voltage). Although an enhancement of the power generated was observed, its actual magnitude was uncertain.

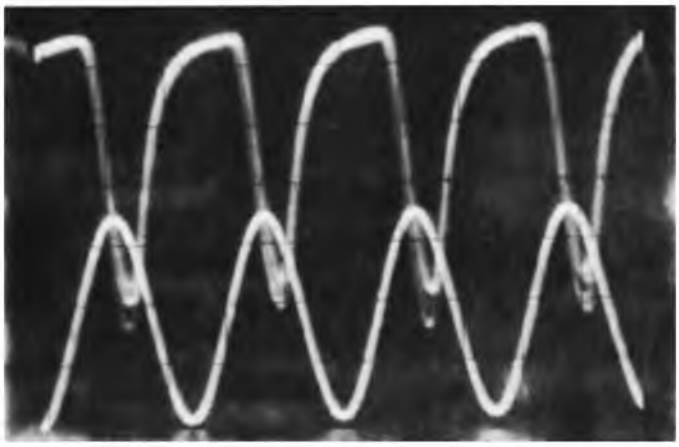

Figure 4.1 Experimental results from DiMatteo et al. [29]. The bottom curve is the piezo drive voltage (increasing voltage is up, corresponding to a decreasing gap size). The top curve is the TPV cell short-circuit current (increased current is down).

Hanamura and Mori [32] also conducted nano-TPV experiments where the emitter and cell was made of tungsten and gallium antimonide (GaSb), respectively. The temperature difference was maintained via a carbon dioxide (CO_2) laser and a water-cooled copper block. In order to avoid heat transfer by conduction, the radiator and the cell were mounted separately. The gap and the parallelism between the surfaces were controlled via micro-stages. *J-V* characteristics were reported for large gaps (few tens to few hundreds of micrometers). The temperature of the emitter, T, and the power generated, P, were reported in the near field for gap ranges around 1 μm (i.e., uncertainty of 1 μm in the measured gap) and are shown in Figure 4.2. Despite these uncertainties, an enhancement of the power generated was qualitatively observed. Recent results [33] using the same apparatus showed an enhancement of the short-circuit current by a factor of 3 for separation gaps below 1.5 μm. An enhancement by a factor of 3.7 of the short-circuit current was later reported [34].

The nano-TPV experiments discussed in this section only qualitatively show that

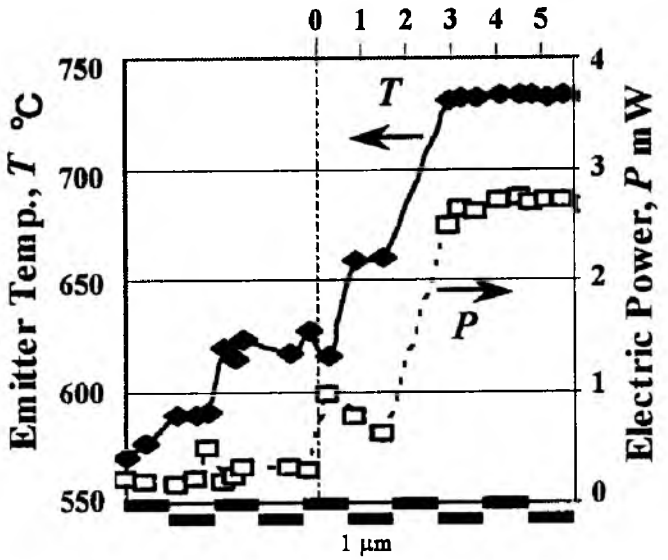

Figure 4.2 Output power, P, and emitter temperature, T, as a function of gap size from Hanamura and Mori [32].

power generation in TPV cells can be enhanced due to the contribution of evanescent modes. This can be attributed to the lack of experimental measurements of near-field radiative heat exchanged by macroscale planar surfaces. The following sections of this chapter discuss near-field radiative heat transfer measurements in a variety of geometries. It is shown that in the majority of the experiments, the geometry studied is not suited for nano-TPV power generation.

4.2 Radiative Heat Transfer Measurements between a Sharp Tip and a Planar Surface

Although enhancement of radiative energy transfer due to the contribution of evanescent waves was first demonstrated in 1968 for cryogenic temperatures [25-28], modern experiments on near-field radiative heat transfer near ambient temperature were not conducted until 1994 by Xu et al. [24] The purpose of this work was to demonstrate the heat transfer between a scanning thermal microscopy (SThM) probe and a sample. The needle of the SThM head was made of indium wire and heated with a heating coil.

The needle served as the emitter while the receiving surface was a thermocouple consisting of $Ag_{0.9}/Cu_{0.1}Cr$. The heat transfer enhancement observed by the authors was deemed inconclusive due to a liquid film between the SThM probe and the thermocouple.

Kittel et al. [10] measured near-field radiative heat transfer between a SThM tip near ambient temperature and a gold or gallium nitride (GaN) substrate near 100 K. Figure 4.3 shows heat rate, ΔP, as a function of gap size, z, between a SThM tip and a gold substrate. Experimental results differed from predictions based on fluctuational electrodynamics at gap sizes less than 10 nm. Later on, Kittel et al. [11] used a similar experimental setup to measure the local density of states (LDOS) of a gold substrate. By maintaining a gap size of 9 nm, they were able to create a topographic image of the substrate.

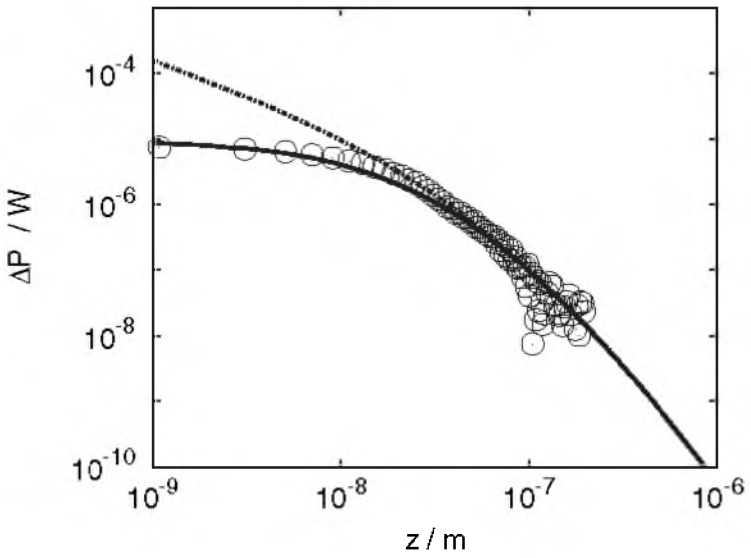

Figure 4.3 Heat rate, ΔP, as a function gap size, z, between SThM tip and a gold substrate from Kittel et al. [10]. The dashed line represents predictions based on fluctuational electrodynamics.

Most recently, Kim et al. [12] investigated heat transfer between a SThM probe tip and a planar substrate at gap sizes as small as 2 nm. Conductance between tips and surfaces composed of silicon-silicon (Si-Si), silicon nitride-silicon nitride (Si_3N_4-Si_3N_4) and gold-gold (Au-Au) was measured. The SThM probe was maintained at 310 K while the substrate was heated to 425 K. Results show fluctuational electrodynamics to be valid in the extreme near field. Figure 4.4 depicts the results for conductance, $G_{eNFRHT,Au\text{-}Au}$, as a function of gap size for the Au-Au configuration.

Although the results from Kittel et al. [10] differed from predictions at gap sizes below 10 nm, later experiments [12] showed fluctuational electrodynamics predictions to be valid at gap sizes as small as 2 nm. Furthermore, it was theoretically determined that the fluctuational electrodynamics framework is applicable to gap sizes as small as 1 nm [35]. Regardless of the gap sizes presented, the total energy transferred between the emitter and receiver is small such that a sharp tip-planar surface geometry is not applicable to nano-TPV power generation.

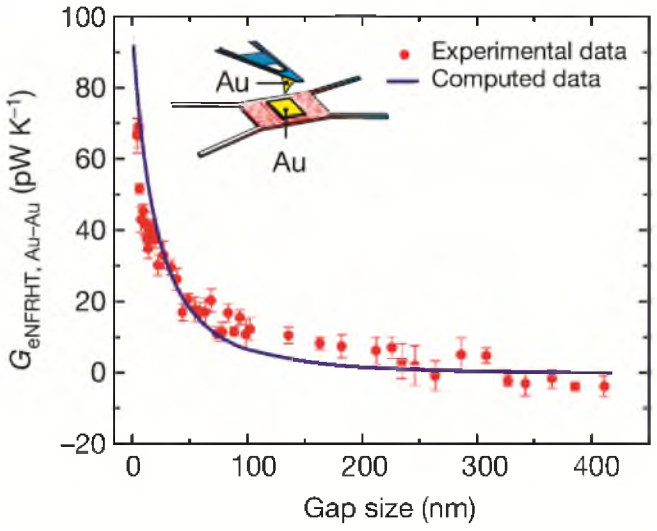

Figure 4.4 Thermal conductance, $G_{eNFRHT,Au\text{-}Au}$, as a function of gap size between a gold SThM tip and a gold substrate from Kim et al. [12].

4.3 Radiative Heat Transfer Measurements between a Microsphere and a Planar Surface

Narayanaswamy et al. [1,2] conducted an experiment to study near-field radiative heat transfer between a 50-μm-diameter SiO_2 sphere and a glass plate. A laser was used to heat the sphere and create a temperature differential of approximately 50 K relative to the surface. A 21% increase over blackbody predictions was observed at a gap spacing of 100 nm. Shen et al. [3] repeated the experiment from Narayanaswamy et al. [1,2] with different substrate materials. Gold and arsenic-doped Si substrates were used in addition to glass. According to their results depicted in Figure 4.5, they were able to achieve radiative heat flux three orders of magnitude greater than blackbody predictions at gap sizes as small as 30 nm. These experiments were repeated by Shen et al. [7] for a 50-μm-diameter gold sphere and a gold substrate. The thermal conductance at a gap size of 30 nm was observed to be larger than the blackbody limit by a factor of 80.

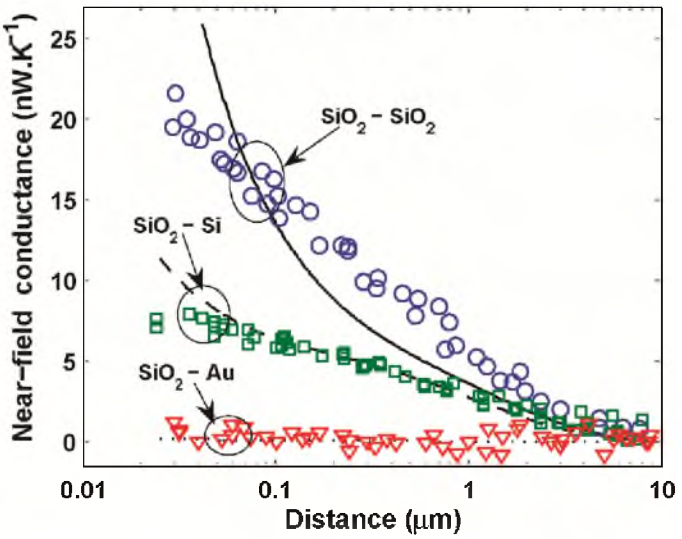

Figure 4.5 Near-field conductance as a function of gap size with respect to substrate material from Shen et al. [3].

Rousseau et al. [4] conducted experiments with a similar setup using a sphere-plane geometry. SiO_2 spheres with diameters of 40 μm and 22 μm served as the receivers. A borosilicate glass plate functioned as the emitter and was heated to 10 – 20 K above ambient temperature. The sphere and plate were separated by a vacuum gap ranging from 30 nm to 2.5 μm. Results demonstrated a clear and distinct dependence on gap distance. As can be seen in Figure 4.6, the experimental results agreed well with the theoretical predictions.

Van Zwol et al. [5] investigated the modulation of near-field radiative heat transfer when using phase change materials. Heat transfer was measured between a 40-μm-diameter SiO_2 sphere mounted to an atomic force microscope (AFM) cantilever at room temperature and thin films of vanadium dioxide (VO_2) (50 and 100 nm) deposited on a sapphire substrate heated to temperatures up to 375 K. Results revealed a decrease in heat transfer by a factor of five after the phase transition from semiconductor to metal occurs. Later, van Zwol et al. [6] used the same setup to measure near-field radiative heat transfer between a SiO_2 sphere and graphene epitaxially grown on a silicon carbide (SiC) substrate. Results revealed a significant increase in heat transfer due to the plasmons in the graphene at gap sizes less than 200 nm.

Shi et al. [9] measured radiation heat transfer between a 100-μm-diameter SiO_2 sphere and a planar hyperbolic metamaterial composed of an anodic aluminum oxide (AAO) absorber on which an array of vertically aligned nickel nanowires were grown. A laser was used to heat the sphere to approximately 323 K while the AAO-nickel nanowire substrate was maintained at 298 K. Figure 4.7 depicts experimental measurements for near-field conductance as a function of sphere-plate separation distance. Results show

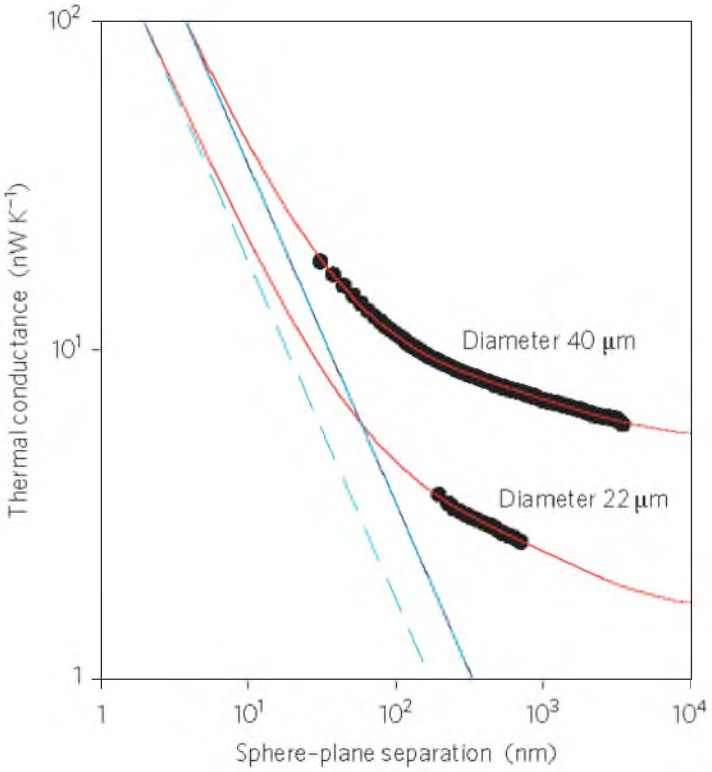

Figure 4.6 Thermal conductance as a function of sphere-plane separation with respect to sphere diameter from Rousseau et al. [4].

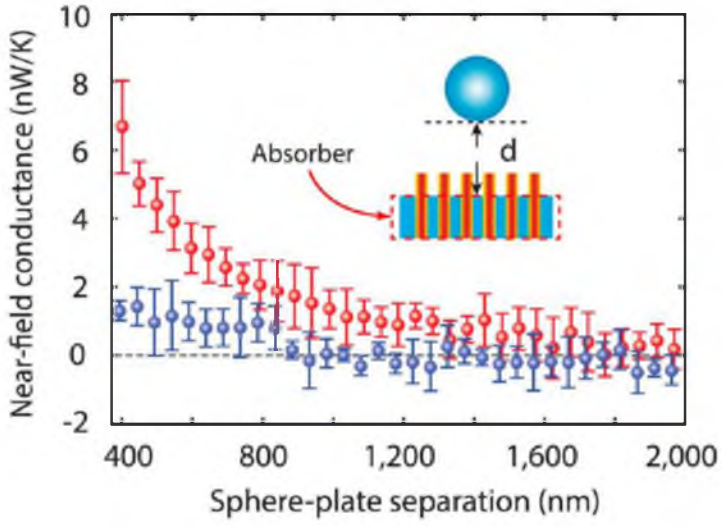

Figure 4.7 Near-field conductance as a function of separation gap from Shi et al. [9]. Blue circles indicate results for an absorber without nanowire protrusions while red circles indicate an absorber with nanowire protrusions.

that heat transfer between the sphere and the absorber with nickel nanowire protrusions can be enhanced by nearly one order of magnitude at a separation gap of 400 nm when compared to the case without the protrusions.

Song et al. [8] measured near-field radiative heat transfer between a 53-μm-diameter spherical SiO_2 emitter and a silicon nitride (Si_3N_4) planar surface coated with varying thicknesses of SiO_2 (50 nm – 3 μm) and a 100-nm-thick layer of gold near room temperature. A custom nanopositioner was able to vary the vacuum gap size from 20 nm to 10 μm. Figure 4.8 depicts experimental measurements of near-field conductance as a function of separation gap size with respect to film thicknesses. While results show there was no measureable enhancement for the case of the gold film, for the cases with SiO_2, significant radiative heat transfer enhancement was only realized when the separation gap was comparable to the film thickness. The authors concluded that surface modes in the SiO_2 films were responsible for the enhancement of near-field conductance.

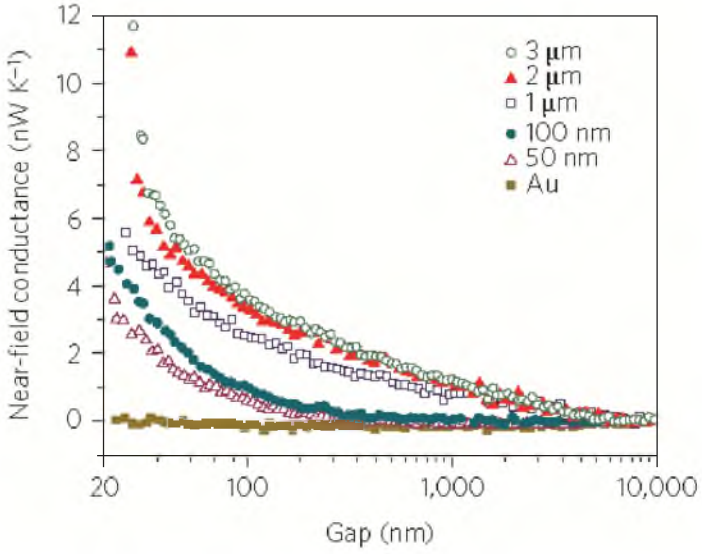

Figure 4.8 Near-field conductance as a function of gap size with respect to SiO_2 thickness from Song et al. [8].

Although gap sizes as small as 20 nm and heat transfer enhancements as large as three orders of magnitude have been achieved with a microsphere-planar surface geometry, this type of setup would not be conducive to nano-TPV power generation. Due to the relatively small area of heat transfer, only a modest amount of radiative energy can be exchanged between an emitter and receiver severely limiting the total electrical power that can be generated. The methods used in the previously mentioned experiments in this section would not be applicable to real engineering devices since they involve microspheres attached to AFM cantilevers.

4.4 Radiative Heat Transfer Measurements between Microstructures

Figure 4.9 depicts the results from Feng et al. [13] where a MEMS device capable of measuring near-field radiative heat transfer between two freestanding 77 × 77 μm^2 SiO_2 membranes separated by a 1-μm-thick vacuum gap is presented. The emitter is heated to temperatures ranging from 313 K to 396 K using a platinum resistor. Results showed the near-field component of the conductance, G_{nr}, was found to be over an order of magnitude greater than the far-field component, G_{fr}.

Using near-field thermal radiation, Guha et al. [14] cooled a 100 × 50 μm^2, 840-nm-thick SiO_2 membrane heated to initial temperatures of 460 K and 416 K by bringing it in to close proximity with a SiO_2 probe connected to a thermal reservoir at 300 K. As shown in Figure 4.10, the temperature change, ΔT, in the membrane was measured to be nearly -1.5 K at a separation gap of 350 nm and an initial temperature of 460 K.

St. Gelais et al. [15] measured near-field radiative heat transfer between two 200 μm × 500 nm Si_3N_4 beams coated with a 100-nm-thick layer of SiO_2 separated by a variable vacuum gap as small as 250 nm. The beams were fabricated using standard

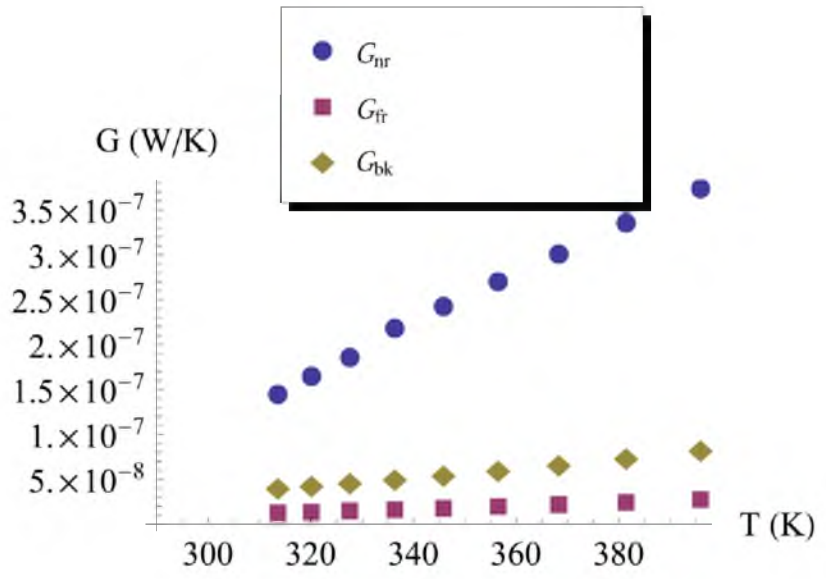

Figure 4.9 Conductance, G, as a function of emitter temperature, T, with respect to near-field, G_{nr}, far-field, G_{fr}, and blackbody conductance, G_{bk}, from Feng et al. [13].

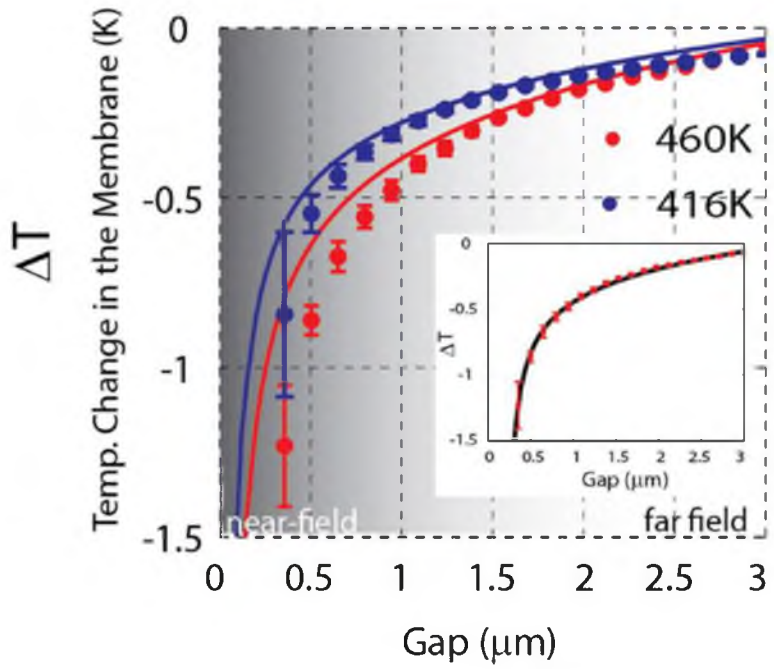

Figure 4.10 Membrane temperature change, ΔT, as a function of separation gap from Guha et al. [14]. Circles represent experimental measurements while the solid lines are theoretical predictions. The inset shows the fitting of the experimental data with the theoretical model.

nanofabrication techniques on a Si substrate. One beam serves as the receiver at 300 K while the second beam functions as an emitter at 430 K. Results show that conduction through the substrate accounts for less than 15% of the total heat transfer at the minimum gap size. Figure 4.11 shows experimental measurements agree with theoretical predictions based on fluctuational electrodynamics. At the minimum gap size, near-field radiative heat transfer exceeds the far-field value by a factor of seven. St. Gelais et al. [16] recently refined this experiment to measure radiative heat flux between SiC nanobeams separated by gaps as small as 42 nm. With a temperature difference of 260 K and a gap size of 42 nm, a heat transfer enhancement by nearly two orders of magnitude over the far-field limit was observed.

Song et al. [17] recently studied radiative heat transfer in a configuration similar to that in Ref. 8. Rather than using a 53-μm-diameter spherical emitter, radiative heat transfer was measured between 48 × 48 μm^2 parallel surfaces. Configurations consisting of SiO_2-SiO_2, Au-Au, SiO_2-Au and Au-Si surfaces were investigated. For the case of SiO_2-SiO_2, results showed an enhancement of thermal conductance of nearly three orders of magnitude when compared to the blackbody limit.

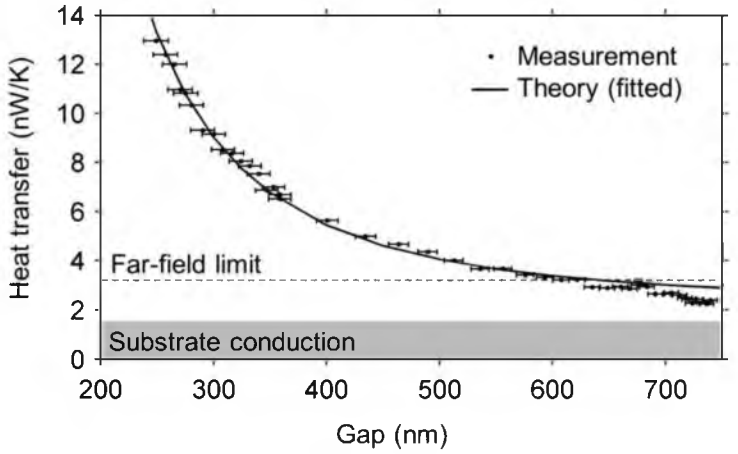

Figure 4.11 Heat transfer as a function of gap size from St. Gelais et al. [15].

In the microstructure geometry, a maximum enhancement factor of thermal conductance of nearly 1000 for gap sizes smaller than 100 nm was realized [17]. However, as with sharp tip-planar surface and microsphere-planar surface geometries, the microstructure geometry is also unsuitable for nano-TPV power generation due to the small heat transfer area exchanging radiation. Furthermore, the complex fabrication processes may make microstructure geometries prohibitively expensive for a real engineering device.

4.5 Radiative Heat Transfer Measurements between Planar Surfaces

A number of experimental investigations involving planar surfaces were performed from 1968 to 1994 [23-27]. Whale [36] reported the data from these experiments and concluded that they were inconsistent, suspect to invalidity, divergent from theoretical predictions, and insufficient to infer a general trend and length scale for near-field thermal radiation between planar surfaces.

More recent experiments involving 12.7-mm-diameter glass plates were conducted by Hu et al. [18], where the gap between the surfaces was maintained via polystyrene particles. Polystyrene was chosen as it has a low thermal conductivity (0.18 $Wm^{-1}K^{-1}$) and is transparent in the infrared band of the electromagnetic spectrum. The gap was assumed to be equivalent to the maximum particle size of 1.6 μm. Experimental results showed a flux exceeding the blackbody predictions by 35%, which match well with predictions based on fluctuational electrodynamics as shown in Figure 4.12. While the method used in this work is relatively simple, the gap between the surfaces is large, thus significantly limiting heat transfer enhancement.

Ottens et al. [19] measured near-field radiative heat transfer between 50×50 mm^2

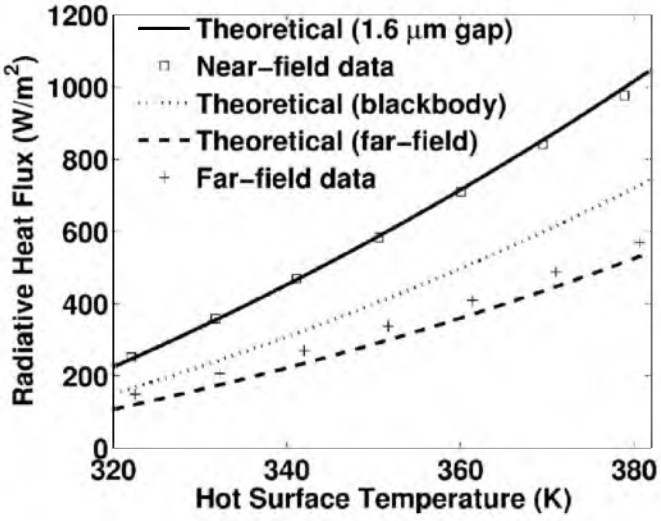

Figure 4.12 Radiative heat flux as a function of emitter temperature from Hu et al. [18].

sapphire surfaces. The setup employed three stepper motors allowing variations of the gap from 2 to 100 μm. The parallelism between the surfaces was monitored via capacitor plates. Results demonstrated an enhancement of the flux by 27% over the blackbody predictions. As shown in Figure 4.13, experimental measurements diverge from predictions as the gap size decreases. The complexity and size of the setup and precision gap control would prevent such a system from being used for an engineering device such as a nano-TPV power generator.

Figure 4.14 shows results from Ito et al. [20]. Near-field radiative heat transfer was measured between millimeter-sized quartz surfaces separated by quartz spacers. Test samples with gaps of 2.0 μm, 1.0 μm and 0.5 μm were measured. The receiver temperature was maintained at 293 K, while the emitter was heated to 298 K, 303 K, 308 K and 313 K. Results showed heat flux to be up to twice that of fluctuational electrodynamics predictions, indicating high parasitic conduction. Heat transfer via conduction would be severely detrimental to the performance of a nano-TPV device.

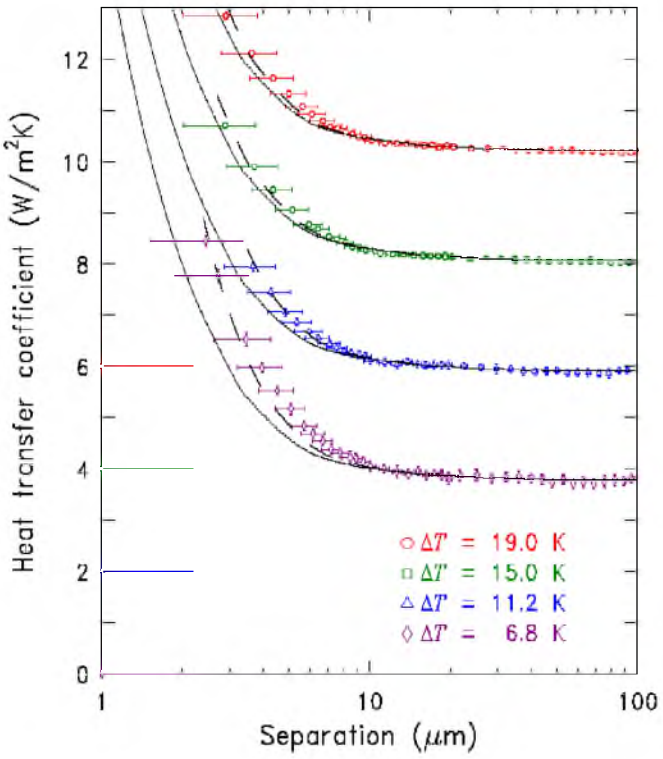

Figure 4.13 Heat transfer coefficient as a function of gap size and temperature difference from Ottens et al. [19]

Ijiro and Yamada [21] measured near-field radiative heat transfer between 25-mm-diameter SiO_2 plates with and without microcavities near 300 K separated by vacuum gaps ranging from 1 μm to 50 μm. Temperature differences of 4.1 K, 8.8 K and 19.5 K were investigated. As shown in Figure 4.15, experimental results agreed well with theoretical predictions and exhibited an increase over blackbody heat transfer by a factor of approximately 1.4 for the case of flat plates without microcavities.

The smallest gap size between planar surfaces thus far in the literature has been reported by Lim et al. [22]. Near-field radiative heat transfer between two microstrips (480 μm × 1.34 cm) of doped Si separated by a vacuum gap as small as 400 nm was measured. Since the gap size is much smaller than the width of the strips, any edge effects can be considered to be negligible. The receiver temperature is maintained at

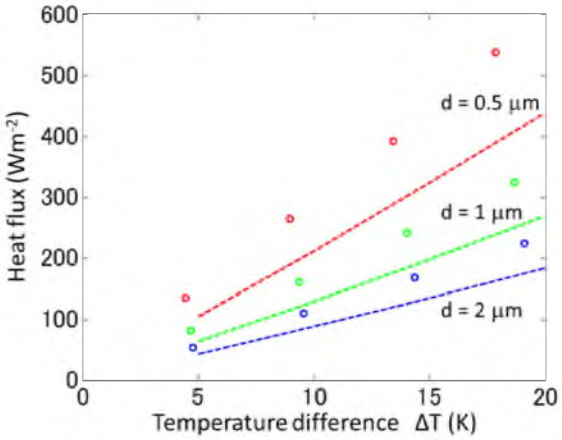

Figure 4.14 Heat flux as a function of temperature difference and gap size from Ito et al. [20]. Circles indicate experimental measurements while the dashed lines represent theoretical predictions.

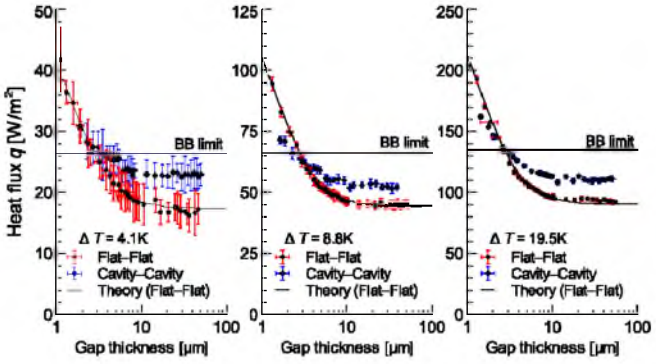

Figure 4.15 Heat flux, q, as a function of gap thickness with respect to temperature difference, ΔT, from Ijiro and Yamada [21].

298 K with a large aluminum heat sink while the emitter was heated to 371 K using a wire heater. As shown in Figure 4.16, the experimental measurements agree reasonably well with theoretical predictions and indicate a heat transfer coefficient 2.91 times greater at a gap size of 400 nm than that for a blackbody. The microsize strips exchanging radiation are small and suffer from the same drawback of the geometries discussed in the previous sections. Without macroscale planar surfaces, the total radiative energy that can be transferred will be small and therefore unsuitable for nano-TPV power generation.

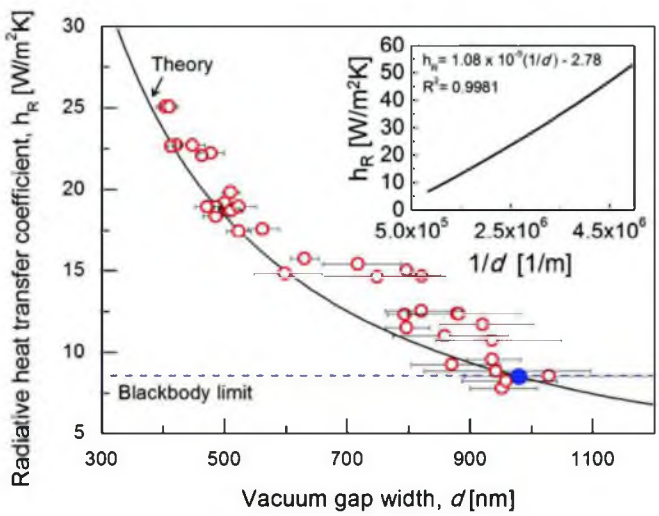

Figure 4.16 Heat transfer coefficient, h_R, as a function of vacuum gap width, d, from Lim et al. [22].

To summarize, two groups have qualitatively observed near-field enhancement of nano-TPV power generation, but no quantitative data has been reported. The maximum enhancement of photogenerated current documented thus far is by a factor of 5. Also, there is very little experimental data of near-field radiative heat flux between macroscale planar surfaces separated by a nanosize gap in the literature. The first necessary step in the development of a nano-TPV power generator is to measure the radiative heat flux between two macroscale surfaces separated by a nanosize gap. The research presented in Chapter 5 addresses this knowledge gap for the purpose of developing TPV devices operating at nanosize gaps.

4.6 References Cited

[1] A. Narayanaswamy and G. Chen, Phys. Rev. B **77**, 075125 (2008).

[2] A. Narayanaswamy, S. Chen, L. Hu, X.Y. Chen and G. Chen, Appl. Phys. A **96**, 357 (2009).

[3] S. Shen, A. Narayanaswamy and G. Chen, Nano Lett. **9**, 2909 (2009).

[4] E. Rousseau, A. Siria, G. Jourdan, S. Volz, F. Comin, J. Chevrier and J.-J. Greffet, Nature Photon. **3**, 514 (2009).

[5] P.J. van Zwol, L. Ranno and J. Chevrier, Phys. Rev. Lett. **108**, 234301 (2012).

[6] P.J. van Zwol, S. Thiele, C. Berger, W.A. de Heer and J. Chevrier, Phys. Rev. Lett. **109**, 264301 (2012).

[7] S. Shen, A. Mavrokefalos, P. Sambegoro and G. Chen, Appl. Phys. Lett. **100**, 233114 (2012).

[8] B. Song, Y. Ganjeh, S. Sadat, D. Thomson, A. Fiorino, V. Fernández-Hurtado, J. Feist, F.J. García-Vidal, J.C. Cuevas, P. Reddy and E. Meyhofer, Nat. Nanotechnol. **10**, 253 (2015).

[9] J. Shi, B. Liu, P. Li, L.Y. Ng and S. Shen, Nano Lett. **15**, 1217 (2015).

[10] A. Kittel, W. Müller-Hirsch, J. Parisi, S.-A. Biehs, D. Reddig and M. Holthaus, Phys. Rev. Lett. **95**, 224301 (2005).

[11] A. Kittel, U.F. Wischnath, J. Welker, O. Huth, F. Rüting and S.-A. Biehs, Appl. Phys. Lett. **93**, 193109 (2008).

[12]] K. Kim, B. Song, V. Fernández-Hurtado, W. Lee, W. Jeong, L. Cui, D. Thomson, J. Feist, M.T.H. Reid, F.J. García-Vidal, J.C. Cuevas, E. Meyhofer and P. Reddy, Nature **528**, 387 (2015).

[13] C. Feng, Z. Tang, J. Yu and C. Sun, Sensors **13**, 1998 (2013).

[14] B. Guha, C. Otey, C.B. Poitras, S. Fan and M. Lipson, Nano Lett. **12**, 4546 (2012).

[15] R. St-Gelais, B. Guha, L. Zhu, S. Fan and M. Lipson, Nano Lett. **14**, 6971 (2014).

[16] R. St-Gelais, L. Zhu, S. Fan and M. Lipson, Nat. Nanotechnol. **11** (2016).

[17] B. Song, D. Thompson, A. Fiorino, Y. Ganjeh, P. Reddy and E. Meyhofer, Nat. Nanotechnol. **11** (2016).

[18] L. Hu, A. Narayanaswamy, X.Y. Chen and G. Chen, Appl. Phys. Lett. **92**, 133106 (2008).

[19] R.S. Ottens, V. Quetschke, S. Wise, A.A. Alemi, R. Lundock, G. Mueller, D.H. Reitze, D.B. Tanner and B.F. Whiting, Phys. Rev. Lett. **107**, 014301 (2011).

[20] K. Ito, A. Miura, I. Hideo and H. Toshiyoshi, Appl. Phys. Lett. **106**, 083504 (2015).

[21] T. Ijiro and N. Yamada, Appl. Phys. Lett. **106**, 023103 (2015).

[22] M. Lim, S.S. Lee and B.J. Lee, Phys. Rev. B **91**, 195136 (2015).

[23] C.M. Hargreaves, Phys. Lett. **30A**, 491 (1969).

[24] J.-B. Xu, K. Läuger, R. Möller, K. Dransfield and I.H. Wilson, J. Appl. Phys. **76**, 7209 (1994).

[25] E.G. Cravalho, G.A. Domoto and C.L. Tien C.L., Measurements of thermal radiation of solids at liquid-helium temperatures, presented at the AIAA 3rd Thermophysics Conference, 1968.

[26] G.A. Domoto, R.F. Boehm and C.L. Tien, J. Heat Transfer **92**, 412 (1970).

[27] S.S. Kutatekadze, N.A. Rubtsov and Y.A. Bal'tsevich, Soviet Physics Doklady **8**, 577 (1979).

[28]] T. Kralik, P. Hanzelka, M. Zobac, V. Musilova, T. Fort and M. Horak, Phys. Rev. Lett. **109**, 224302 (2012).

[29] R.S. DiMatteo, P. Greiff, S.L. Finberg, K.A. Young-Waithe, H.K.H. Choy, M.M. Masaki and C.G. Fonstad, Appl. Phys. Lett. **79**, 1894 (2001).

[30] R.S. DiMatteo, P. Greiff, S.L. Finberg, K.A. Young-Waithe, H.K.H. Choy, M.M. Masaki and C.G. Fonstad, presented at the 5th Conference on Thermophotovoltaic Generation of Electricity, 2003.

[31] R.S. DiMatteo, P. Greiff, D. Seltzer, D. Meulenberg, E. Brown., E. Carlen, K. Kaiser, S. Finberg, H. Nguyen, J. Azarkevich, P. Baldasaro, J. Beausang, L. Danielson, M. Dashiell, D. DePoy, H. Ehsani, W. Topper and K. Rahner, presented at the 6th Conference on Thermophotovoltaic Generation of Electricity, 2004.

[32] K. Hanamura and K. Mori, presented at the 7th Conference on Thermophotovoltaic Generation of Electricity, 2007.

[33] K. Hanamura, H. Fukai, E. Srinivasan, M. Asano and T. Masuhara, Photovoltaic generation of electricity using near-field radiation, presented at the ASME/JSME 2011 8th Thermal Engineering Joint Conference, 2011.

[34] J. Yoshida, Y. Ashida and K. Hanamura, Thermophotovoltaic generation of electricity by GaSb schottky cell using evanescent effect, presented at the International Workshop on Nano-Micro Thermal Radiation, 2012.

[35] V. Chiloyan, J. Garg, K. Esfarjani and G. Chen, Nat. Commun. **6**, 6755 (2015).

[36] M.D. Whale and E.G. Cravalho, IEEE T. Energy Conver. **17**, 130 (2002).

CHAPTER 5

RADIATIVE HEAT TRANSFER EXCEEDING THE BLACKBODY LIMIT BETWEEN MACROSCALE PLANAR SURFACES SEPARATED BY A NANOSIZE VACUUM GAP

The following sections have been submitted to be published in *Nature Communications* as a paper titled "Radiative heat transfer exceeding the blackbody limit between macroscale planar surfaces separated by a nanosize vacuum gap." As such, it is to be treated as a stand-alone paper with its own references, sections and equations. Coauthors of the paper are Michael P. Bernardi, Daniel Milovich and Mathieu Francoeur.

5.1 Radiative Heat Transfer Exceeding the Blackbody Limit between Macroscale Planar Surfaces Separated by a Nanosize Vacuum gap

5.1.1 Abstract

Using Rytov's framework of fluctuational electrodynamics [1], Polder and Van Hove [2] theoretically demonstrated in the 1970s that radiative heat transfer between planar surfaces separated by a vacuum gap smaller than the thermal wavelength exceeds the blackbody limit due to tunneling of evanescent modes. This finding has led to the conceptualization of systems capitalizing on evanescent modes such as thermophotovoltaic power generators [3] and thermal rectifiers [4]. The development of these potential applications is however currently limited by the lack of devices capable of

exchanging heat by radiation between two macroscale planar surfaces separated by a nanosize vacuum gap. Here, using a custom-fabricated device in which the gap separating two 5×5 mm^2 intrinsic Si planar surfaces is modulated in the range of 3500 nm to 150 nm via a compliant membrane and mechanical actuation, we measure radiative heat transfer for large temperature differences ($\Delta T \sim 120$ K) in various regimes, including those dominated by either propagating or evanescent modes. Excellent agreement between fluctuational electrodynamics predictions and experimental data is observed, and a substantial radiative transfer enhancement over the blackbody limit by a factor of 8.4 is reported for a 150-nm-thick separation gap. Our near-field radiative heat transfer device paves the way for the establishment of novel evanescent wave-based engineering systems.

5.1.2 Introduction

Radiation heat transfer exceeding the blackbody limit at nanosize separation gaps has been experimentally confirmed in the scanning probe-surface [5-7], scanning probe-film [8], microsphere-surface [9-12], microsphere-film [13] and microsphere-nanostructured surface [14] configurations. Although the accuracy of fluctuational electrodynamics at sub-10 nm gaps has been questioned in the experiments of Kittel et al. [6], the validity of this framework has been confirmed both experimentally [7] and theoretically [15] down to separation gaps of 2 nm and 1 nm, respectively. Additional works involving micro/nanostructures have also experimentally demonstrated the enhancement of thermal radiation in the near field [16-20]. The micro/nanosize surfaces involved in the aforementioned experiments, however, limit the amount of radiation that can be exchanged, such that these configurations cannot be readily applied to engineering

systems such as thermophotovoltaic power generators. While the development of evanescent wave-based devices typically requires macroscale surfaces separated by a nanosize vacuum gap, experimental research on near-field radiative heat transfer between macroscale surfaces has mainly focused on relatively large, microsize separation gaps at cryogenic [21,22] and room [23-26] temperatures. Recently, Ito et al. [27] measured radiative heat transfer between millimeter-size fused quartz surfaces separated by pillars, also made of fused quartz, at a separation gap of 500 nm. The results were twice that of fluctuational electrodynamics predictions due to excessive heat conduction through the pillars, which prevent the application of this configuration to engineering systems. Lim et al. [28] measured a radiative heat transfer enhancement of 2.91 relative to the blackbody limit between two microstrips of doped Si separated by a 400-nm-thick gap. Yet, significant heat transfer and radiation enhancement necessitate larger surfaces and a smaller separation gap, respectively.

Here, we measure radiative heat transfer via a custom-fabricated MEMS-based device consisting of two planar 5×5 mm^2 intrinsic Si surfaces separated by a gap that can be modulated from 3500 nm down to 150 nm. This device enables probing radiative heat transfer between macroscale surfaces for large temperature differences ($\Delta T \sim 120$ K) in multiple regimes, including those dominated by either propagating or evanescent modes. The device, shown in Figure 5.1, was manufactured using standard microfabrication techniques, as detailed in Section 5.3.1, and consists of two 2.2×2.2 cm^2 Si substrates separated by four rigid, 3.5-μm-tall SU-8 posts with a diameter of 250 μm. The bottom substrate was fabricated from a 525-μm-thick intrinsic Si wafer while the top substrate was manufactured from a 521-μm-thick Si-on-insulator (SOI) wafer

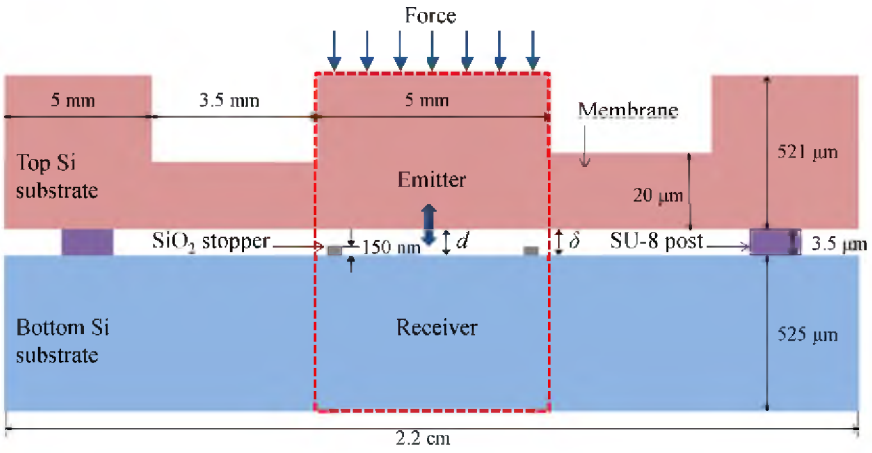

Figure 5.1 Schematic of the device in the open position, where the emitter-receiver portion is identified by a red dashed box. It consists of two Si substrates separated by 3.5-μm-tall SU-8 posts. The separation gap between the emitter and the receiver, d, can be modulated by applying a force causing the membrane to flex. The minimum separation gap d is 150 nm and corresponds to the height of the SiO_2 stoppers. The gap d is uniform under an applied force, while the separation gap outside the emitter-receiver region, δ, is non-uniform when a force is applied to the device. The 1-μm-thick buried SiO_2 layer in the top Si substrate is not shown.

with a 1-μm-thick buried silicon dioxide (SiO_2) layer. The surface roughness of the Si substrates was less than 1.2 nm as measured with a Zygo NewView optical profilometer. A 501-μm-deep, 3.5-mm-wide trench was etched on the backside of the top Si substrate using deep reactive ion etching and a buffered oxide etch solution. This resulted in a 20-μm-thick compliant Si membrane allowing the 5×5 mm^2 emitter to move relative to the receiver (the emitter-receiver portion of the device is identified by the dashed box in Figure 5.1 under an applied force. To avoid contact between the emitter and the receiver, four SiO_2 stoppers with a diameter of 5 μm and height of 150 nm were fabricated on the lower Si substrate, thus fixing the minimum separation gap d to 150 nm. The two Si substrates were precisely aligned and bonded in an EVG 520 IS wafer bonder. Testing of the device was conducted in a vacuum chamber ($P \approx 10^{-4}$ Pa) located in a class 1000 clean room tent.

5.1.3 Results

5.1.3.1 Experimental Procedure

Heat transfer measurements were performed using the configuration shown in Figures 5.2 and 5.3. The temperature difference was maintained via thermoelectric (TE) modules (Custom Thermoelectric, 00701-9B30-22RU4) acting as a heat pump and cooler on the emitter and receiver sides, respectively. The TE heat pump was mounted on a 500-μm-thick copper (Cu) heat spreader located on the 5×5 mm^2 Si emitter. The temperature of the outer surface of the emitter $T_{e,o}$ was measured via a thermistor (Selco, LSMC700A010KD002) embedded in the Cu heat spreader. The outer surface of the receiver was maintained at a temperature $T_{r,o}$ of 300 K, monitored via a thermistor, by the TE cooler. The receiver and TE cooler were separated by a 500-μm-thick Cu heat spreader. The entire device was placed on a Cu heat sink mounted to the base of the vacuum chamber (see Figure 5.4) and all contact resistances were minimized using thermal grease (Arctic Silver Ceramique 2). Heat was supplied to the device at a rate Q, which is the sum of the heat rate into (Q_{in}) and supplied by (P_{HP}) the TE heat pump. Since the device is in a vacuum, Q_{in} is solely due to thermal emission by the stainless steel walls and aluminum door of the vacuum chamber near ambient temperature, and is thus much smaller than P_{HP}, such that $Q \approx P_{HP}$. The heat supplied by the TE heat pump Q, partially spreading outside the emitter-receiver portion of the device, is divided into two contributions, namely radiation heat transfer at a separation gap d between the emitter and receiver $Q_{e\text{-}r}$, and the background heat transfer Q_{back}. The background heat rate Q_{back} includes radiation outside the emitter-receiver portion of the device at a separation gap δ, conduction through the SU-8 posts and conduction through the SiO_2

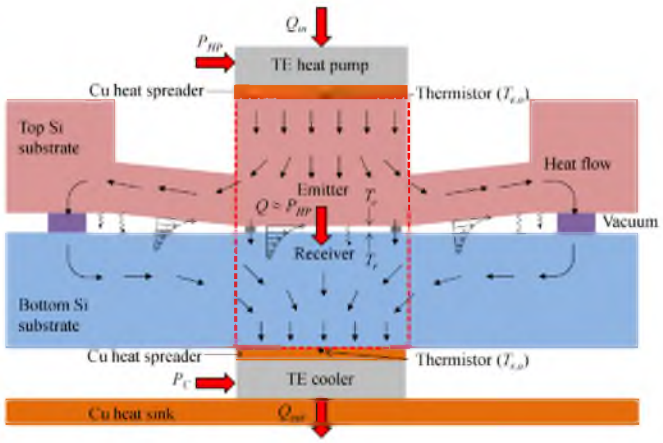

Figure 5.2 Heat flow through the device in the closed position. The temperature difference between the emitter and receiver is maintained by a TE heat pump and a TE cooler. The power supplied to the heat pump, P_{HP}, is approximately equal to the heat rate through the device, Q. Heat transfer between the top and bottom Si substrates occurs via radiation within and outside the emitter-receiver region and by conduction through the SU-8 posts and SiO_2 stoppers when the device is in the closed position. The temperatures $T_{e,o}$ and $T_{r,o}$ are measured by thermistors and are approximately equal to T_e and T_r, respectively.

stoppers when the device is in the closed position. Note that the thermal resistance associated with the separation gap (e.g., 462.4 KW^{-1} for d = 150 nm, $T_{e,o}$ = 420 K, $T_{r,o}$ = 300 K) is much larger than the thermal resistances of the emitter (0.192 KW^{-1}) and receiver (0.162 KW^{-1}), such that the measured temperatures are approximately equal to temperatures of the inner surfaces of the emitter (T_e) and receiver (T_r), adjacent to the vacuum gap. The experimental procedure was validated by measuring conduction through a 1.1-mm-thick layer of borosilicate glass. In addition, using a technique similar to that of Hu et al. [24], radiation transfer was measured between 5 × 5 mm^2 planar Si surfaces separated by vacuum gaps of 500 nm and 200 nm maintained by low thermal conductivity (0.18 $Wm^{-1}K^{-1}$) polystyrene spherical particles. These validation results are provided in Section 5.3.2.

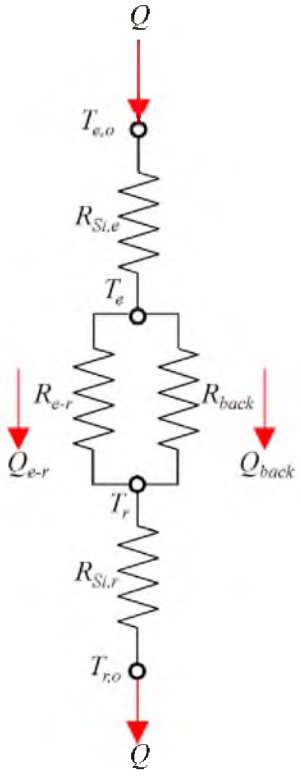

Figure 5.3 Equivalent thermal circuit of the device. $R_{Si,e}$ and $R_{Si,r}$ are the resistances of the Si emitter and receiver, $R_{e\text{-}r}$ is the resistance due to radiation between the emitter and receiver, R_{back} is the resistance due to background heat transfer that includes radiation outside the emitter-receiver region as well as conduction through the SU-8 posts and SiO_2 stoppers. The heat rate flowing through the device, Q, is the sum of heat rates due to radiation between the emitter and receiver, $Q_{e\text{-}r}$, and background heat transfer, Q_{back}.

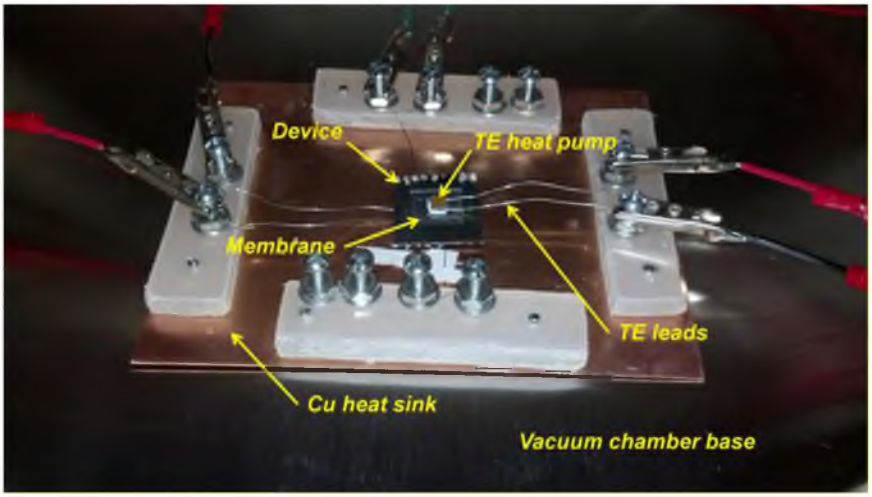

Figure 5.4 Photograph of the near-field radiative heat transfer device in the vacuum chamber.

5.1.3.2 Heat Rate Measurements

The heat rate supplied by the TE heat pump was compared against numerical predictions based on the measured temperatures. Unprocessed experimental heat rates Q that include radiation heat transfer between the emitter and receiver $Q_{e\text{-}r}$ as well as the background heat transfer Q_{back} are shown in Figure 5.5 for temperature differences ΔT (= $T_e - T_r$) up to 120 K. The separation gap d between the emitter and receiver was modulated by using calibrated masses ranging from 0.9 g to 5 g, as detailed in Section 5.3.3. The numerical predictions were obtained via a coupled fluctuational electrodynamics-COMSOL Multiphysics comprehensive heat transfer model of the device taking into account radiation between the emitter and receiver, heat transfer by radiation outside the emitter-receiver region and conduction through the SiO_2 stoppers and SU-8 posts. The details of the comprehensive model are provided in the 5.2.2. Figure 5.6 shows the temperature distribution in the device obtained from the model for a heat rate Q of 0.92 W and a separation gap d of 150 nm. The agreement between experimental data and numerical predictions when the device is in the open (d = 3500 ± 22 nm) and closed (d = 150 ± 5 nm) position is remarkable. The uncertainty associated with these gap sizes, identified as colored bands in Figure 5.5, was determined experimentally by measuring the variation of the height of the SiO_2 and SU-8 layers used to create the stoppers and the posts, respectively. Using nominal gap values of 3500 nm and 150 nm in the numerical simulations, a maximum relative difference between experiments and predictions of 9.1% is obtained for a 3500-nm-thick gap and ΔT = 15.5 K, while a minimum relative difference of less than 0.1% is achieved for a 150-nm-thick gap and ΔT = 84.2 K. In addition, for all cases presented in Figure 5.5, radiation largely dominates

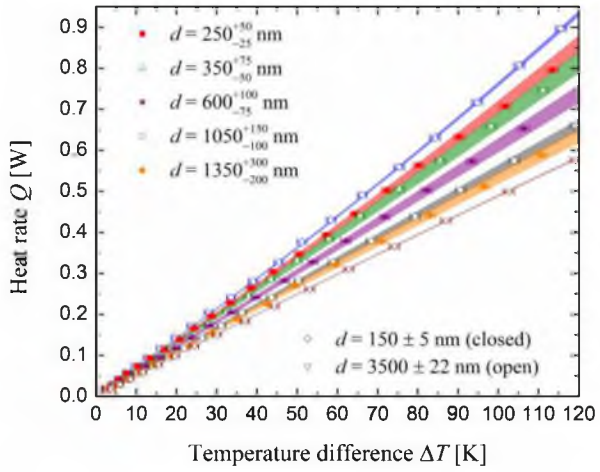

Figure 5.5 Heat rate, Q, as a function of the temperature difference between the emitter and receiver, ΔT, for various separation gaps, d. In all cases, the temperature of the receiver, T_r, is fixed at 300 K. The symbols show unprocessed experimental data while the colored bands are numerical simulations obtained from the coupled fluctuational electrodynamics-COMSOL Multiphysics comprehensive model described in the Section 5.2.2. The gap sizes d in the open and closed position are known, with some small uncertainty, from the manufacturing of the device and the associated measured heat rate are in good agreement with numerical predictions. It was not possible to measure directly the intermediate gap sizes, such that they were estimated from the comprehensive heat transfer model.

heat transfer through the device. According to the model, the portion of the heat rate due to conduction reaches a maximum of 11.7% when the gap size is 3500 nm and the temperature difference is 3.8 K. For the case when the device is in the closed position (d = 150 nm) and the temperature difference is 115.6 K, the portion of the total heat rate due to conduction is at a minimum of 6.6%. As explained in Section 5.3.3, it was not possible to determine exactly the intermediate gap sizes between the open and closed positions. As the force applied on the device was increased, it was observed that the heat rate Q increased, due to a larger proportion of evanescent modes contributing to heat transfer, until the device was in the closed position. Intermediate gap sizes, shown in Figure 5.5, were estimated using the comprehensive model, the measured heat rates and emitter temperatures (see Section 5.2.3).

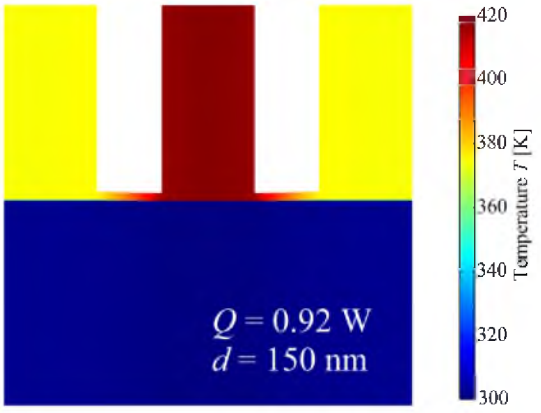

Figure 5.6 Simulated temperature distribution in the device via the comprehensive model for an input heat rate Q of 0.92 W, a separation gap d of 150 nm, and a fixed receiver temperature T_r of 300 K resulting in an emitter temperature of 420 K. Heat spreading outside the emitter portion of the device results in background heat transfer Q_{back}.

5.1.4 Discussion

The radiative heat flux between the 5 × 5 mm^2 emitter and receiver without the background heat rate is shown in Figure 5.7 as a function of the temperature difference. The agreement between experimental data and fluctuational electrodynamics predictions in the open and closed positions is excellent. A maximum radiation transfer enhancement over the blackbody limit by a factor of 8.4 was measured for a gap size of 150 nm and a temperature difference of 115.6 K. This constitutes the largest value recorded between two macroscale plane surfaces at non-cryogenic temperatures. The mechanism responsible for this enhancement can be understood by inspecting the dispersion relations shown in Figure 5.8, where the heat flux is plotted as a function of the angular frequency ω and parallel wavevector k_ρ for gap sizes of 3500 nm, 1000 nm, 500 nm and 150 nm, and a temperature difference of 120 K. Modes that are propagating in both Si and vacuum are contained within the region $k_\rho < k_0$ (= ω/c_0), where k_0 is the magnitude of the wavevector in vacuum. Planck's theory of heat radiation solely accounts for these modes. Frustrated modes, propagating in Si and evanescent in vacuum, are characterized by

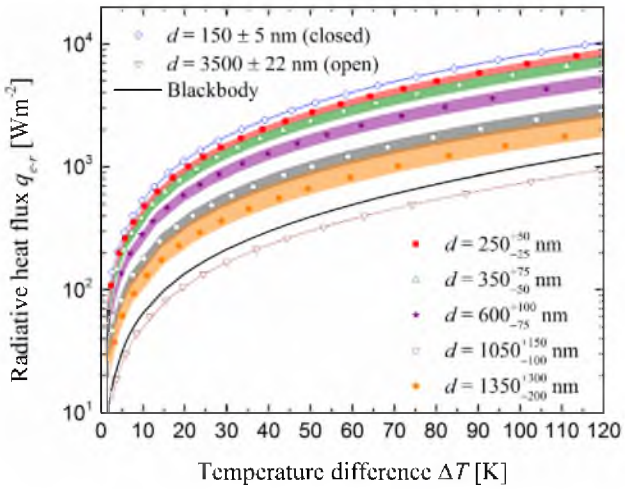

Figure 5.7 Radiative heat flux, qe-r, as a function of temperature difference, ΔT. The symbols show the experimental heat flux between the 5 × 5 mm2 emitter and receiver, where the background heat transfer has been subtracted. The colored bands are fluctuational electrodynamics predictions. In the closed position (d = 150 nm), the experimental radiative heat flux exceeds the blackbody predictions by a factor of 8.4. In the open position (d = 3500 nm), the measured radiative heat flux is below the blackbody predictions due to a modest contribution from evanescent modes.

parallel wavevectors $k_0 < k_\rho < \mathrm{Re}(n)k_0$, where n is the refractive index of Si. Surface modes are evanescent in both Si and vacuum and are described by $k_\rho > \mathrm{Re}(n)k_0$. The dispersion relations show clearly that the enhancement of radiative heat transfer is solely due to the additional contribution of frustrated modes in the near field, as intrinsic Si does not support surface modes such as surface phonon-polaritons or surface plasmon-polaritons. Here, with a single device, we measured radiative heat transfer in various regimes, including those dominated by either propagating or evanescent modes. Indeed, although heat transfer via frustrated modes occurs at a gap of 3500 nm, their contribution is insufficient to exceed the blackbody predictions (approximately 68% of the heat flux is due to propagating modes). Conversely, radiation heat transfer is largely dominated by frustrated modes for a 150-nm-thick gap and accounts for approximately 88% of the heat flux between the emitter and the receiver.

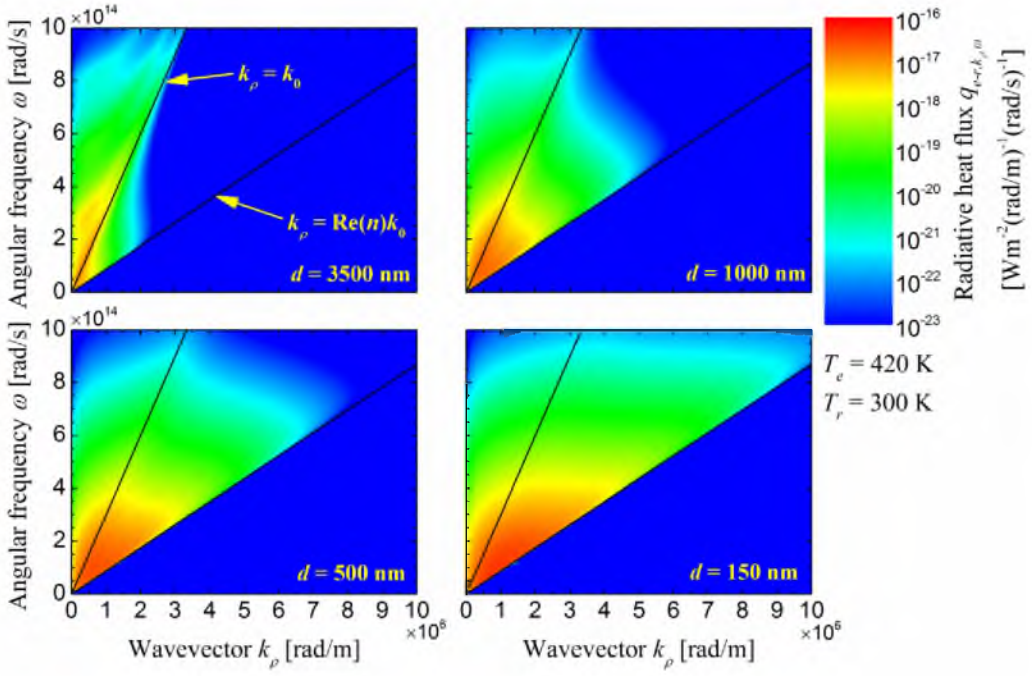

Figure 5.8 Calculated dispersion relations showing the radiative heat flux per unit parallel wavevector k_ρ and angular frequency ω for gaps of 3500 nm, 1000 nm, 500 nm and 150 nm, and emitter and receiver temperatures of 420 K and 300 K, respectively. The region where k_ρ is smaller than k_0 corresponds to modes that are propagating in the vacuum gap, while the zone where $k_0 < k_\rho < \mathrm{Re}(n)k_0$ describes frustrated modes that are propagating in Si but evanescent in the vacuum gap. Radiation enhancement in the near field for the case of intrinsic Si is solely due to these frustrated modes that have an increasing contribution to heat transfer as the separation gap d decreases.

The experimental results presented here show that it is possible to enhance radiation heat transfer by approximately an order of magnitude relative to the blackbody limit between two macroscale surfaces separated by a nanosize vacuum gap due to the additional contribution of frustrated modes. In terms of application, it has been recently suggested that frustrated modes may be more beneficial to the performance of evanescent wave-mediated thermophotovoltaic power generators than surface modes [29], thus showing the importance of materials like intrinsic Si. Our near-field radiative heat transfer device paves the way to the development of engineering systems capable of converting evanescent modes into electrical power.

5.2 Methods

5.2.1 Experimental Uncertainty Analysis

The uncertainty associated with the experimental data is due to the temperature and heat rate measurements. For the temperature, the uncertainty stems from the ohmmeter (BK Precision, 889B) used to measure the resistance of the thermistors as well as the thermistors themselves. The error in the resistance measurement is given by the manufacturer specifications as ± (0.2% + 0.1 Ω) within the range from 100 Ω to 1000 Ω, and ± (0.1% + 1.0 Ω) for the range of 1 kΩ to 10 kΩ. The uncertainty introduced by the thermistors is a function of temperature and the thermistors' change of resistance with temperature. A resistance reading of 9225 Ω corresponds to a temperature of 300 ± 0.46 K while a resistance reading of 185.8 Ω corresponds to a temperature of 420 ± 0.85 K. Combining the uncertainties introduced by the ohmmeter and the thermistors results in an overall uncertainty of ± 0.48 K at 300 K and ± 0.89 K at 420 K.

The uncertainty associated with the heat rate is introduced by the power supply (BK Precision, 9121A) connected to the TE heat pump. The uncertainty in the supplied current is ± (0.05% + 2 mA) and the uncertainty in the supplied voltage is ± (0.02% + 3 mV). Additionally, the resistance associated with the wires needs to be accounted for since it induces a small amount of power dissipation. A four-wire sensing technique was employed to account for the resistance of the wires leading up to the device. The resistance associated with the TE leads (see Figure 5.4) was measured to be 0.08 Ω ± 0.9 mΩ. For example, when 1.2 A ± 2.6 mA and 0.84 V ± 3.2 mV is provided by the power supply (1.01 W ± 6.0 mW), the power dissipated in the TE leads is 115.2 ± 1.8 mW. The power supplied to the TE heat pump, which is equivalent to the total heat rate, is then

determined to be 894.8 ± 7.8 mW. These uncertainties are plotted as error bars in Figure 5.5.

5.2.2 Computational Model

Near-field radiative heat transfer was modeled using fluctuational electrodynamics [1]. The net radiative heat flux due to propagating and evanescent waves was calculated as follows [2]:

$$q^{prop} = \frac{1}{4\pi^2}\int_0^{\infty} d\omega\left[\Theta(\omega,T_1)-\Theta(\omega,T_2)\right]\int_0^{k_0} dk_\rho k_\rho \left[\frac{\left(1-\left|r_{01}^{TE}\right|^2\right)\left(1-\left|r_{02}^{TE}\right|^2\right)}{\left|1-r_{01}^{TE}r_{02}^{TE}e^{2i\,\mathrm{Re}(k_{z0})\delta}\right|^2}+\frac{\left(1-\left|r_{01}^{TM}\right|^2\right)\left(1-\left|r_{02}^{TM}\right|^2\right)}{\left|1-r_{01}^{TM}r_{02}^{TM}e^{2i\,\mathrm{Re}(k_{z0})\delta}\right|^2}\right] \quad (5.1)$$

$$q^{evan} = \frac{1}{\pi^2}\int_0^{\infty} d\omega\left[\Theta(\omega,T_1)-\Theta(\omega,T_2)\right]\int_{k_0}^{\infty} dk_\rho k_\rho e^{-2\,\mathrm{Im}(k_{z0})\delta}\left[\frac{\mathrm{Im}\left(r_{01}^{TE}\right)\mathrm{Im}\left(r_{02}^{TE}\right)}{\left|1-r_{01}^{TE}r_{02}^{TE}e^{-2\,\mathrm{Im}(k_{z0})\delta}\right|^2}+\frac{\mathrm{Im}\left(r_{01}^{TM}\right)\mathrm{Im}\left(r_{02}^{TM}\right)}{\left|1-r_{01}^{TM}r_{02}^{TM}e^{-2\,\mathrm{Im}(k_{z0})\delta}\right|^2}\right] \quad (5.2)$$

where the subscripts 0, 1 and 2, respectively refer to the vacuum, the top Si substrate and bottom Si substrate, $\Theta(\omega,T)$ is the mean energy of an electromagnetic state calculated as $\hbar\omega/[\exp(\hbar\omega/k_bT)-1]$, k_ρ and k_z are the components of the wavevector parallel and perpendicular to the surface of the layers, while r_{ij}^{TE} and r_{ij}^{TM} are the Fresnel reflection coefficients at the interface of media i and j in TE and TM polarizations. The dielectric function of intrinsic Si was assumed to be independent of temperature in the range of operation and was obtained by curve-fitting the experimental data from Ref. 30. Note that in the emitter-receiver portion of the device, the separation gap δ and temperatures T_1 and T_2 are equal to d, T_e and T_r, respectively. The net radiative heat flux used for producing the numerical results shown in Figures 5.5 and 5.7 was obtained by summing Equations

(5.1) and (5.2). The dispersion relations in Figure 5.8 were generated by solving Equations (5.1) and (5.2) per unit angular frequency ω and per unit parallel wavevector k_ρ.

The theoretical heat rate Q through the device, that includes radiation transfer between the emitter and the receiver $Q_{e\text{-}r}$ as well as the background heat transfer Q_{back}, was calculated using a coupled fluctuational electrodynamics-COMSOL Multiphysics comprehensive model. Near-field radiative heat transfer was included in COMSOL by defining a fictional material, in place of the vacuum gap, characterized by a local, temperature-dependent effective thermal conductivity. In the emitter-receiver portion of the device, the effective conductivity was calculated using Equations (5.1) and (5.2) at a uniform separation gap d. The effective conductivity outside the emitter-receiver region was derived using the Derjaguin approximation [11] to account for the variations of the separation distance δ, assumed to be linear, when the device was not in the open position. Heat conduction through the SU-8 posts and SiO_2 stoppers was calculated using temperature-independent thermal conductivities of 0.2 $Wm^{-1}K^{-1}$ and 1.3 $Wm^{-1}K^{-1}$, respectively, while the temperature-dependent thermal conductivity provided in Ref. 31 was used for intrinsic Si. A typical value for contact resistance of 2.5×10^{-5} Km^2W^{-1} was imposed between the Si and SiO_2 stoppers as well as between the Si and SU-8 posts. Heat transfer simulations in the device were initiated by imposing the heat rate Q supplied by the TE heat pump, while the TE cooler was modeled as a constant temperature boundary condition (300 K) at the bottom face of the receiver. For a given heat input Q and gap thickness d between the emitter and receiver, the temperature distribution in the device was determined using an iterative method where the effective thermal conductivity of the

vacuum gap and the thermal conductivity of Si were calculated at the updated temperature. Iterations were repeated until a maximum absolute temperature difference less than 0.001 K was achieved across the device. For a specific separation gap d, these simulations were repeated for a series of heat inputs Q ranging from 0 to 1.4 W in increments of 0.04 W. This allowed determining a theoretical heat rate Q as a function of the temperature difference ΔT between the emitter and receiver for a specific separation gap d. For instance, Figure 5.6 shows the temperature distribution in the device for a heat input Q of 0.92 W and a separation gap d of 150 nm. For these conditions, the emitter reaches a uniform temperature of 420 K, but heat is also dissipated outside the emitter region in the top Si substrate. It can also be seen that the bottom Si substrate has a nearly uniform temperature of 300 K.

Validation of the coupled fluctuational electrodynamics-COMSOL Multiphysics model was performed by comparing numerical predictions against unprocessed experimental data measured when the device was in the open (d = 3500 ± 22 nm) and closed (d = 150 ± 5 nm) positions. The uncertainty associated with these two gap sizes was used to calculate a theoretical band of heat rate Q as a function of the temperature difference ΔT. These bands, however, are fairly small due to the small uncertainty associated with these gap sizes, and are thus hardly visible in Figure 5.5.

5.2.3 Estimation of Intermediate Separation Gap Sizes between the Emitter and Receiver

There was no direct method for measuring the separation gap between the emitter and receiver, except when the device was in the open and closed positions. Since the coupled fluctuational electrodynamics-COMSOL Multiphysics model was in excellent agreement with the measured heat rate as a function of the temperature difference in both

the open and closed positions (see Figure 5.5), intermediate separation gap sizes were estimated using the aforementioned model. Specifically, a nominal gap size d was determined by best fitting the experimental data with numerical predictions. The uncertainty associated with the estimated gaps, shown in colored bands in Figures 5.5 and 5.7, was derived using the uncertainty associated with the measured temperatures and heat rates.

Even if intermediate gap sizes were not determined from another independent measurement, the experimental results show clearly that heat transfer increases as the separation gap decreases due to an increasing contribution of evanescent modes. Heat transfer reaches saturation when the emitter comes into contact with the SiO_2 stoppers. These observations are consistent with fluctuational electrodynamics predictions.

5.3 Supplementary Information

5.3.1 Device Fabrication

5.3.1.1 Fabrication of the Bottom Si Substrate

The main steps required in fabricating the bottom Si substrate are shown in Figure 5.9. Starting with a 525-μm-thick, 10-cm-diameter intrinsic Si wafer, a 150-nm-thick layer of SiO_2 was grown using thermal oxidation. Most of the SiO_2 layer was etched away using UV lithography and a buffered oxide etch (BOE) solution consisting of 25% HF:40% NH_4F leaving a set of four 5-μm-diameter stoppers per device. The purpose of these stoppers was to prevent the emitter from making contact with the receiver when the device was in the closed position. Next, a 3.5-μm-thick layer of SU-8 3005 negative photoresist was spun onto the wafer. A spin speed of 4500 rpm lasting 30" was required to achieve the desired thickness. Using UV lithography, 250-μm-diameter areas

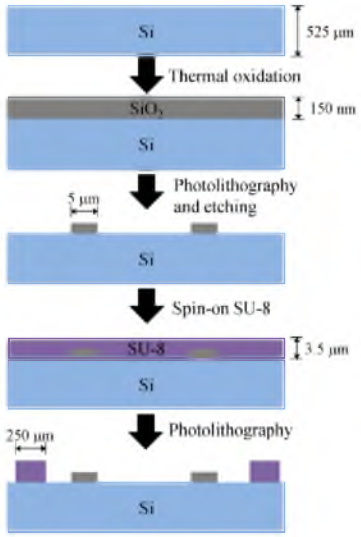

Figure 5.9 Main fabrication steps for the bottom Si substrate.

were exposed and developed in order to create the posts (four per device) separating the top and bottom Si substrates. Six bottom Si substrates were created by dicing the wafer into 2.2 × 2.2 cm^2 sections.

5.3.1.2 Fabrication of the Top Si Substrate

The main steps required in fabricating the top Si substrate are shown in Figure 5.10. Fabrication was performed on a 521-μm-thick, 10-cm-diameter Si-on-insulator (SOI) wafer. The SOI wafer consisted of a 20-μm-thick intrinsic Si device layer, a 1-μm-thick buried SiO_2 insulator layer and a 500-μm-thick intrinsic Si handle layer. The first step in fabricating the 3.5-mm-wide, 20-μm-thick membrane was to spin-on and pattern a layer of AZ9260 photoresist using UV lithography. The patterned photoresist layer acted as a mask for the deep reactive ion etching (DRIE) process. The buried SiO_2 insulator layer acted as an etch-stop to prevent over-etching into the Si device layer. The insulator layer was then etched away using a BOE solution leaving only the 20-μm-thick membrane.

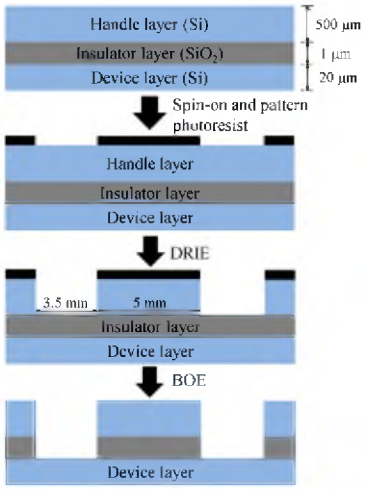

Figure 5.10 Main fabrication steps for the top Si substrate using an SOI wafer.

When spinning-on the AZ9260 photoresist, an additional drop of photoresist dripped onto the wafer near the end of the spin cycle. The extra drop left a thicker area of photoresist that was not uniformly spread on the wafer. This was not visually apparent and went unnoticed until after the DRIE etch process had begun. This resulted in portions of the membrane being slightly thicker than 20 μm such that the membrane was stiffer than expected. This effect is detailed further in Section 5.3.3.

5.3.1.3 Bonding of the Top and Bottom Si Substrates

The top and bottom Si substrates were bonded following the procedure described in Ref. 32 using an EVG 520 IS wafer bonder. The two substrates were precisely aligned using a custom-made alignment fixture. The fixture consisted of glass microscope slides bonded to a Si wafer. The fixture, along with the device, was placed inside the wafer bonder and subjected to a compressive force of 700 N at a temperature of 210°C for 60'. This caused the SU-8 posts, located on the bottom Si substrate, to bond to the top Si substrate. Figure 5.11 shows a photograph of the device and alignment fixture inside the wafer bonder.

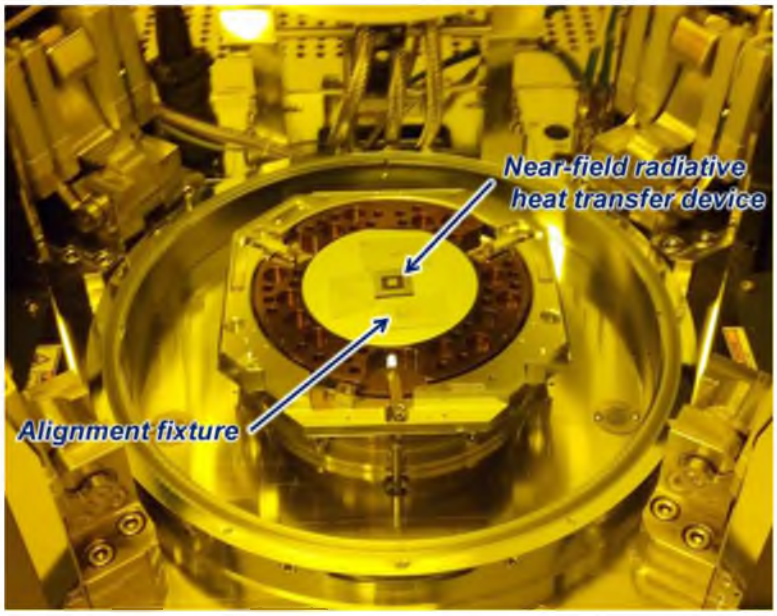

Figure 5.11 Interior of the EVG 520 IS wafer bonder. A custom-fabricated fixture was employed to ensure proper alignment of the top and bottom Si substrates.

5.3.2 Calibration of the experimental setup

5.3.2.1 Conduction Heat Transfer through Borosilicate Glass

The measurement method was first calibrated by measuring the thermal conductivity κ of a 1.1-mm-thick layer of borosilicate glass. Figures 5.12 and 5.13 show a schematic of the experimental setup and the associated results. The near-field radiative heat transfer device was replaced with a 5×5 mm^2 layer of borosilicate glass, and its thermal conductivity κ was retrieved by measuring the heat rate Q as a function of the temperature difference ΔT. Note that the cold side of the borosilicate layer, measured by a thermistor, was maintained at a constant temperature T_2 of 300 K in all experiments. Using Fourier's law and assuming one-dimensional conduction, a thermal conductivity κ of 1.0 Wm^{-1}K^{-1} was experimentally determined. This value is in good agreement with published data for borosilicate glass [33].

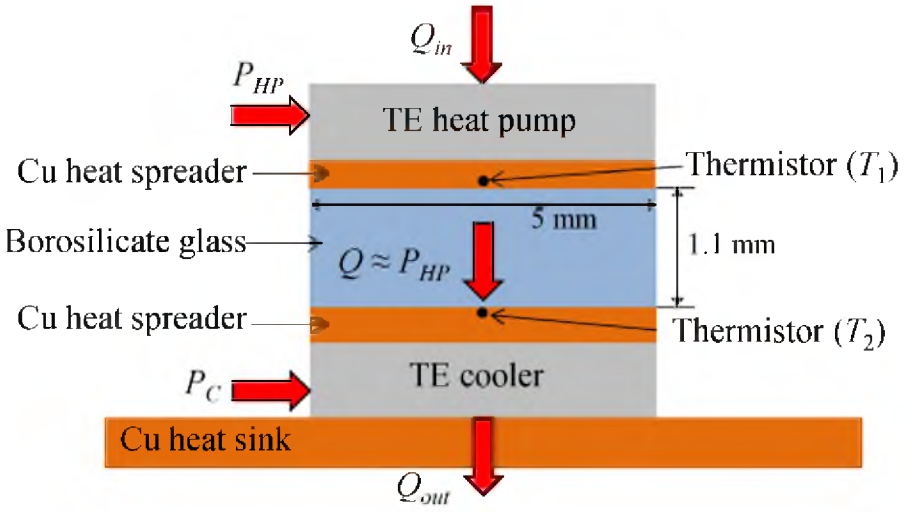

Figure 5.12 Schematic of the experimental setup used to calibrate the measurement system for the case of conduction. It consists of a 1.1-mm-thick layer of borosilicate glass sandwiched between two Cu heat spreaders. The temperature difference is maintained by a TE heat pump and a TE cooler. The power supplied to the TE heat pump, P_{HP}, is approximately equal to the heat rate through the glass, Q. The temperatures on either side of the glass layer, T_1 and T_2, are measured using thermistors embedded in the Cu heat spreaders.

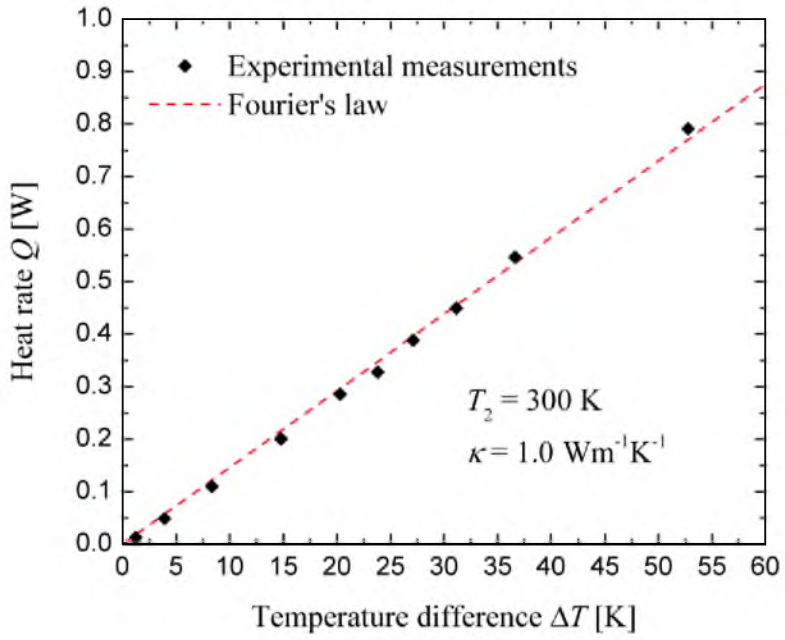

Figure 5.13 Heat rate, Q, as a function of temperature difference ΔT. The symbols indicate unprocessed experimental results while the dashed line correspond to Fourier's law using a thermal conductivity κ = 1.0 Wm^{-1}K^{-1} for borosilicate glass.

5.3.2.2 Radiation Heat Transfer between Si Surfaces separated by Nanosize Polystyrene Particles

In order to calibrate the measurement method for the case of radiation, the near-field radiative heat transfer device was replaced by two 5 × 5 mm^2, 525-μm-thick layers of intrinsic Si separated by vacuum gaps of 500 nm and 200 nm maintained by polystyrene spherical particles. This technique was used by Hu et al. [24] for measuring near-field radiative heat transfer between SiO_2 plates separated by a 1.6-μm-thick vacuum gap, since the polystyrene particles have a low thermal conductivity κ_p of 0.18 $Wm^{-1}K^{-1}$ and are essentially transparent in the infrared spectral band. A schematic of the setup and associated results are provided in Figures 5.14 and 5.15.

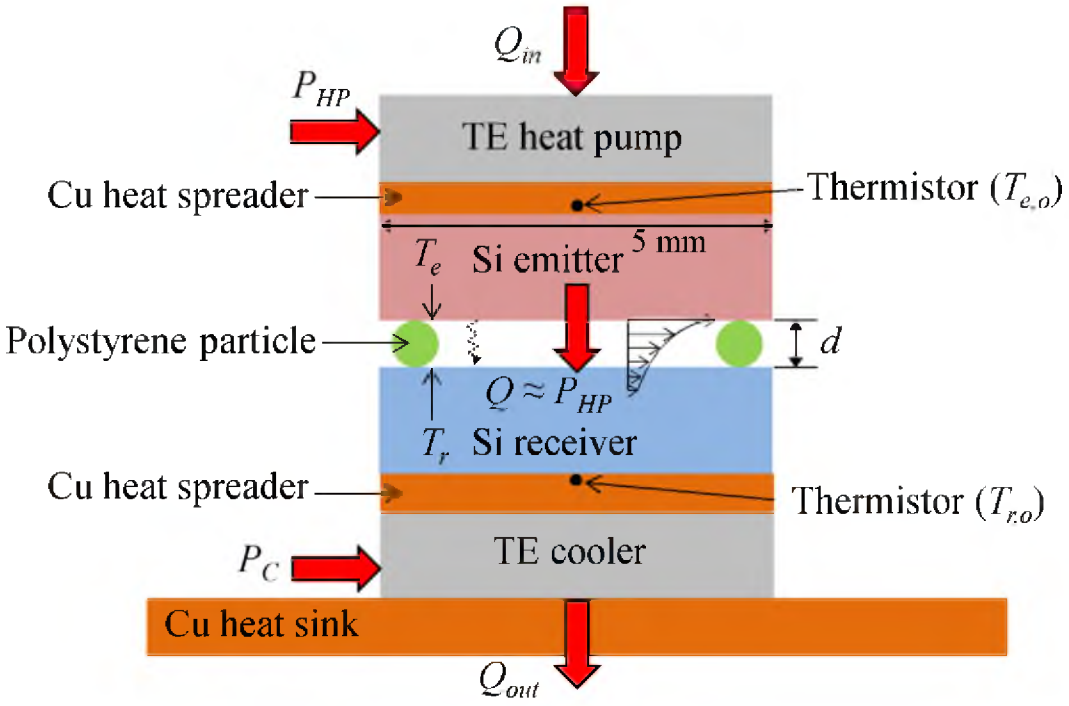

Figure 5.14 Schematic of the experimental setup used to calibrate the measurement system for the case of near-field radiation. It consists of two Si substrates separated by vacuum gap sizes of 500 nm and 200 nm using polystyrene spherical particles. The temperature difference between the emitter and receiver is maintained by a TE heat pump and a TE cooler. The power supplied to the TE heat pump, P_{HP}, is approximately equal to the heat rate through the glass, Q. The temperatures $T_{e,o}$ and $T_{r,o}$ are measured by thermistors and are approximately equal to T_e and T_r, respectively.

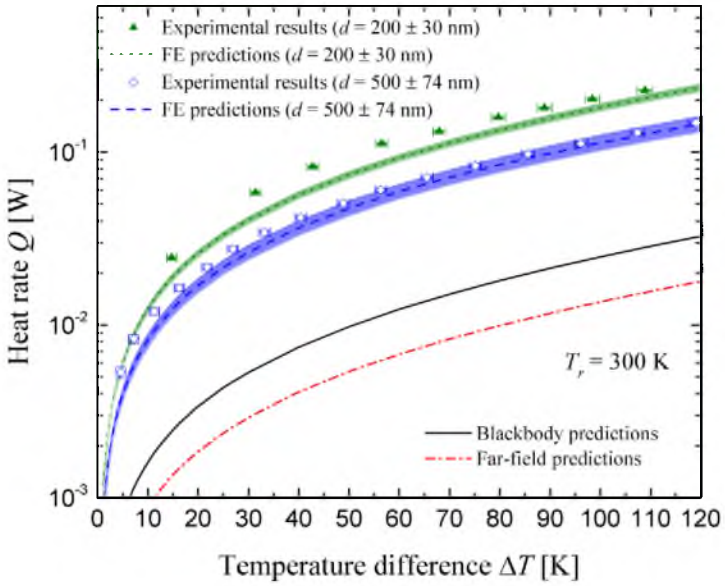

Figure 5.15 Heat rate, Q, as a function of temperature difference between the emitter and receiver, ΔT. The symbols show unprocessed experimental measurements, while the colored bands are numerical simulations obtained from fluctuational electrodynamics. Experimental results at a gap size of 500 nm exceed blackbody predictions by a factor of 4.6 at a temperature difference of 119.0 K. At a gap size of 200 nm, blackbody predictions are exceeded by a factor of 8.1 at a temperature difference of 108.9 K.

The Si emitter and receiver were cleaned in a UV/ozone chamber and were then rinsed in acetone, isopropanol and deionized water prior to depositing the polystyrene particles. The 500-nm-diameter particles were in a suspension of deionized water at a concentration of 1.15×10^{11} particles/mL. The suspension was sonicated with an Elmasonic Bath Sonicator to ensure a uniform distribution of particles. Since the particles were in a fairly high initial concentration, it was necessary to dilute them to ensure that only a monolayer of particles was deposited on the Si surface and to minimize conduction heat transfer between the emitter and receiver. The dilution was performed in two steps. First, 0.05 mL of the particle suspension was diluted with 100 mL of deionized water; second, 1 mL of the intermediate suspension from the first step was diluted with 115 mL of deionized water. The resulting concentration was 5×10^{6} particles/mL. Using a syringe,

0.02 mL of the suspension was deposited on the Si receiver leaving approximately 10^4 polystyrene particles on the surface. The Si receiver was then dried on a hotplate before being aligned with the Si emitter and placed in the vacuum chamber. Preparation of the samples separated by 200-nm-diameter polystyrene particles was accomplished in a similar fashion. These particles were initially suspended in deionized water at a concentration of 1.8×10^{12} particles/mL and were diluted to a concentration of 7.8×10^6 particles/mL in two steps using sonication. A syringe was used to deposit 0.02 mL of the suspension on the surface of the Si receiver resulting in approximately 1.6×10^5 particles. According to the manufacturer specifications, the standard deviation in particle sizes was ±74 nm and ±30 nm for the 500 nm and 200 nm particles, respectively. This standard deviation was taken into account in the fluctuational electrodynamics simulations and is shown as colored bands in Figure 5.15.

The heat flow through the sample Q supplied by the TE heat pump is split into two contributions, namely the heat rate by radiation between the emitter and receiver $Q_{e\text{-}r}$, and the background heat rate Q_{back} (see Figure 5.2). Here, the background heat rate is solely due to conduction through the polystyrene particles. This background heat rate was determined by estimating the contact area between the particles and the Si surfaces via a Hertz model. Taking into account the force exerted by the masses of the TE heat pump, Si emitter, thermistor and Cu heat spreader, the contact area A between the 500 nm polystyrene particles and Si was determined to be 2241 nm^2. The background heat rate was thus estimated using Fourier's law:

$$Q_{back} = N\frac{\square_p A}{D}(T_e \square T_r) \tag{5.3}$$

where N is the number of particles while D is the particle diameter which is the same as the gap size d separating the emitter and receiver. For a fixed receiver temperature of 300 K, the background heat rate was estimated to be 8.1×10^{-5} W and 9.7×10^{-4} W for temperature differences of 1 K and 120 K, respectively. Since the background heat transfer due to conduction through the polystyrene particles was always less than 1% of the heat rate by radiation, it was assumed that $Q \approx Q_{e\text{-}r}$. The contact area between the 200 nm particles and the Si surfaces was estimated to be 194 nm^2 using the same process as described earlier, thus resulting in background heat rates of 2.7×10^{-5} W to 3.4×10^{-3} W for temperature differences of 1 K and 120 K, respectively. Although this heat rate was slightly larger than for the case of 500-nm-diameter particles, it was always less than 1.7% of the heat rate by radiation such that $Q \approx Q_{e\text{-}r}$ was again assumed.

In general, there is a good agreement between experimental results and fluctuational electrodynamics predictions. For the case of 500 nm particles, the measured heat rate is 148.2×10^{-3} W at a temperature difference of 119.0 K. This differs from the predicted value of 143.5×10^{-3} W by 3.2%. At the lower end of the temperature difference, the experimentally measured heat rate is 5.3×10^{-3} W for a temperature difference of 4.6 K, which differs from the prediction of 3.7×10^{-3} W by 45.4%. However, the absolute value of the difference between the measured and experimental heat rates is 1.7×10^{-3} W, which is actually smaller than the difference at the high end of the temperature range of 4.6×10^{-3} W. For 200 nm particles, the measured heat rate is 227.7×10^{-3} W at a temperature difference of 108.9 K. This differs from the prediction of 205.1×10^{-3} W by 11.0%. At the lower end of the temperature difference, the experimentally measured heat rate is 24.5×10^{-3} W for a temperature difference of 14.7 K. This differs from the

prediction of 18.7×10^{-3} W by 31.3%. However, much like the case with 500 nm particles, the absolute value of the difference between the measured and experimental heat rates is 5.9×10^{-3} W which is less than the difference at the high end of the temperature range of 22.6×10^{-3} W. These discrepancies may be attributed to the difficulty in aligning the Si emitter and receiver. Unlike the near-field radiative heat transfer device, the Si emitter and receiver were aligned manually. Also, the imperfect dispersion of particles on the receiver, and possible perturbations of the thermal near field by the polystyrene particles could have contributed to the discrepancies.

5.3.3 Membrane Design

As shown in Figure 5.2, the device layer of an SOI wafer constitutes the membrane allowing the emitter to move relative to the receiver. The thickness of the device layer thus determined the thickness of the membrane. When designing the membrane, compliance and strength were considered. Since SOI wafers can be purchased with a variety of device layer thicknesses, a COMSOL model was created in order to determine an appropriate membrane thickness and width. Figures 5.16 and 5.17 show the results for a 3.5-mm-wide, 20-μm-thick membrane. According to the model, a force of 4 mN is required to displace the emitter by 3.39 μm. At this deflection, the peak stress is 6.13 MPa and occurs at the edges where the membrane adjoins the bulk Si. The yield strength of Si is 7 GPa [34]; therefore, the membrane can flex from a nominal gap size of 3500 nm down to 150 nm without failing.

The expected gap size under a 4 mN load is predicted to be 110 nm. Since the SiO_2 stoppers have a height of 150 nm, a 4 mN applied force, corresponding to an added mass of 0.41 g, is theoretically sufficient to bring the device to a closed position.

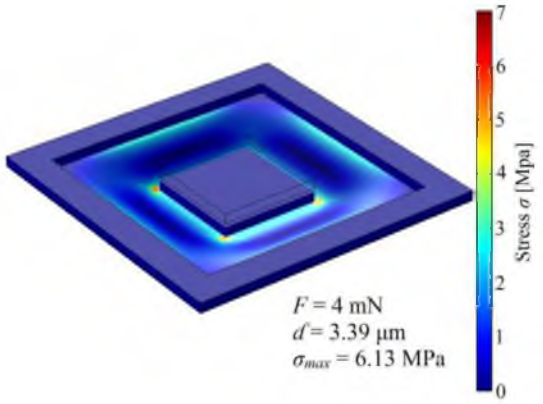

Figure 5.16 Stress distribution in the membrane when a force, F, of 4 mN is applied to the emitter. The maximum stress, σ_{max}, of 6.13 mPa occurring at the corners of the membrane is significantly smaller than the Si yield strength of 7 GPa. The model shows that the displacement, d, of the emitter relative to the receiver under an applied force of 4 mN is enough to bring the device in the closed position.

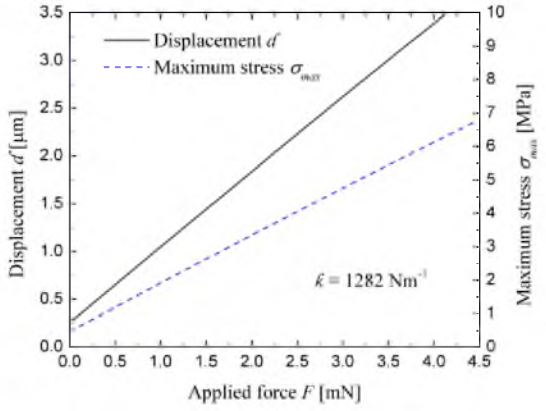

Figure 5.17 Numerical predictions of the emitter displacement, d, and membrane maximum stress, σ_{max}, as a function of the applied force, F, for the 20-µm-thick, 3.5-mm-wide membrane. The resulting spring coefficient, k, is predicted to be 1282 Nm^{-1}.

Additionally, according the model, the effective spring coefficient, k, of the membrane is 1282 Nm^{-1}. With a known spring coefficient, the gap size between the Si emitter and Si receiver can theoretically be determined based on the applied load.

Using the comprehensive heat transfer model to estimate the intermediate gaps between the closed and open position, it was found that a mass of 0.9 g results in a gap size of 1350^{+300}_{-200} nm, a mass of 1 g results in a gap size of 1050^{+150}_{-100} nm, a mass of 2 g

results in a gap size of 600^{+100}_{-75} nm, a mass of 3 g results in a gap size of 350^{+75}_{-50} nm, and a mass of 4 g results in a gap size of 250^{+50}_{-25} nm. In practice, the mass required to bring the device in closed position was 5 g, corresponding to a force of 49.1 mN. The device had a stiffer membrane than expected which also flexed in a non-linear fashion. As mass was added to the device and the gap size decreased, the spring coefficient increased causing the membrane to become stiffer as it flexed. The effective spring coefficient k of the experimental device with an applied load of 1 g was calculated as approximately 3518 Nm^{-1} while the spring coefficient was 14942 Nm^{-1} with an applied load of 5 g. This may be due to the issue encountered during fabrication that was discussed in Section 5.3.1.2. This resulted in the membrane being slightly thicker in certain areas causing it to be stiffer than designed.

5.4 References Cited

[1] S.M. Rytov, Y.A. Kravtsov, V.I. Tatarskii, *Principles of Statistical Radiophysics 3: Elements of Random Fields* (Springer, New York, 1989).

[2] D. Polder and M. Van Hove, Phys. Rev. B **4**, 3303, 1971.

[3] R.S. DiMatteo, P. Greiff, S.L. Finberg, K.A. Young-Waithe, H.K.H. Choy, M.M. Masaki and C.G. Fonstad, Appl. Phys. Lett. **79**, 1894 (2001).

[4] C.R. Otey, W.T. Lau and S. Fan, Phys. Rev. Lett. **104**, 154301 (2010).

[5] J.-B. Xu, K. Läuger, R. Möller, K. Dransfield and I.H. Wilson, J. Appl. Phys. **76**, 7209 (1994).

[6] A. Kittel, W. Müller-Hirsch, J. Parisi, S.-A. Biehs, D. Reddig and M. Holthaus, Phys. Rev. Lett. **95**, 224301 (2005).

[7] K. Kim, B. Song, V. Fernández-Hurtado, W. Lee, W. Jeong, L. Cui, D. Thomson, J. Feist, M.T.H. Reid, F.J. García-Vidal, J.C. Cuevas, E. Meyhofer and P. Reddy, Nature **528**, 387 (2015).

[8] L. Worbes, D. Hellmann and A. Kittel, Phys. Rev. Lett. **110**, 134302 (2013).

[9] A. Narayanaswamy, S. Shen and G. Chen, Phys. Rev. B **78**, 115303 (2008).

[10] S. Shen, A. Narayanaswamy and G. Chen, Nano Lett. **9**, 2909 (2009).

[11] E. Rousseau, A. Siria, G. Jourdan, S. Volz, F. Comin, J. Chevrier and J.-J. Greffet, Nature Photon. **3**, 514 (2009).

[12] S. Shen, A. Mavrokefalos, P. Sambegoro and G. Chen, Appl. Phys. Lett. **100**, 233114 (2012).

[13] B. Song, Y. Ganjeh, S. Sadat, D. Thomson, A. Fiorino, V. Fernández-Hurtado, J. Feist, F.J. García-Vidal, J.C. Cuevas, P. Reddy and E. Meyhofer, Nat. Nanotechnol. **10**, 253 (2015).

[14] J. Shi, B. Liu, P. Li, L.Y. Ng and S. Shen, Nano Lett. **15**, 1217 (2015).

[15] V. Chiloyan, J. Garg, K. Esfarjani and G. Chen, Nat. Commun. **6**, 6755 (2015).

[16] B. Guha, C. Otey, C.B. Poitras, S. Fan and M. Lipson, Nano Lett. **12**, 4546 (2012).

[17] C. Feng, Z. Tang, J. Yu and C. Sun, Sensors **13**, 1998 (2013).

[18] R. St-Gelais, B. Guha, L. Zhu, S. Fan and M. Lipson, Nano Lett. **14**, 6971 (2014).

[19] R. St-Gelais, L. Zhu, S. Fan and M. Lipson, Nat. Nanotechnol. **11** (2016).

[20] B. Song, D. Thompson, A. Fiorino, Y. Ganjeh, P. Reddy and E. Meyhofer, Nat. Nanotechnol. **11** (2016).

[21] G.A. Domoto, R.F. Boehm and C.L. Tien, J. Heat Transfer **92**, 412 (1970).

[22] T. Kralik, P. Hanzelka, M. Zobac, V. Musilova, T. Fort and M. Horak, Phys. Rev. Lett. **109**, 224302 (2012).

[23] C.M. Hargreaves, Phys. Lett. **30A**, 491 (1969).

[24] L. Hu, A. Narayanaswamy, X.Y. Chen and G. Chen, Appl. Phys. Lett. **92**, 133106 (2008).

[25] R.S. Ottens, V. Quetschke, S. Wise, A.A. Alemi, R. Lundock, G. Mueller, D.H. Reitze, D.B. Tanner and B.F. Whiting, Phys. Rev. Lett. **107**, 014301 (2011).

[26] T. Ijiro and N. Yamada, Appl. Phys. Lett. **106**, 023103 (2015).

[27] K. Ito, A. Miura, I. Hideo and H. Toshiyoshi, Appl. Phys. Lett. **106**, 083504 (2015).

[28] M. Lim, S.S. Lee and B.J. Lee, Phys. Rev. B **91**, 195136 (2015).

[29] M.P. Bernardi, O. Dupré, E. Blandre, P.-O. Chapuis, R. Vaillon and M. Francoeur, Sci. Rep. **5**, 11626 (2015).

[30] E.D. Palik, *Handbook of Optical Constants of Solids* (Academic Press, San Diego, 1998).

[31] M. Asheghi, M.N. Touzelbaev, K.E. Goodson, Y.K. Leung and S.S. Wong, J. Heat Transfer **120**, 30 (1998).

[32] S.G. Serra, A. Schneider, K. Malecki, S.E. Huq and W. Brenner, presented in the 3rd Int. Conf. on Multi-Material Micro Manufacture, Bulgaria, 2007.

[33] N.P. Bansal and R.H. Doremus, *Handbook of Glass Properties* (Academic Press, Orlando, 1986).

[34] T.-R. Hsu, *MEMS and Microsystems: Design, Manufacture and Nanoscale Engineering* (Wiley, Hoboken, 2008).

CHAPTER 6

CONCLUSION

Near-field thermal radiation applied to nanoscale-gap thermophotovoltaic (nano-TPV) power generation has been discussed and analyzed throughout this dissertation via a numerical and experimental approach. A numerical model of a nano-TPV power generator was developed and an experimental device was designed and fabricated for the purpose of measuring near-field radiative heat transfer across gap sizes ranging from 3500 nm to as small as 150 nm between 5×5 mm^2 planar intrinsic silicon (Si) surfaces. A summary of the main results and recommendations for future research is presented hereafter.

6.1 Numerical Modeling of a Nano-TPV Power Generator

6.1.1 Summary

A numerical model coupling near-field thermal radiation, charge and heat transport was applied to a nano-TPV power generator consisting of a gallium antimonide (GaSb) cell illuminated by broadband tungsten and quasi-monochromatic Drude emitters at 2000 K. Nano-TPV performance was analyzed relative to radiative, electrical and thermal losses as well as the type of emitter used. In particular, the effect each mode of radiative heat transfer (propagating, frustrated and surface) has on each loss mechanism was analyzed.

Results showed that all three loss mechanisms must be considered in order to accurately model a nano-TPV power generator. Failure to do so causes device performance to be greatly overestimated. Considering only radiative and electrical losses with a GaSb cell illuminated by a broadband tungsten radiator separated by a vacuum gap of 10 nm, the power density and conversion efficiency were 9.77×10^5 Wm^{-2} and 34.3%, respectively. When all three loss mechanisms were taken into account, power density and conversion efficiency dropped to 6.82×10^5 Wm^{-2} and 21.2%, respectively.

This work also quantified the effect of broadband near-field radiation comprised of frustrated modes and quasi-monochromatic radiation comprised of surface modes on each loss mechanism. In order to minimize radiation absorbed below the cell bandgap and thermalization of EHPs generated above the cell bandgap, many numerical works have focused on using quasi-monochromatic emitters that support surface modes [1-7]. A GaSb-based nano-TPV power generator illuminated by a fictitious quasi-monochromatic emitter approximated by a Drude model was analyzed. Results showed that the nano-TPV device with a broadband tungsten emitter outperformed the device with a Drude emitter for all cases except at the smallest gap sizes and when electrical and thermal losses were neglected. At a vacuum gap of 10 nm and considering all loss mechanisms, the nano-TPV device with a tungsten emitter reached a temperature of 448 K and had a power density and conversion efficiency of 6.82×10^5 Wm^{-2} and 21.2%, respectively. Under these conditions, the temperature of the cell with the Drude emitter rose above its melting point of 985 K causing the device to fail. Only when ignoring electrical and thermal losses did the device with a Drude emitter outperform the device with a tungsten emitter. The Drude-based device had a power density and conversion efficiency of

1.71×10^6 Wm^{-2} and 59.5%, respectively, while the device with a tungsten emitter achieved a power density and conversion efficiency of 1.36×10^6 Wm^{-2} and 47.9%, respectively. These results also showed that frustrated modes are more beneficial to nano-TPV power generation than surface modes.

It was shown that a nano-TPV power generator with a broadband emitter outperforms a device with a quasi-monochromatic emitter for most cases. It was also shown that performance can be further improved by tuning the emission spectrum of the emitter. By limiting radiation below the cell bandgap and determining an upper cutoff energy where the benefits of EHP generation are outweighed by the effects of thermalization, device performance was shown to improve. When eliminating radiation below 0.66 eV and above 1.45 eV, power output and conversion efficiency increased by 6.5% and 21.3%, respectively. Furthermore, cell temperature remained 30 K cooler when using the filtered spectrum. It may be possible to control the emission spectrum of the radiator using photonic crystals or meta-materials. A rigorous analysis of the optimal emission spectrum for far-field TPV power generators has recently been conducted using a genetic algorithm [8] and is currently underway for nano-TPV devices.

6.1.2 Recommendations

As stated above, the optimal emission spectrum for a far-field TPV power generator has recently been studied. This model is also currently being used to determine the optimal spectrum to use with a nano-TPV device.

The coupled radiative, heat and charge transport model is capable of simulating nano-TPV power generators with cells comprised of the ternary alloys of indium gallium arsenide (InGaSb). A database with various other TPV materials such as indium arsenide

(InAs) and germanium (Ge) should be created. This will allow for the study of how the three loss mechanisms affect a wider variety of TPV cells. Also, varying cell architectures such as cell thickness, n-on-p or p-on-n configuration and doping levels should be studied. However, the required temperature-dependent material properties are currently not widely available and may require significant research effort to determine.

The numerical model currently incorporates tungsten, Drude and blackbody radiators. Additional emitters such as silicon carbide (SiC), cubic boron nitride (cBN), rare-earth oxides and photonic crystals could be added to the model. A larger database of emitters would allow for a potentially large number of emitter-cell combinations. Along with the determination of an optimal emission spectrum, these would aide in the research and optimization of nano-TPV power generators and expedite the development of real engineering devices.

The design of a TPV cell should be further explored with respect to near-field radiative heat transfer. In typical solar applications, only propagating modes are incident on the cell. However, in nano-TPV applications, radiative heat transfer will be dominated by frustrated or surface modes. Absorption characteristics of a cell are dependent on the type of radiative mode present. A numerical model such as the one described in Chapter 3 may be beneficial to the design of cells used in nano-TPV power generators.

6.2 Experimental Measurements of Near-Field Radiative Heat Transfer

6.2.1 Summary

Only two groups [9-14] have conducted experiments on nano-TPV devices. The results showed mostly qualitative performance improvements at microscale gaps. A major bottleneck in nano-TPV experimental research is the difficulty in maintaining a

nanoscale gap between macroscale planar surfaces. Furthermore, radiative heat transfer exceeding the blackbody limit at nanoscale gaps between macroscale planar surfaces has never been shown experimentally. This bottleneck must be overcome prior to any meaningful research on nano-TPV devices can be conducted.

Thus far in the literature, most near-field radiative heat transfer experiments have been limited to a tip-surface [15-17], sphere-surface [18-26] or microstructure geometry [27-30] due to the difficulty associated with maintaining a nanoscale gap between macroscale surfaces. In Chapter 5, measurements were presented between macroscale planar surfaces at gap sizes smaller than anything previously published.

A MEMS-based device capable of measuring radiative heat transfer between 5 × 5 mm^2 intrinsic Si surfaces across a variable gap has been designed. Radiation across gap sizes ranging from 3500 nm, where thermal radiation is dominated by propagating modes, down to 150 nm, where thermal radiation is dominated by evanescent modes, is measured. The emitter and receiver are separated by a set of 3500-nm-tall SU-8 photoresist posts. The emitter is suspended by a 20-μm-thick compliant Si membrane such that the emitter can move relative to the receiver. Calibrated masses were used to apply a mechanical load to the emitter causing the Si membrane to flex and decrease the gap size. A set of 150-nm-tall SiO_2 stoppers prevent the emitter from making direct contact with the receiver.

The heat rate through the device was modulated using a thermoelectric heat pump mounted to the emitter while a thermoelectric cooler was mounted to the receiver in order to maintain a constant temperature of 300 K. Temperatures on either side of the device were measured using thermistors embedded in copper heat spreaders. Experimental

results were compared to a comprehensive model coupling COMSOL Multiphysics and fluctuational electrodynamics. This method of measurement was verified for a simple case of conduction through a 1.1-mm-thick piece of borosilicate glass and for near-field radiation at gap sizes of 200 and 500 nm. The gap sizes were maintained using polystyrene spheres as spacers.

Unprocessed experimental results matched numerical predictions extremely well at gap sizes of 3500 and 150 nm. The heat flux was found to exceed blackbody predictions by a factor of 8.4 for a temperature difference of 115.59 K and a gap size of 150 nm. This is the largest heat flux enhancement over blackbody between two macroscale planar surfaces near room temperature ever recorded in the literature. Although evanescent modes contribute to heat flux at a gap size of 3500 nm, they are not sufficient to exceed the blackbody limit. Intermediate gap sizes were determined by fitting the numerical model with the experimental results. Although it was not possible to determine precise gap sizes using this method, the device behaved as expected with the measured heat rate increasing as the applied load was increased. The increasing heat rate indicated an increasing contribution of evanescent modes. Therefore, it can be concluded that the gap size was decreasing.

6.2.2 Recommendations

Since radiative heat transfer between macroscale planar surfaces was measured at gap sizes smaller than anything previously reported in the literature, one of the next steps is to generate power with a nano-TPV device. By using the current design and replacing the receiver with a TPV cell, it would be possible to measure power generation at multiple gap sizes. This would allow for the quantitative determination of performance

enhancement at a variety of gap sizes. In addition to TPV experiments, this setup is also suitable for measuring near-field thermal rectification [31].

The current device as designed is extremely delicate due the weak bond between the SU-8 posts and Si. The compliant membrane is also prone to breakage. Further development and design modifications will be required in order to improve the sturdiness of the device. Also, the fabrication processes used for Si may not be compatible with a TPV cell materials. A custom fabricated cell would also be necessary since electrical contacts or antireflective coatings on the top surface of the cell may limit the minimum possible gap size.

A simpler method to conduct these experiments would be to use polystyrene spheres as spacers between an emitter and receiver as discussed in Section 5.3.2.2. Since minimal fabrication time is required, measurements could be made much quicker than with the near-field radiative heat transfer device. However, this method does not allow for multiple gap sizes with a single device and the emitter temperature would be limited as polystyrene has a melting temperature of 513 K. Alignment of the emitter and receiver is currently accomplished manually and is extremely difficult. A micropositioner could be utilized in order to simplify this task.

As stated at the beginning of Chapter 5, gap control and measurement was originally intended to be accomplished using electrostatic forces and capacitance. Due to limitations with the equipment and the experimental setup, this method did not work as expected. However, this may still be a valid method for gap control and warrants further development. Additionally, an algorithm could be developed to allow for a closed-loop feedback system where the gap self-adjusts in order to optimize power output or

conversion efficiency of the nano-TPV system. A resistance temperature detector patterned on the interior surfaces of the device from a thin metallic layer could be used to continuously monitor device and emitter temperatures. This data could be used in the feedback loop to automatically adjust the device to an optimal gap. There is currently a pending patent on this mechanism [32]. Preliminary data on this work is presented in Appendix A.

There is also much research that needs be accomplished with the TPV cell itself. Research on low-bandgap TPV cells is still a relatively new field and there are currently no commercially available cells. At the relatively low emitter temperatures (up to 420 K) studied in this dissertation, cells with bandgaps as low as 0.17 eV may be required. Additionally, there is a great deal of research to be done regarding the emitter. At such low temperatures, it is paramount to optimize the emission spectrum in order to produce as much power or operate at the highest conversion efficiency possible. It is important to note that based on the results from Chapter 3, radiative heat transfer based on frustrated modes as opposed to surface modes may be better suited to nano-TPV power generation. This is where the coupled near-field thermal radiation, charge and heat transport model presented in Chapter 3 and the recommendations discussed in section 6.1.2 become extremely useful.

6.3 References Cited

[1] A. Narayanaswamy and G. Chen, Appl. Phys. Lett. **82**, 3544 (2003).

[2] M. Laroche, R. Carminati and J.-J. Greffet, J. Appl. Phys. **100**, 063704 (2006).

[3] R. Messina and P. Ben-Abdallah, Sci. Rep. **3**, 1383 (2013).

[4] V.B. Svetovoy and G. Palasantzas, Phys. Rev. Appl. **2**, 034006 (2014).

[5] O. Ilic, M. Jablan, J.D. Joannopoulos, I. Celanovic and M. Soljačić, Opt. Express **20**, A366 (2012).

[6] C. Simovski, M. Stanislav, I. Nefedov and S. Tretyakov, Opt. Express **21**, 14988 (2013).

[7] Y. Guo, S. Molesky, H. Hu, C.L. Cortes and Z. Jacob, Appl. Phys. Lett. **105**, 073903 (2014).

[8] J. DeSutter, M.P. Bernardi and M. Francoeur, Ener. Convers. Manage. **108**, 429 (2016).

[9] R.S. DiMatteo, P. Greiff, S.L. Finberg, K.A. Young-Waithe, H.K.H. Choy, M.M. Masaki and C.G. Fonstad, Appl. Phys. Lett. **79**, 1894 (2001).

[10] R.S. DiMatteo, P. Greiff, S.L. Finberg, K.A. Young-Waithe, H.K.H. Choy, M.M. Masaki and C.G. Fonstad, presented at the 5th Conference on Thermophotovoltaic Generation of Electricity, 2003.

[11] .S. DiMatteo, P. Greiff, D. Seltzer, D. Meulenberg, E. Brown., E. Carlen, K. Kaiser, S. Finberg, H. Nguyen, J. Azarkevich, P. Baldasaro, J. Beausang, L. Danielson, M. Dashiell, D. DePoy, H. Ehsani, W. Topper and K. Rahner, presented at the 6th Conference on Thermophotovoltaic Generation of Electricity, 2004.

[12] K. Hanamura and K. Mori, presented at the 7th Conference on Thermophotovoltaic Generation of Electricity, 2007.

[13] K. Hanamura, H. Fukai, E. Srinivasan, M. Asano and T. Masuhara, Photovoltaic generation of electricity using near-field radiation, presented at the ASME/JSME 2011 8th Thermal Engineering Joint Conference, 2011.

[14] J. Yoshida, Y. Ashida and K. Hanamura, Thermophotovoltaic generation of electricity by GaSb schottky cell using evanescent effect, presented at the International Workshop on Nano-Micro Thermal Radiation, 2012.

[15] A. Kittel, W. Müller-Hirsch, J. Parisi, S.-A. Biehs, D. Reddig and M. Holthaus, Phys. Rev. Lett. **95**, 224301 (2005).

[16] A. Kittel, U.F. Wischnath, J. Welker, O. Huth, F. Rüting and S.-A. Biehs, Appl. Phys. Lett. **93**, 193109 (2008).

[17] K. Kim, B. Song, V. Fernández-Hurtado, W. Lee, W. Jeong, L. Cui, D. Thomson, J. Feist, M.T.H. Reid, F.J. García-Vidal, J.C. Cuevas, E. Meyhofer and P. Reddy, Nature **528**, 387 (2015).

[18] A. Narayanaswamy, S. Shen and G. Chen, Phys. Rev. B **78**, 115303 (2008).

[19] A. Narayanaswamy, S. Chen, L. Hu, X.Y. Chen and G. Chen, Appl. Phys. A **96**, 357 (2009).

[20] S. Shen, A. Narayanaswamy and G. Chen, Nano Lett. **9**, 2909 (2009).

[21] E. Rousseau, A. Siria, G. Jourdan, S. Volz, F. Comin, J. Chevrier and J.-J. Greffet, Nature Photon. **3**, 514 (2009).

[22] P.J. van Zwol, L. Ranno and J. Chevrier, Phys. Rev. Lett. **108**, 234301 (2012).

[23] P.J. van Zwol, S. Thiele, C. Berger, W.A. de Heer and J. Chevrier, Phys. Rev. Lett. **109**, 264301 (2012).

[24] N. Gu, K. Sasihithlu and A. Narayanaswamy, Near field radiative heat transfer measurement, presented in *Optical Nanostructures and Advanced Materials for Photovoltaics*, Austin, TX, 2011.

[25] S. Shen, A. Mavrokefalos, P. Sambegoro and G. Chen, Appl. Phys. Lett. **100**, 233114 (2012).

[26] B. Song, Y. Ganjeh, S. Sadat, D. Thomson, A. Fiorino, V. Fernández-Hurtado, J. Feist, F.J. García-Vidal, J.C. Cuevas, P. Reddy and E. Meyhofer, Nat. Nanotechnol. **10**, 253 (2015).

[27] C. Feng, Z. Tang, J. Yu and C. Sun, Sensors **13**, 1998 (2013).

[28] R. St-Gelais, B. Guha, L. Zhu, S. Fan and M. Lipson, Nano Lett. **14**, 6971 (2014).

[29] R. St-Gelais, L. Zhu, S. Fan and M. Lipson, Nat. Nanotechnol. **11** (2016).

[30] B. Song, D. Thompson, A. Fiorino, Y. Ganjeh, P. Reddy and E. Meyhofer, Nat. Nanotechnol. **11** (2016).

[31] C.R. Otey, W.T. Lau and S. Fan, Phys. Rev. Lett. **104**, 154301 (2010).

[32] M.P. Bernardi and M. Francoeur, U.S. Application No. 14/941,257 (13 November 2015.

APPENDIX A

USING ELECTROSTATIC FORCES AND CAPACITANCE FOR CONTROLLING AND MEASURING THE GAP SIZE BETWEEN MACROSCALE PLANAR SURFACES SEPARATED BY A NANOSCALE GAP

As discussed in Chapter 5, the original design of the near-field radiative heat transfer device incorporated electrostatic forces and capacitance for adjusting and measuring the gap size. This method ultimately was not used due to difficulties with the equipment and experimental setup. In this appendix, the research conducted and preliminary measurements related to the electrostatically modulated gap control mechanism are presented.

A.1 Gap Size Modulation via Electrostatic Forces

A net force arises when differing charges are applied to two opposing surfaces. This force can be used to actuate MEMS-based devices [1]. In the near-field radiative heat transfer device discussed in Chapter 5, four gold 500 × 500 μm^2, 20-nm-thick electrodes were deposited on the emitter and receiver surfaces using electron-beam evaporation with a Denton SJ20C. The electrostatic forces were to be balanced by the restoring spring force of the compliant membrane. The electrostatic force, F_{ES}, and the restoring spring force, F_{Sp}, are defined as follows:

$$F_{ES} = \frac{1}{2}\frac{\varepsilon_0 \varepsilon A}{d^2}V^2 \tag{A.1}$$

$$F_{Sp} = kd \tag{A.2}$$

where ε_0 and ε are the vacuum permittivity of 8.854×10^{-12} Fm^{-1} and relative permittivity of the medium between the electrodes, respectively. Since the gap between the electrodes was vacuum, the relative permittivity takes a value of unity. A denotes the electrode area, d is the separation gap thickness and V is the voltage difference between opposing surfaces. The spring coefficient of the membrane and the displacement of the emitter are denoted by k and d, respectively.

Figure A.1 shows the electrostatic and spring forces as a function of gap size with respect to the voltage applied to the electrodes. As can be seen in the figure and inferred from Equations (A.1) and (A.2), the spring force increases linearly as gap size d decreases while the electrostatic force scales with d^{-2}. Due to the difference in scaling, a minimum stable gap size arises below which the electrostatic force is always larger than the restoring spring force causing the device to snap in to the closed position. For the fabricated near-field radiative heat transfer device with an open position gap size of 3500 nm, the minimum stable gap size d_{min} = 2333 nm and applied voltage V = 42.9 V.

Figure A.2 shows force as a function of gap size for various applied voltages. All gaps smaller than 2333 nm were unstable and resulted in the device snapping in to its closed position. In fact, this phenomenon was not specific to this application. Any actuation system relying on electrostatic attractive forces balanced by restoring spring forces exhibits a snap-in condition at ⅔ of the initial gap size [2].

The following derivation shows that the snap-in point is not dependent on initial

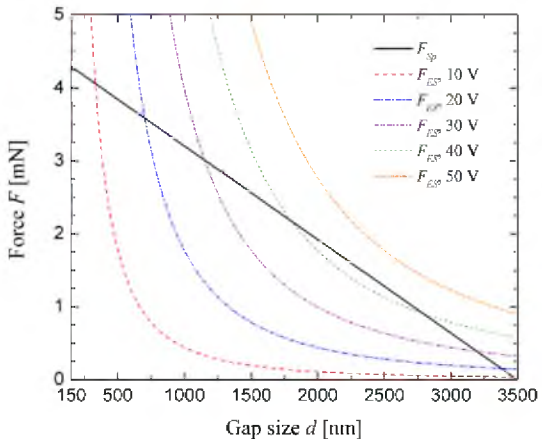

Figure A.1 Electrostatic force, F_{ES}, and spring force, F_{Sp}, as a function of gap size with respect to applied voltage. At gap sizes smaller than 2333 nm or voltages larger than 42.9 V the device under study exhibits an instability and snaps in to its minimum gap size.

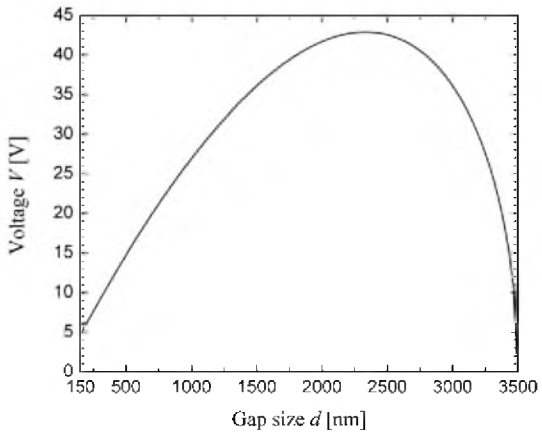

Figure A.2 Gap size as a function of voltage for the device under study. The actuation mechanism is unstable at gap sizes less than 2333 nm.

gap size, electrode area, spring coefficient or applied voltage. In order for a gap position to be stable, the restoring spring force, F_{Sp}, must be equal to the electrostatic force, F_{ES}. By setting Equations (A.1) and (A.2) equal to each other and knowing that the displacement of the emitter $d' = d_0 - d$ where d_0 is the initial gap size and d is the actual gap size yields:

$$\frac{1}{2}\frac{\varepsilon_0 \varepsilon A}{d^2}V^2 = (d_0 - d)k \qquad \text{(A.3)}$$

The maximum voltage needed to bring such a device to its minimum stable gap, d_{min}, occurs at:

$$\frac{\partial V}{\partial d} = 0 \tag{A.4}$$

Solving Equations (A.3) and (A.4) and simplifying yields:

$$d_{min} = \frac{2}{3} d_0 \tag{A.5}$$

As can be seen in Equation (A.5), snap-in always occurs at ⅔ the initial gap size, d_0, and is independent of any other variables. However, it is important to note that Equation (A.5) is only valid when the spring coefficient is a constant value. By utilizing a spring coefficient that is a function of gap size, the point at which snap-in occurs can be modified. A gap-dependent spring coefficient can be determined by solving Equations (A.3) and (A.4) with the assumption that the spring coefficient k is a function of gap size d. This yields Equations (A.6) and (A.7).

$$k(d) = k_0 \exp\left(-b\frac{d}{d_0}\right) \tag{A.6}$$

$$b = \frac{2a^{-1} - 3}{1 - a} \tag{A.7}$$

where k_0 is a nominal spring coefficient at the initial gap size and a is the ratio of the minimum stable gap size d_{min} to the initial gap size d_0 and takes values $0 < a < 1$.

Although gap size actuation is typically limited to ⅔ of the initial gap size, this obstacle can potentially be overcome by the use of a membrane with a non-linear spring coefficient as described by Equations (A.6) and (A.7). Alternatively, electrostatic repulsion can be used to modulate the gap without any points of instability. By designing the device so that the initial gap size is equivalent to its minimum gap size, only positive

(or negative) charges can be applied to the electrodes to repel the surfaces from each other.

A.2 Gap Size Measurement using Capacitance

Capacitance can be used to measure the distance between the emitter and receiver. A set of three gold 500 × 500 μm^2, 20-nm-thick pads were deposited on the emitting and receiving surfaces using the Denton SJ20C electron-beam evaporator. Capacitance, C, as a function of gap size and area is shown in Equation (A.8).

$$C = \frac{\varepsilon_0 \varepsilon A}{d} \tag{A.8}$$

Figure A.3 depicts capacitance as a function of gap size. When the device was in the open position at 3500 nm, the capacitance was expected to be 1.90 pF while capacitance of 44.25 pF was expected at the closed position gap size of 150 nm.

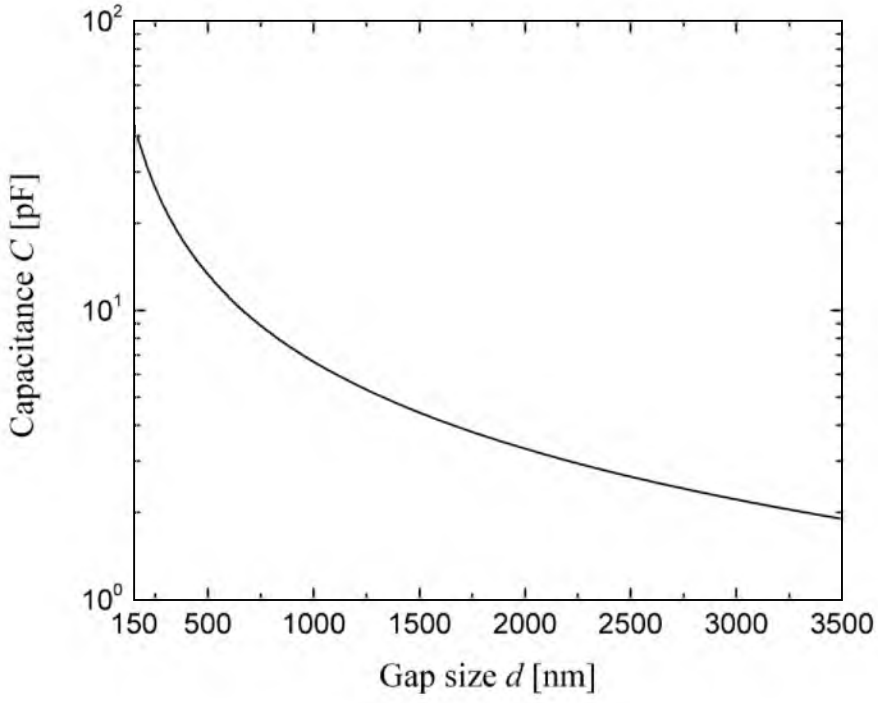

Figure A.3 Capacitance as a function of gap size.

A.3 Experimental Measurements using Electrostatic Actuation and Capacitive Measurements

Figure A.4 shows experimental measurements of the gap control mechanism. Measured capacitance and estimated gap size are shown as a function of applied voltage. The error bars shown are based on the measurement uncertainty of the equipment where the error in the voltage is ± (0.5% + 0.2 V) and the error in the capacitance is ± (1.0% + 0.01 pF). The reported capacitance is the sum of all three capacitive sensors. When there was 1 V applied to the electrostatic pads, the measured capacitance was 203.6 pF. According to Eq. (A.8), this corresponded to a gap size of 32.6 nm. At an applied voltage of 30 V, the measured capacitance was 101.6 pF which corresponded to a 65.3-nm-thick gap. However, the minimum possible gap size in the device was 150 nm due to the height of the silicon dioxide stoppers. Not only did these values not agree with the data in Figures A.2 and A.3, the trend was also inverted. Instead of capacitance increasing as voltage to the electrostatic pads was increased (which should correspond to a decreasing gap size), the measured capacitance tended to decrease which indicated an increasing gap size.

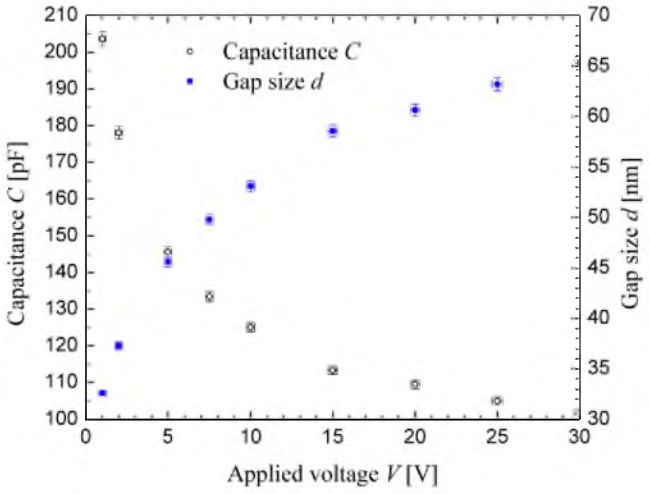

Figure A.4 Capacitance, C, and gap size, d, as a function of applied voltage.

The capacitance meter (BK Precision, 889B) was capable of measuring values as low as 79 fF; therefore, its capabilities were not a concern. However, it was found that the parasitic capacitance introduced by the wiring of the experimental setup and the vacuum chamber feedthroughs was much larger than the capacitance of the device gap sensor. This parasitic capacitance was measured to be on the order of 100 pF while the expected value for the device gap sensors was 44.3 pF at a gap size of 150 nm. Additionally, since only one capacitance meter was available, all three capacitance sensors had to be connected in parallel and measured simultaneously. The act of disconnecting and reconnecting the capacitance meter to make individual measurements can introduce error since the connection itself is slightly different each time. Also, the voltage source used did not perform with the advertised accuracy or precision.

For future research, a dedicated data acquisition system with a higher quality voltage source should be used. In this way, each capacitor can be measured independently while compensating for any parasitic capacitance. Independently measuring each capacitive gap sensor would also have the benefit of allowing for the determination of parallelism between the emitter and receiver. Shorter lengths of wire, higher quality connectors and 4-wire sensing could be used to reduce and account for parasitic capacitance. Also, larger capacitor plates could be used. This could make the desired capacitance larger relative to any parasitic effects.

A.4 References Cited

[1] D.J. Bell, T.J. Lu, N.A. Fleck and S.M. Spearing, J. Micromech. Microeng. **15**, S153 (2005).

[2] W.-M. Zhang, G. Meng and D. Chen, Sensors **7**, 760 (2007).

APPENDIX B

EXPERIMENTAL APPARATUS FOR PERFORMING NEAR-FIELD RADIATIVE HEAT TRANSFER MEASUREMENTS

As discussed in Chapter 5, fabrication for the near-field radiative heat transfer device was conducted at the University of Utah Nanofab. In order to minimize the possibility of contaminating the device with particles that could lead to unwanted heat transfer by conduction, it was important that any experimental testing also be conducted in a clean environment. The University of Utah Nanofab generously donated an 8×6 ft^2 cleanroom tent to the Radiative Energy Transfer Lab. Although the original purpose of the tent was to allow for the experimental testing presented in this dissertation, it has also been used for other experiments greatly expanding the capabilities of the Radiative Energy Transfer lab.

Figure B.1 depicts the assembled tent including all the experimental equipment. All sample preparation and testing were conducted within this cleanroom environment. Using a portable particle counter, it was determined that the tent operates at a class 1000 level. Fans draw in air from above the tent, filter it through four 4×2 ft^2 HEPA filters and force it downward and out from under the curtains. The resulting laminar flow immediately removes any particles from within the tent.

The tent currently houses a $12 \times 12 \times 12$ in^3 box-style vacuum chamber capable of achieving vacuum levels of 10^{-4} Pa. Two 19-pin feedthroughs were used to deliver power

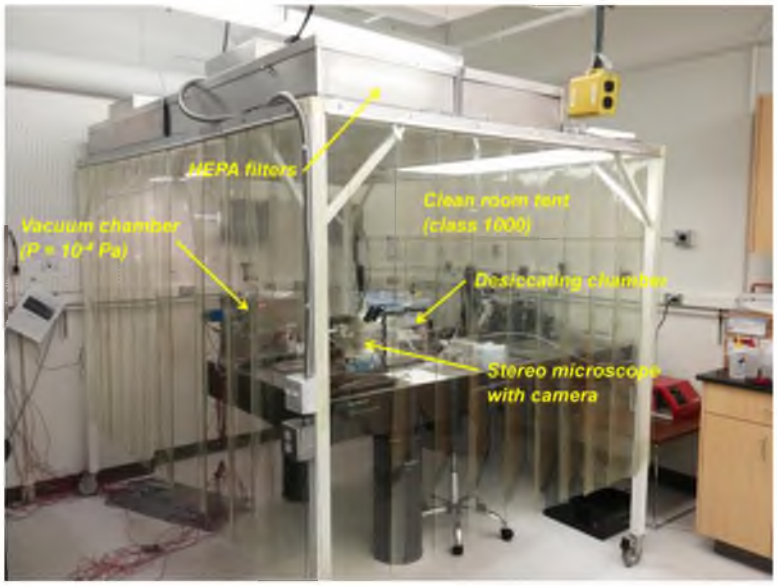

Figure B.1 Class 1000 clean room tent located in the Radiative Energy Transfer Lab.

to the thermoelectric heater and cooler as well as the wiring for the thermistors. There is also a UV/ozone cleaner used for sample cleaning and preparation and a stereo microscope utilized for sample inspection. An oven was employed for baking or drying samples when necessary and a desiccating chamber was used for sample storage.

Figure B.2 shows the instrumentation and power supplies employed in the experimental setup. As stated in Chapter 5, a BK Precision 889B LCR meter was used to measure the resistance of the thermistors and the capacitance of the gap sensors. A BK Precision 9121A power supply was utilized to power the thermoelectric heat pump while a BK Precision 1667 power supply was used for the thermoelectric cooler. The 1667 was not nearly as precise or accurate as the 9121A; however, since the cooler was only meant to maintain a constant temperature of 300 K, precisely measuring the power delivered to it was not critical. A laptop was employed for data recording and processing.

There is still room for improvement in this experimental setup. Maintaining a 300 K receiver temperature required constant manual adjustment of the thermoelectric cooler

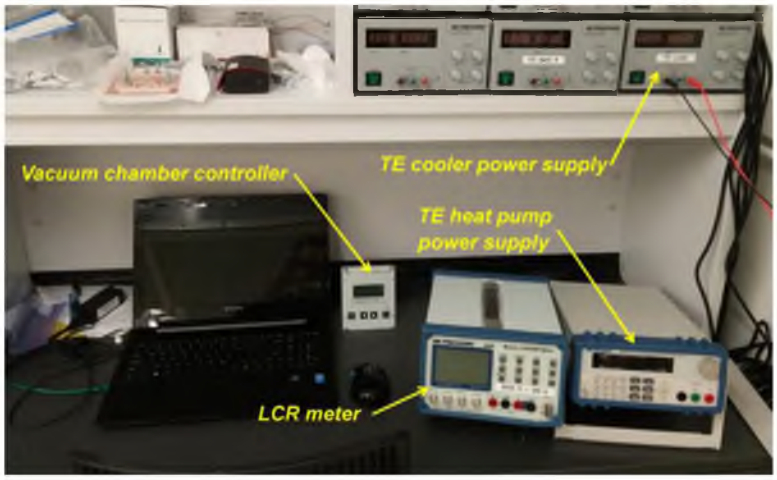

Figure B.2 Power supplies, LCR meter and vacuum chamber controller required for experimental measurements.

and heat pump power supplies. With each adjustment, approximately 5 to 10 min was required for the system to reach steady-state. This resulted in a time-consuming data collection process. Furthermore, any postprocessing of the data was completed manually. Integrating the power supplies and LCR meter with a data acquisition system such as LabVIEW could greatly streamline the data collection process and even automatically complete some of the data processing tasks. This would allow for real-time comparison of experimental data with theoretical predictions.